Ice Age changes: Antarctic sea ice and sea-surface temperature in the Southwest Pacific Ocean and their relationship to ocean circulation, marine productivity, and atmospheric carbon dioxide concentrations

by

Jacob Jones

Bachelor of Arts, University of British Columbia, 2016

Thesis Submitted in Partial Fulfillment of the
Requirements for the Degree of
Master of Resource Management

in the
School of Resource and Environmental Management
Faculty of Environment

SIMON FRASER UNIVERSITY
Summer 2022

Declaration of Committee

Name:	**Jacob Jones**
Degree:	**Master of Resource Management**
Title:	**Ice Age changes: Antarctic sea ice and sea-surface temperature in the Southwest Pacific Ocean and their relationship to ocean circulation, marine productivity, and atmospheric carbon dioxide concentrations**
Committee:	**Chair:** **Tammara Soma** Assistant Professor, Resource and Environmental Management
	Karen Kohfeld Supervisor Professor, Resource and Environmental Management
	Kirsten Zickfeld Committee Member Professor, Geography
	Brent Ward Examiner Professor, Earth Sciences

Abstract

Antarctic sea ice is hypothesized to have played an important role in modulating ocean circulation, marine productivity, and atmospheric carbon dioxide (CO_2) concentrations on glacial-interglacial timescales; however, few reconstructions exist to directly link them. Here I reconstruct past winter sea ice concentration, sea surface temperature, and biogenic opal burial in a marine sediment core from the Southern Ocean over the last 140,000 years. The results suggest that Antarctic sea ice expansion was not a major contributor to CO_2 drawdown early in the glacial cycle, but a weakening of meridional temperature gradients could have contributed to early atmospheric CO_2 drawdown via their impact on air-sea gas exchange. Furthermore, sea-ice expansion appears linked to reductions in intermediate water mass production. Opal burial was high during the Holocene period and reduced during times of sea-ice expansion. Opal reductions may also be associated with southward migrations in the Antarctic Polar Front during warming periods.

Keywords: Sea ice; Antarctica; glacial-interglacial cycle; carbon dioxide

Acknowledgements

This research was not possible without the close supervision of Dr. Karen Kohfeld. You've been an excellent mentor throughout this learning process, and I deeply appreciate the patience and support you've provided me. A special thanks to Helen Bostock, Xavier Crosta, Melanie Liston, Gavin Dunbar, Zanna Chase, Amy Leventer, Harris Anderson, and Geraldine Jacobsen, for all your hard work and support on this project. I would also like to thank Kirsten Zickfeld and the members of the COPE lab for their guidance and support along the way. Finally, I'd like to give special thanks to my partner – Thea Buitendyk – who has provided unending and unconditional support over the last 3 years. This would not have been possible without you.

This work was supported by a Canadian Natural Sciences and Engineering Research Council grant (Discovery Grant RGPIN342251) provided to Karen Kohfeld. Travel funding for workshop collaboration was provided by a Past Global Changes (PAGES) grant to the Cycles of Sea Ice Dynamics in the Earth System (C-SIDE) Working Group. A special thanks to Rachel Meyne (Colgate University), who assisted with diatom slide preparation, and Dr. Maureen Soon (University of British Columbia), who assisted with opal concentration measurements. The TAN1302-96 core was collected during the TAN1302 RV Tangaroa voyage to the Mertz Polynya. We would like to thank the Voyage leader Dr. Mike Williams and Captain Evan Solly and the crew, technicians, and scientists involved in the TAN1302 voyage. The voyage was co-funded by NIWA, Australian, and French research funding. We acknowledge Dr. Andrew Kingston for running the stable isotopes at NIWA. We acknowledge ANSTO grant AP11676 for funding the additional radiocarbon dates. This research was partially supported by the Australian Government through the Australian Research Council's Discovery Projects funding scheme (project DP180102357) awarded to Zanna Chase and Helen Bostock.

Table of Contents

List of Tables

List of Figures

List of Acronyms

AABW	Antarctic Bottom Water
AAIW	Antarctic Intermediate Water
APF	Antarctic Polar Front
AZ	Antarctic Zone
DBD	Dry bulk density
DIC	Dissolved inorganic carbon
DSW	Dense Shelf Water
LCDW	Lower Circumpolar Deep Water
LGM	Last Glacial Maximum
MAR	Mass accumulation rate
MAT	Modern analog technique
MIS	Marine isotope stage
POOZ	Permanent Open Ocean Zone
ppm	Parts per million (per mil)
SALH	Silicic Acid Leakage Hypothesis
SAZ	Sub-Antarctic Zone
SIC	Sea ice concentration
SO	Southern Ocean
SSI	Summer sea ice
SSST	Summer sea surface temperature
SST	Sea surface temperature
STF	Subtropical Front
UCDW	Upper Circumpolar Deep Water
WSIC	Winter sea ice concentration
WSIP	Winter sea ice presence

Chapter 1: Climate Proxies and Their Use

1.1 Introduction

Ever since the high-resolution Vostock ice cores were retrieved from Antarctica in the 1980s (Delmas, 1980; Neftel et al., 1982), paleoclimatologists have been working to better understand the mechanisms driving the observed cyclicity in atmospheric carbon dioxide (CO_2) concentrations over the last 800 thousand years (ka). Ice core reconstructions have shown that atmospheric CO_2 has varied between ~190 parts per million (ppm) during glacial maxima and ~280 ppm during warm interglacial periods, corresponding to fluctuations in global temperature and the expansion and collapse of global ice sheets (e.g., Petit et al., 1999; Denton et al., 2010). The changes in atmospheric CO_2 concentration cannot be explained by variations in the Earth's orientation and orbit alone, suggesting that internal positive feedbacks likely play a key role in governing the timing and amplitude of these climate changes (e.g., Sigman et al. 2010; Gregoire et al., 2015). The relative size of the ocean as a carbon reservoir, which is approximately 60x larger than the atmosphere, suggests that small changes in how the marine carbon cycle operates could have large impacts on atmospheric CO_2 concentrations (e.g., Broecker and Peng, 1982; Sigman and Boyle, 2000). The Southern Ocean is a location of particular interest as it is one of the few locations where the deep ocean directly interacts with the atmosphere (e.g., Jaccard et al., 2013; Stein et al., 2020). Proposed mechanisms linking the Southern Ocean to changes in atmospheric CO_2 include physical and biological processes, including (but not limited to): increased sea ice coverage and reduced air-sea gas exchange (Stephens and Keeling, 2000), sea ice-related changes in ocean circulation and ventilation (Toggweiler, 1999; Bouttes et al., 2010; Ferrari et al., 2014); and changes in the biological pump, either through iron fertilization (e.g., Martin et al., 1990; Archer and Johnson, 2000) or through a regime shift in primary production via changes in the supply of nutrients (e.g., Brzezinski et al., 2002; Matsumoto et al., 2002). Despite coordinated global efforts to better understand the main drivers of glacial-interglacial CO_2 fluctuations, the precise mechanism(s) remain undetermined.

This thesis uses marine sediment core TAN1302-96 (59.09°S, 157.05°E, water depth 3099 m) extracted from the southwestern Pacific sector of the Southern Ocean to

produce novel paleoclimate reconstructions using proxy data to help address the following research questions:

> [1] How has sea ice changed in the southwestern Pacific sector of the Southern Ocean over the last 140 ka?
>
> [2] How do these changes relate to changes in ocean circulation, marine primary production, and changes in atmospheric CO_2?

This chapter provides background information on the climate proxies used in this thesis, introduces the Southern Ocean and the influence of sea ice on carbon cycle processes, outlines what we currently know about sea ice reconstructions, and identifies some major gaps in our knowledge. Chapter 2 provides new winter sea ice concentration (WSIC) and summer sea surface temperature (SSST) estimates over the last 140 ka; evaluates the timing of sea ice advance and its potential impact on CO_2 sequestration; and highlights a potential link between sea-ice expansion and intermediate water production and subduction. Chapter 3 compares sea ice expansion estimates from TAN1302-96 with a new analysis of biogenic opal and calcium carbonate (CaCO3) concentrations, mass accumulation rates (MARs), and iron deposition. This chapter provides an evaluation of the interplay between these factors over a full glacial-interglacial cycle, highlighting the role of sea ice, migrating ocean fronts, and other sedimentary factors in governing in opal burial. Finally, Chapter 4 provides a conclusion on the major findings outlined in this thesis.

1.2 Climate Proxies

Observations of today's climate, including current sea surface temperatures, regional precipitation, and seasonal sea-ice extent, are made using a variety of instruments that have been in use for around a century or two (depending on the instrument). These instrumental records provide precise measurements of physical phenomena, but they can only provide information since their use and records began. Sea surface temperature measurements, for example, have been collected for nearly 200 years during ship voyages by sailors and other crew (Chan, 2021). On the other hand, sea-ice extent was not well documented until 1979 when satellite imaging allowed for more precise measurements (Parkinson & Cavalieri, 2012), although whaling and ship's log

records have provided some rough estimates of sea-ice coverage before this time (Armand et al., 2017). To understand what the climate was like before these records began, climate proxies are employed to extend our baseline back into the past.

Climate proxies are a way of understanding the past climate through indirect measurements, such as through an analysis of tree pollen, diatoms, or geochemical signatures, all of which are influenced by, and therefore capture, some aspect(s) of the past environment. For example, diatoms (i.e., single cellular aquatic algae) live in the top layers of the ocean, and the relative abundances of diatom species tend to reflect local sea surface temperature because each species has relatively narrow temperature preferences (Resende et al., 2005). Diatom assemblages from the polar waters just off the coast of Antarctica are dominated by diatom species with very cold temperature preferences. Conversely, if we were to also look at the diatom assemblages from the Sea of Cortez in Mexico, we would find diatoms with warmer temperature preferences. Diatoms are particularly useful climate proxies because they have narrow ecological preferences and because their cell walls are made of silica (Si), which allow them to preserve well in marine sediments. As a result, sediment cores from the bottom of the ocean allow us to assess diatom assemblages at different depth intervals to interpret how the past environment has changed. By combining the identified diatom assemblages with a constructed age model (outlined below) and a statistical framework that relates diatom assemblages to today's environment, we are able to quantitatively reconstruct past environments, including past temperatures and sea-ice extent.

1.2.2 Diatoms

Diatoms (Figure 1) are single-celled phytoplankton that live in aquatic environments around the world (Smol & Stoermer, 2010). They provide a significant amount of the world's oxygen and constitute roughly 23% of the world's total global primary productivity and about 40% of marine primary production (Snoeijs et al., 2002; Serôdio & Lavaud, 2020). Estimates of the number of diatom species range from ~2,000 to over 200,000 (Mann & Droop, 1996), making them both ubiquitous and diverse. Diatoms have relatively narrow ecological preferences, including specific temperature, salinity, and sea-ice tolerances, which create diverse species assemblages depending on local climate parameters (Resende et al., 2005). Diatom frustules (shells) are made of silica, which allow them to preserve well in ocean sediments over millions of years (Serôdio & Lavaud,

2020; Westacott et al., 2021). Between the ubiquity, diversity, narrow ecological preferences, and good preservation, fossil diatoms are excellent proxies for paleoceanographic reconstructions.

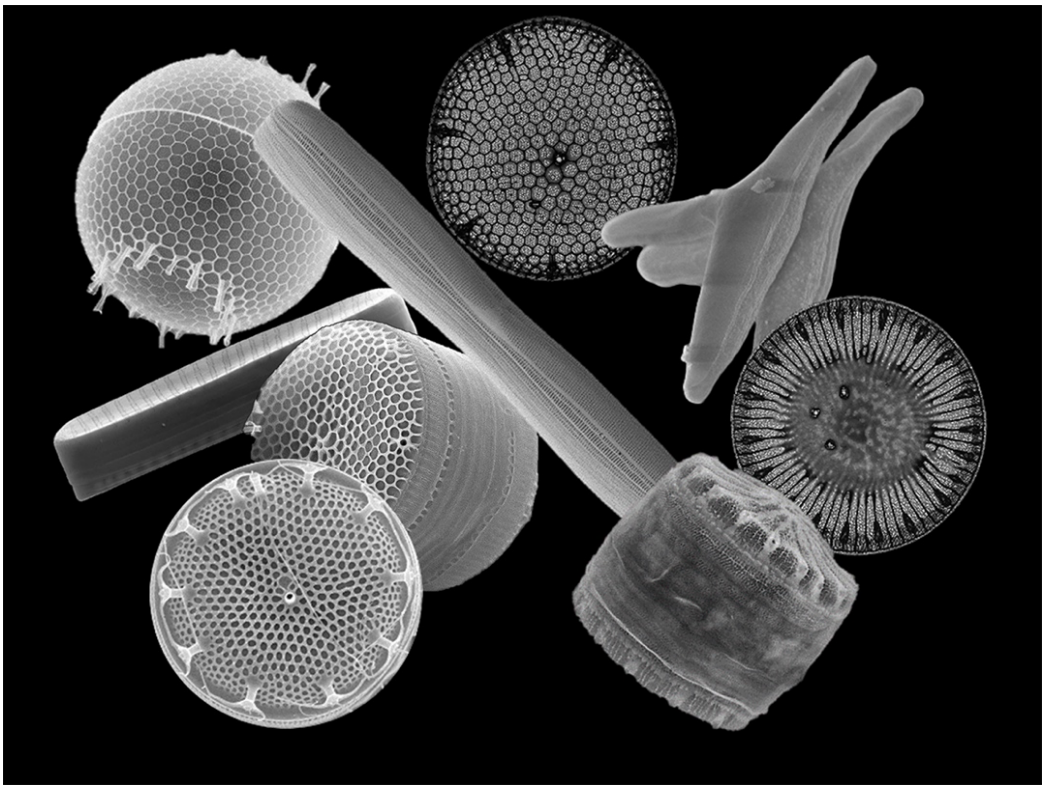

***Figure 1**: Scanning electron microscope (SEM) image of pennate and centric diatoms. Image retrieved from https://jgi.doe.gov/csp-2021-100-diatom-genomes/.*

1.2.2.1 Using Diatoms to Estimate Past Environmental Conditions

Statistical comparisons of fossil diatom assemblages with modern assemblages with known environmental parameters can yield quantitative reconstructions of past conditions, including sea-ice concentrations (SIC), which describes the fraction of ocean area covered by sea ice, and sea surface temperature (SST) (e.g., Imbrie and Kipp, 1971; Crosta et al., 1998; Esper and Gersonde, 2014; Ferry et al., 2015). These paleocological 'transfer functions' are empirically derived equations that allow for the calculation of

quantitative estimates of past environmental conditions. Two of the primary transfer functions used in reconstructing SIC and SST via diatoms are the Imbrie and Kipp Method (IKM) (Imbrie and Kipp, 1971), and the Modern Analog Technique (MAT) (Hutson, 1980). The MAT is the transfer function used in this thesis and will be the primary focus of this section. The Generalized Additive Model (GAM) (Ferry et al., 2015; Armand et al., 2017) is a relatively new statistical model that has been applied to fossil diatoms to estimate SIC and SST; however, the GAM is not as widespread as either the MAT or IKM.

The MAT provides a statistical comparison between a fossil assemblage and a range of modern assemblages across a variety of sample sites to find a 'modern analog', i.e., the modern assemblage existing today that is most similar to the fossil assemblage being examined (Hutson, 1980; Crosta et al., 1998). This comparison requires a reference dataset (also known as the training dataset) based on modern, core top diatom assemblages and their respective environmental parameters, such as SST and SIC. The MAT then calculates a dissimilarity coefficient based on the squared chord and/or log distance, which is a measure of the degree of dissimilarity between the fossil assemblages and modern reference assemblages (Prell, 1985). The modern analogs that are selected as the most similar then provide estimates of environmental parameters that are the best match to the fossil assemblage, thus allowing for quantitative reconstruction estimates with associated errors.

Crosta et al. (1998) found that the IKM, which is a similar transfer function based on Q-mode factor analysis, produces similar quantitative estimates as the MAT, although the IKM approach has a tendency to overestimate sea-ice coverage relative to the MAT. The MAT was also found to have other advantages over the IKM, including: [1] it can be applied directly to the fossil assemblage without the need for a factor analysis; [2] new reference data can easily be added to the training dataset without the need of recalculating the transfer function equation (as is the case with IKM); and [3] uncommon species play as important of a role as common species in the reconstruction of past environments (Crosta et al., 1998). Many groups maintain that the MAT provides the most robust estimates (e.g., Crosta et al., 1998; Esper & Gersonde, 2014), although new work has suggested that the relatively new GAM provides the most accurate estimates of sea-ice extent and sea-surface temperature changes (e.g., Armand et al., 2017). Ferry et al. (2015) compared the MAT and GAM estimates and found that the MAT underrepresented sea ice estimates relative to the GAM, although results were comparable. Despite this

debate, there is good evidence that the MAT produces robust estimates for diatom-based sea ice reconstructions (e.g., Crosta et al., 1998; Esper & Gersonde, 2014; Ferry et al., 2015), and at the time of writing, it remains a standard method for reconstructing WSIC and SSST.

Irrespective of the selected transfer function used to reconstruct past environmental conditions, all rely on several fundamental assumptions, including that: [1] a multivariate approach provides better estimates than a single-species approach (Sachs, 1973); [2] species assemblages are systematically related to the environmental parameters of interest, such as sea ice coverage or temperature (Imbrie & Kipp, 1971; Sachs, 1977); and [3] that the same relationships between modern environmental parameters and species assemblages exist today as they did in the past, and that species evolution has not dramatically altered morphology or environmental parameters[1].

1.2.3 Marine Geochemistry & Biogenic Fluxes

The use of geochemistry in paleoclimatology is particularly useful when reconstructing past marine environments. Observations of today's ocean and sedimentary chemistry allows for an understanding of processes that govern the distribution of heat, salt, nutrients, and the partitioning of isotopes throughout the ocean. Assuming the processes controlling sedimentary geochemistry were the same in the past as they are today, researchers are able to analyze the geochemical composition of fossils and other components of marine sediment cores to reconstruct changes in global climate, ocean circulation, and biological productivity. The geochemistry used throughout this thesis focuses primarily on estimating the biogenic components of marine sediments (i.e., those

[1] This assumption is supported by glacial-interglacial changes in diatom assemblages across the Southern Ocean, which show coherent changes in assemblages during periods of climatic change obtained from independent proxy records. For example, similar diatom species assemblages and diagnostic species (e.g., sea ice diatoms) appear in Southern Ocean marine cores during the LGM and MIS 6 (e.g., Crosta et al., 2004; Jones et al., 2022) at the same time as other independent proxy records suggest cooling and sea-ice expansion (EPICA Dome C deuterium (δD), sea salt sodium (ssNa) records, etc.). The same patterns and assemblages occurring across the Southern Ocean in concert with independent proxy records strongly suggest that these assemblages have maintained a consistent relationship at least over the last glacial-interglacial cycle. Additionally, the coherent response of the diatom assemblages and the general lack of 'non-analog" conditions – i.e., when one species would have evolved to change habitat while others did not – suggests that evolution has not been a driving force of changes to diatom assemblages over the late Pleistocene time period covered by this thesis.

produced by previously living organisms), specifically carbonate and opal, and uses the isotope geochemistry of fossil foraminiferal shells as a means of reconstructing sediment ages (planktonic foraminifera) and water mass geometry (benthic foraminifera) (outlined below in Section 1.3).

1.2.3.1 Oxygen Isotopes

Our understanding of past changes in the hydrological cycle can be reconstructed using two stable isotopes of oxygen, ^{16}O and ^{18}O. The differences in the atomic masses of these two isotopes reflect differing numbers of neutrons in the nucleus. The hydrological cycle moves these isotopes as H_2O throughout the different reservoirs (atmosphere, hydrosphere, and cryosphere) via phase transformations, which partitions the isotopes relative to their weight (Urey, 1947). For example, during evaporation, water containing ^{16}O is preferentially evaporated over water containing ^{18}O because of the additional energy required to evaporate heavier isotopes. The reverse is true of condensation – water containing ^{18}O is preferentially precipitated over ^{16}O because it is heavier. As H_2O is evaporated in some places and deposited as precipitation in others, some reservoirs become 'enriched' or 'depleted' depending on the direction of partitioning. This effect can be observed in precipitation falling at different latitudes, with higher latitudes having increasingly cooler temperatures and generally being further from the evaporative source region, therefore having an increasingly lighter oxygen isotope signature (Figure 2) (Dansgaard, 1964). The ratio of ^{18}O:^{16}O is known as the $\delta^{18}O$, which is calculated using the following equation:

$$\delta^{18}O = (((^{18}O/^{16}O_{sample} - {}^{18}O/^{16}O_{standard})/{}^{18}O/^{16}O_{standard}) \times 1000.$$

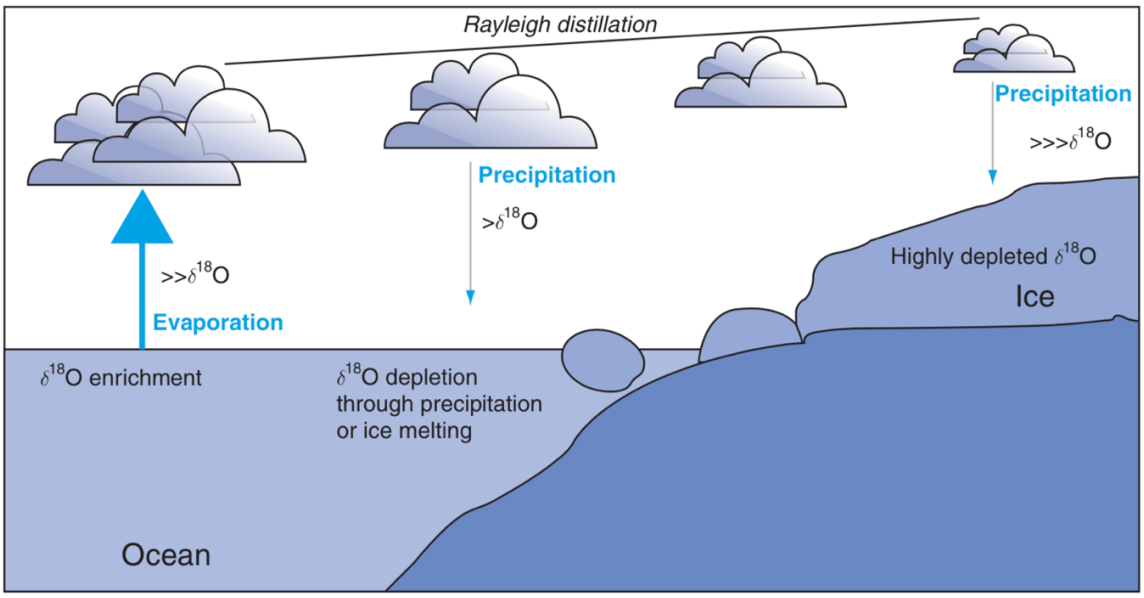

***Figure 2**: Infographic of Rayleigh distillation process, highlighting the fractionation of oxygen isotopes between the different reservoirs (Bassinot, 2007).*

This 'distillation' process (Urey, 1947) is captured by marine phytoplankton such as foraminifera, who incorporate the local oxygen isotope composition of seawater when they precipitate their shells made of calcium carbonate ($CaCO_3$). In addition to the local isotope composition, the $\delta^{18}O$ of the shell is also influenced by the *in-situ* temperature where the shell is formed, with lower temperatures resulting in more positive $\delta^{18}O$ values (Urey, 1947; Emiliani, 1955). Once the foraminifera die, they accumulate in the sediment over time and create a repository of past ocean $\delta^{18}O$ in the marine sediment. Interpreting the $\delta^{18}O$ requires a comparison to a standard, such as Pee Dee Belemnite (PDB, used in this research) (Craig, 1957) or the Vienna Standard Mean Ocean Water (V-SMOW) (Craig, 1961). These standards allow for a quantifiable deviation from a known value, against which all samples can be compared.

During periods when a significant amount of water is removed from the oceans and trapped as ice, higher values of ^{18}O relative to ^{16}O (i.e., ^{18}O enrichment) are found in the oceans. Furthermore, higher values of ^{16}O are found in the snow and ice at the poles due to the precipitation of nearly all ^{18}O en route to the cool polar regions (Emiliani, 1955; Dansgaard, 1964; Shackleton, 1967; Shackleton & Opdyk, 1973). Emiliani (1955) was the

first to interpret the changes in past temperatures and a glacial-interglacial cycle using the $\delta^{18}O$ from multiple marine cores across different oceanic basins (discussed further in Section 1.1.3.2). This process was later refined by Shackleton (1967), which set the stage for our modern use of oxygen isotope stratigraphy (i.e., Marine Isotope Stages) as a fundamental tool for marine paleoclimatology and age model construction, both of which are discussed later.

1.2.3.2 Carbon Isotopes

Carbon has two stable isotopes, ^{12}C and ^{13}C (the unstable isotope, ^{14}C, is discussed in Section 1.1.3.1). Like oxygen isotope fractionation, carbon isotopes fractionate according to their atomic mass and the ratio of ^{12}C to ^{13}C (known as the $\delta^{13}C$) can be interpreted from foraminiferal tests made of calcium carbonate ($CaCO_3$).

The carbon isotope fractionation process preferentially removes ^{12}C from the surface waters via primary production, enriching the surface-water dissolved inorganic carbon (DIC) pool in ^{13}C (Kroopnick, 1985). After the organisms die and sink towards the bottom of the ocean, bacterial remineralization enriches the deep ocean DIC with ^{12}C, resulting in a gradient of high $\delta^{13}C$ in nutrient-depleted surface waters and low $\delta^{13}C$ in nutrient-rich deep waters (Broecker and Peng, 1982; Bostock et al., 2004; Morée et al., 2018). Higher rates of surface productivity tend to lead to lower surface nutrient concentrations and higher $\delta^{13}C$ values, suggesting $\delta^{13}C$ of planktonic foraminifera can provide some information about surface ocean productivity. In the deep ocean, the $\delta^{13}C$ of benthic foraminifera provides clues to changes in the degree of deep ocean remineralization of phytodetritus, which results in nutrient enrichment (and lower $\delta^{13}C$ values); as deep-water ages and remineralized nutrients accumulation, the $\delta^{13}C$ of deep ocean DIC becomes progressively “lighter” (Broecker and Peng, 1982; Bostock et al., 2013). Thus, the $\delta^{13}C$ composition recorded in benthic foraminifera can be used to interpret past changes in ocean circulation and ventilation (Duplessy et al., 1988; Lynch-Stieglitz et al., 2007), water mass geometry (Pahnke & Zahn, 2005; Ronge et al., 2015), and nutrient concentrations (Morée et al., 2018).

1.2.3.3 Biogenic Opal

Biogenic opal, which refers to the hydrated silica ($SiO_2 \cdot nH_2O$) formed by diatoms, is a proxy of diatom productivity that has been used to reconstruct multiple aspects of past surface conditions (e.g., Bradtmiller et al., 2009; Chase et al., 2015). Biogenic opal concentrations and calculated burial rates can provide information on past frontal structures, rates of upwelling, nutrient availability, and overall net primary productivity (e.g., Cortese et al., 2004; Anderson et al., 2009; Bradtmiller et al., 2009; Chase et al., 2015). Understanding how these factors have changed is an important component of understanding the past efficiency of the biological pump (discussed in 1.2.2.2 Biological Mechanisms). A comprehensive overview and application of its use can be found in Chapter 3.

1.2.4 Age Models

Age models are means of estimating the age of each depth interval within a sediment core and can be constructed using a variety of different methods. For example, an age model can be constructed by counting individual layers (e.g., tree rings, ice core rings, or varved sediments), which could produce an age model with an annual resolution, or by radiometric dating (e.g., radiocarbon dating, uranium-thorium dating) of materials extracted from specific intervals within the core. The dated intervals provide specific "tie points," i.e., specific depth intervals that are "tied" to a known age. Once these tie points are established, one can estimate the age of each depth interval between the tie points, which then allows for the calculation of linear sedimentation rates (i.e., change in sedimentation (cm) between each dated interval (year) (see Figure 11 for an example).

Age model construction for marine sediment cores from the South Pacific Ocean can use tie points from a variety of sources, such as oxygen isotope stratigraphy, which "tunes" the $\delta^{18}O$ record to known changes in "orbital forcing", or cyclical variability in incoming solar radiation determined by changes in the Earth's tilt, precession, and orbital eccentricity (Imbrie et al., 1984; Martinson et al., 1987). Age models can also be constructed by combining multiple independent lines of evidence, such as radiometric dates and geochemical analyses. The age model used in this thesis for marine core TAN1302-96 (discussed in Chapter 2) is a combination of radiocarbon dates and the tuning of the oxygen isotope record to an oxygen isotope chronology known as LR04

benthic stack (Lisiecki and Raymo, 2005). The LR04 stack is an average of 57 globally distributed benthic $\delta^{18}O$ records showing distinct, recognizable cycles that have been assigned ages from today back to 5.3 million years based on orbital tuning (Lisiecki and Raymo, 2005). The LR04 stack provides a standardized record to which other cores can be tied with an associated error estimate of ± 4 ka (Lisiecki and Raymo, 2005). Using the $\delta^{18}O$ stratigraphy has the advantage of providing a globally averaged chronology. However, one important disadvantage is the time lag that exists between surface signals being transported and captured in the benthic record, which has been estimated to be as high as several thousand years (e.g., Skinner and Shackleton, 2005; Lisiecki and Stern, 2016).

In places where carbonate dissolution inhibits the preservation of foraminifera and the oxygen isotope stratigraphy is unavailable or unreliable, changes observed in proxy reconstructions, such as SST, can be tied to contemporaneous changes in other nearby records so long as they have well constrained and independent age models. For example, high-resolution Antarctic temperature reconstruction from the European Project for Ice Coring in Antarctica (EPICA) Dome C ice cores has a relatively well-constrained age model (e.g., Jouzel et al., 2007; Stenni et al., 2010; Bereiter et al., 2014) and is commonly used as the independent record to which others may be tied within the Southern Ocean. Matching marine core SST reconstructions with the EPICA Dome C temperature record assumes that changes in Antarctic temperature are contemporaneous with changes in the reconstructed SST record (e.g., Ghadi et al., 2020). Using the EPICA deuterium temperature record as a local reference record in the Southern Ocean has some benefits over using the LR04 benthic stack because it provides a direct correlation between surface temperature records and may circumvent some of the temporal lags associated with LR04 record described above. Determining the best approach to constructing a robust age model depends on the resolution of the of available data and the inclusion of associated errors, time lags, and other related variables.

The application of Bayesian statistics to age modelling represents a relatively new form of chronological interpretation that has gained significant traction over the last 20 years (Bayliss, 2015). The Bayesian approach allows tie points (e.g., radiocarbon dates) and associated uncertainty to be considered in conjunction with *a priori* information (e.g., stratigraphic or sedimentation context, or other tie points and their uncertainty), which

together can produce a statistically robust age model that considers all available data (e.g., Buck and Juarez, 2017).

Traditionally, age modelling software packages such as *Bacon* (Blaauw & Christen, 2011) and *OxCal* (Bronk Ramsey, 1995) have been documented to produce reliable age models when no major chronological issues, such as bioturbation or lateral sediment redistribution, are present (Lougheed & Obrochta, 2019). When more uncertainty exists around the reliability of tie points or sedimentation, software such as *Undatable* (used in this thesis) provides a more robust approach to producing an age vs. depth profile (Lougheed and Obrochta, 2019). *Undatable* uses an embedded Bayesian radiocarbon calibration software, known as *MatCal*, (Lougheed & Obrochta 2016), which allows the user to select their own calibration curve and reservoir age (discussed below). *Undatable* also uses a deterministic approach, assuming positive sedimentation, and allows the user to incorporate greater uncertainty into the depths of each tie points, ultimately creating a more robust age model.

1.2.3.1 Radiocarbon Dating and Calibration

Radiocarbon dating (^{14}C) is a type of radiometric dating which can be used to date organic materials. Radioactive ^{14}C is naturally produced in the atmosphere via cosmic rays and combines with oxygen to form CO_2. This CO_2 is then incorporated into autotrophs via photosynthesis and heterotrophs through their consumption of autotrophs in approximate equilibrium with the atmosphere (Taylor, 2000). Once the organism dies it stops consuming ^{14}C, which radioactively decays into ^{14}N at a known rate with a half-life of 5,730 years. Using an accelerator mass spectrometer, measurements of the amount of ^{14}C remaining in the sample allow for a comparison against the known ratio of ^{14}C:^{12}C that exists in living organisms, which can then be used to calculate the radiocarbon date associated with the time at which the material stopped consuming ^{14}C (i.e., its death).

Previously, ^{14}C was believed to have been created at a constant and known rate throughout history. However, in the 1950s, Hessel de Vires (1953) determined that both the amount of ^{14}C produced in the atmosphere and the exchange of carbon between reservoirs has changed throughout time, thus impacting the calculated radiocarbon date of a sample (de Vires, 1958; Reimer 2021). For example, radiocarbon calibration curves (i.e., an estimate of how the concentration of ^{14}C in the atmosphere has changed through

time) have been established by counting and measuring the ^{14}C in tree-ring records (dendrochronology) over the last ~12 ka (Stuiver & Braziunas, 1993). The annual growth rings of trees, specifically those of long-lived tree species such as the California bristlecone pine (*Pinus longaeva*), allow for the measured ^{14}C of each annual ring to be compared to an absolute date, which are calculated by counting the rings back in time (e.g., de Vires, 1958; Willis et al., 1960). Other independent dating techniques, including U/Th dating of corals, has extended the calibration curve back to ~50 ka (Bard et al., 1990; 1993; Burr et al., 1998).

The slow circulation and lack of homogenous mixing of the oceans results in a more complex interpretation of marine ^{14}C results than exists for terrestrial samples (e.g., Gordon & Harkness, 1992; Ascough et al., 2005). The 'marine reservoir effect' describes the process and offset between ^{14}C samples taken from the marine environment and the amount of radiocarbon in the atmosphere (Ascough et al., 2005; Alves et al., 2018). This effect results in marine samples appearing older than their contemporary terrestrial counterparts due to the time lag that exists for oceans to re-equilibrate with the atmosphere. The ^{14}C that enters the ocean can take hundreds of years or longer to circulate, which means a possibly longer residence time before being taken up by marine organisms and an 'artificially' older age (Alves et al., 2018). This effect is further complicated by the heterogenous mixing that occurs across the ocean basins, with high latitude oceans (especially the Arctic) seeing reservoir offsets of up to 800-1200 years (e.g., Stern and Lisiecki, 2013; Paterne et al., 2019). Because of this heterogenous reservoir effect, local marine reservoir ages (MRAs) are needed to ensure an accurate calibration of measured radiocarbon (Butzin et al., 2020).

1.2.3.2 Marine Isotope Stages

The pioneering work by Urey (1947) on oxygen isotope fractionation, and the later work by his student Cesare Emiliani, laid the foundation for the establishment of Marine Isotope Stages (MIS). Emiliani (1955) identified alternating warm and cold 'stages' through fluctuations in the $\delta^{18}O$ record from marine cores extracted across the Atlantic, Caribbean, and Pacific Oceans. He suggested that these shifts in $\delta^{18}O$ represented swings in global ocean temperature. The later work by Shackleton (1967) helped to correct the interpretations of marine $\delta^{18}O$ records by determining that dominant signal in the $\delta^{18}O$

record was the local isotopic signature as determined by the global ice volume, rather than the local temperature. This discovery ultimately refined the interpretations associated with Marine Isotope Stages and suggested that the warm and cold stages were correlated with periodic changes in the Earth's insolation established by Milankovitch (1920) (Hays et al. 1976; Imbrie and Imbrie, 1981; Mackensen et al. 1984; Lisiecki and Raymo, 2005).

The stages are numbered beginning with MIS 1 representing the Holocene (~12 ka BP to present), with stage numbers increasing as they extend back in time (Figure 3). Oddly numbered stages (MIS 1, 3, etc.) represent warm climatic intervals, while evenly numbered stages (MIS 2, 4, etc.) represent glacial climatic intervals (i.e., ice ages). As seen in Figure 3, stages can be subdivided into substages. For example, MIS 5 is subdivided into 5 substages, with 'odd' stages 5a, 5c, and 5e (or 5.1, 5.3, 5.5) representing warm intervals within the larger stage 5, and 'even' stages 5b and 5d (or 5.2, 5.4) representing cooler intervals within stage 5. This MIS numbering system extends back to 5.3 million years (Lisiecki & Raymo, 2005) and allows for a universal interpretation of past climates based on alternating warm and cool periods derived from benthic $\delta^{18}O$ records.

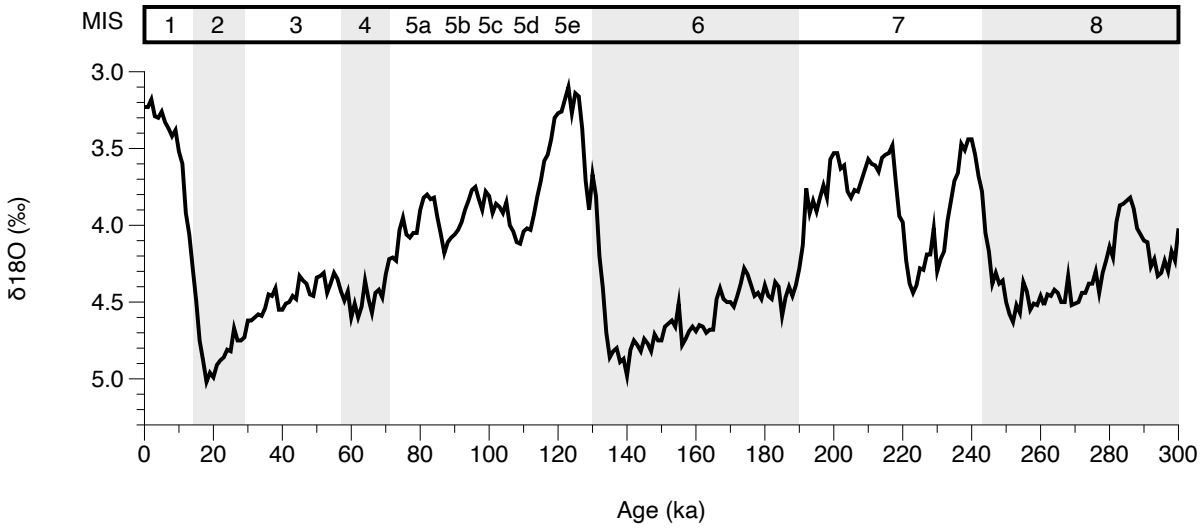

***Figure 3**: The most recent 300,000 years of the LR04 benthic $\delta^{18}O$ stack (Lisiecki & Raymo, 2005) showing alternate warm (odd MIS in white) and cold (even MIS shaded in grey) stages. Note that the Y-axis is inverted. Over 100 MIS have been identified, extending back to at least 5.3 million years (Lisiecki & Raymo, 2005; Ohno et al., 2016).*

1.3 The Southern Ocean

The Southern Ocean (SO) represents the polar waters circulating around Antarctica from ~40°S to the Antarctic coastal margin (~70°S) and as such links waters in the Atlantic, Pacific, and Indian Ocean basins (Figure 4) (e.g., Rintoul and Bullister, 1999; Bostock et al., 2013). The region comprises a complex series of oceanic gyres and fronts that separate water masses along multiple temperature, salinity, and nutrient concentration gradients. These fronts are heterogenous across the different ocean basins and vary from season to season (e.g., Graham and De Boer, 2013). The SO is classified as a high-nutrient-low chlorophyll (HNLC) area, where the cold and nutrient-rich Circumpolar Deep Water (CDW) upwells to the surface and supplies the region with high concentrations of nutrients vital to support primary production. Despite this high concentration of nutrients, the region observes relatively low rates of primary production likely due to limited light availability from sea ice coverage and a lack of bioavailable iron (e.g., Martin, 1990; Boyd, 2002).

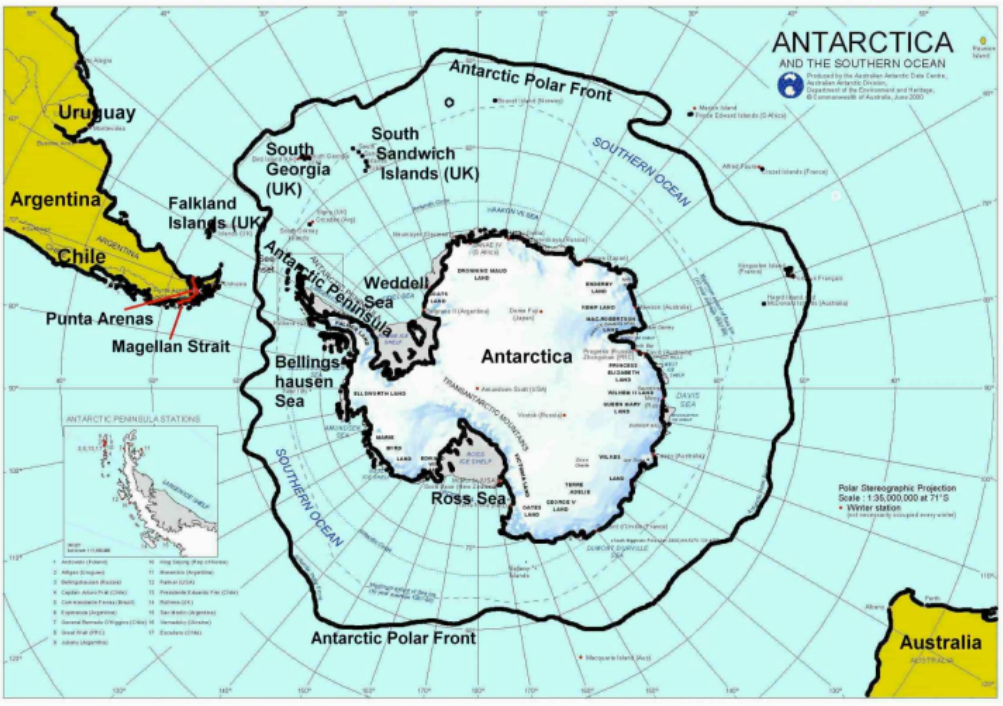

Figure 4: *Image of Antarctica and the average position of the Antarctic Polar Front (APF) (Wittmann, 2010).*

The Southern Ocean is a location of particular interest for paleoclimatology research because the region provides direct exchange pathways between all ocean basins, the deep ocean, and the atmosphere (Jaccard et al., 2013; Gottschalk et al., 2016). The physical and biological processes that occur within the Southern Ocean, such as sea-ice expansion, have been modeled to show that they are able to collectively account for the total CO_2 variability of ~80 ppm, although significant debate continues surrounding the specific contributions and timing of each mechanism (Kohfeld & Ridgwell, 2009; Kohfeld & Chase, 2017).

1.3.1 Antarctic Sea Ice

Sea ice is frozen surface water that forms annually during fall and winter months when surface waters reach freezing temperatures of around -1.9°C (Petrich & Eicken, 2017). In the Southern Ocean, annual sea ice coverage expands to approximately ~18.10^6 km^2 in September (Cavalieri et al., 2003; Cavalieri and Parkinson, 2008), extending to 62.4°S during austral winter and retreating to 65.9°S during the summer months in the southwestern Pacific Ocean (our study area) (Figure 5) (Ackley, 1981; Bostock et al., 2013). Despite rising annual temperatures, Antarctic sea ice expanded from 1979 until 2014 (Hobbs et al., 2016; Comiso et al., 2017) but has since begun to decrease in extent (Parkinson, 2019).

Sea ice plays an important role locally by influencing the freshwater flux into the sea ice margin during spring melt, which acts to stabilize and shoal the upper mixed layer and deposit bioavailable iron (Fe) into the meltwater (Person et al., 2020; Schultz et al., 2020). This stabilization and Fe deposition promotes primary production of diatoms along the ice margin, thereby influencing the biological pump (discussed below) (Pellichero et al., 2016).

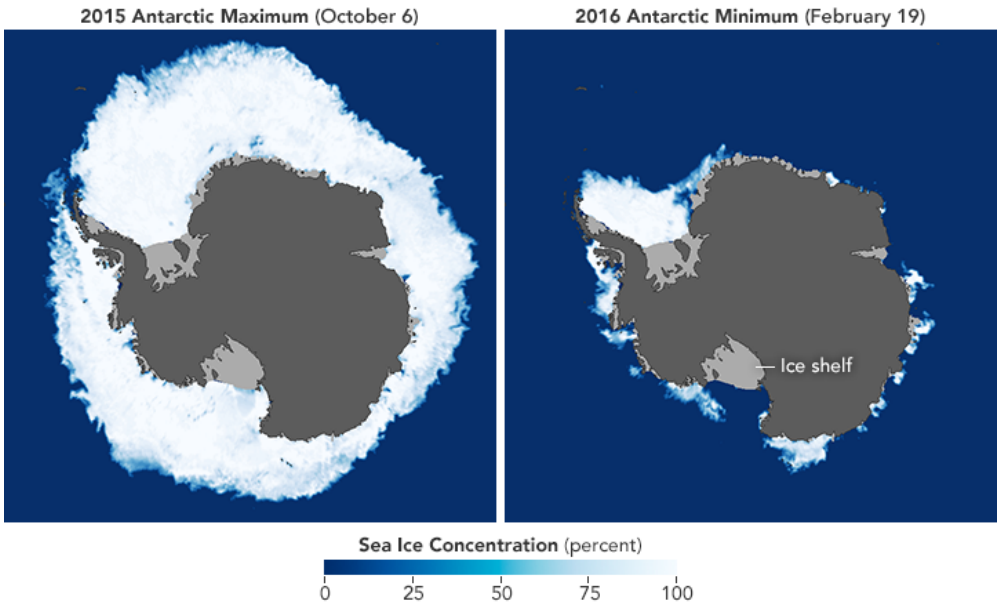

Figure 5: *Image of Antarctic sea ice during austral winter (left) and summer (right) between 2015 and 2016. Image retrieved from: https://earthobservatory.nasa.gov/features/SeaIce/page4.php*

Sea ice also plays an important physical role on a larger scale, influencing the radiative absorption of the region through the ice-albedo feedback (Kashiwase et al., 2017) and ocean overturning and the global thermohaline circulation (e.g., Bouttes et al., 2010; Ferrari et al., 2014). When sea ice forms, CO_2-rich brine is injected into the underlying surface waters and causes an increase in water mass density that in some regions (e.g., the Weddell Sea) leads to the formation of Dense Shelf Water (DSW) and Antarctic Bottom Water (AABW) (Rysgaard et al., 2011). This formation process helps to ventilate the deep ocean but can also enhance deep ocean stratification and stabilization (Toggweiler, 1999; Bouttes et al., 2010), leading to a reduction in mixing between abyssal and deep water masses (Ferrari et al., 2014). Increased sea-ice coverage also acts a physical barrier (i.e., sea ice 'cap'), thereby reducing the air-sea gas exchange of upwelled waters (Stephens & Keeling, 2000; Rysgaard et al., 2011). During the spring and summer melt, enhanced freshwater input along the sea ice margin causes a regional freshening and buoyancy gain, limiting the subduction of Antarctic Intermediate Waters (AAIW) and directly influencing intermediate water ocean circulation (Ronge et al., 2015; Jones et al., 2022).

1.3.2 Mechanisms Governing CO_2 Sequestration in the Southern Ocean

Given the direct exchange pathways between the deep ocean and the atmosphere and the influence that sea-ice growth and decay have on physical processes directly linked to ocean circulation, sea ice has been hypothesized to have played an important role in modulating glacial-interglacial CO_2 variability (e.g., Kohfeld and Chase, 2017; Stein et al., 2020). Of the sea ice related processes that have gained considerable attention within the scientific community, this thesis primarily focuses on the physical mechanisms, including the influence that sea ice has on reducing air-sea gas exchange (e.g., Stephens & Keeling, 2000; Maqueda & Rahmstorf, 2002), and through the alteration of circulation and ventilation (e.g., Toggweiler, 1999; Bouttes et al., 2010; De Boer & Hogg, 2014; Ferrari et al., 2014). Although not as central, this thesis also discusses the biological mechanisms associated with sea ice coverage, specifically its proposed influence on the redistribution of nutrients and associated primary productivity (e.g., Brzezinski et al., 2002; Matsumoto et al., 2002).

1.3.2.1 Physical Mechanisms

The sea ice 'capping' mechanism describes a reduction in air-sea gas exchange as a result of an increase in sea ice coverage (Stephens and Keeling, 2000). This sea ice cap was suggested to have essentially blocked the outgassing of carbon-rich waters that upwell, leading to an increase in the ocean's carbon storage. The initial box model by Stephens & Keeling (2000) proposed that this mechanism could account for up to 67 ppm of the ~80 ppm glacial-interglacial variability in atmospheric CO_2. However, subsequent work suggests a more conservative value of between 12 and 40 ppm, or 15-50% of the total (Maqueda & Rahmstorf, 2002; Kohfeld and Ridgwell, 2009). Other physical mechanisms link sea ice expansion to alterations in ocean circulation and related changes to the ventilation of the deep ocean (e.g., Bouttes et al., 2010; De Boer and Hogg, 2014; Ferrari et al., 2014). Some of these mechanisms have been suggested to account for the entire 80 ppm drawdown (e.g., Toggweiler, 1999). The fundamental principles underlying these hypotheses rely on the rearrangement of water masses that ultimately caused more carbon to be sequestered in the deep ocean for longer periods of time. For example, the hypothesis outlined in Ferrari et al. (2014) suggests that enhanced sea-ice coverage led to a shoaling in the depth of the maximum density gradient between deep and abyssal

water masses, which ultimately led to an expansion of the deep, carbon-rich water masses known as Antarctic Bottom Water (AABW) (Figure 6).

Importantly, the physical processes involving sea ice expansion, capping of air-sea gas exchange, and alteration of circulation and ventilation, are fundamentally linked. As such, they can operate together (either simultaneously or delayed) to enhance the relative contribution of sea ice to glacial-interglacial CO_2 variability. For example, Stein et al. (2020) suggest that the combined effects of reduced vertical mixing and sea ice capping can account for 40 ppm of the total 80 ppm reduction, with the reduced vertical mixing (accounting for 30 ppm) occurring earlier in the glacial cycle compared to capping (accounting for an additional 10 ppm), which occurred only once sea ice had expanded sufficiently.

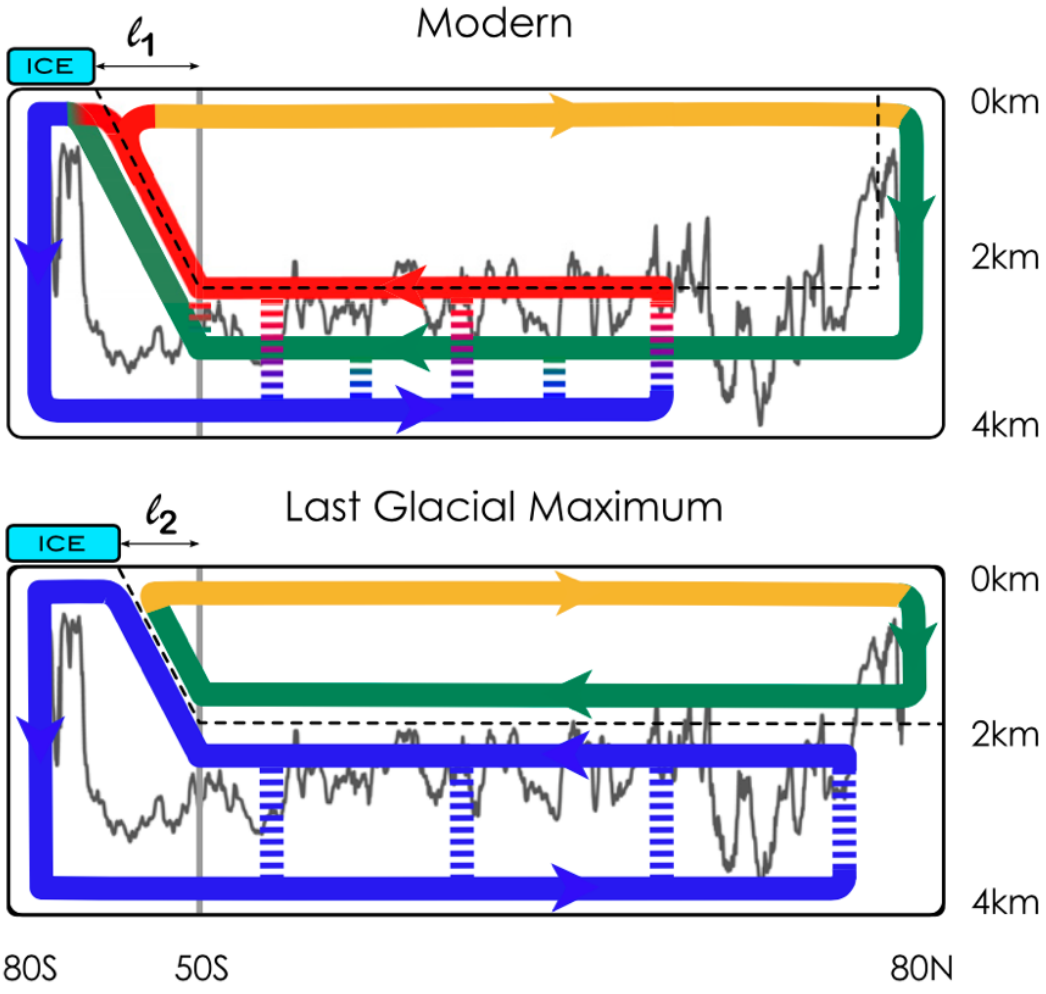

***Figure 6**: Reorganization of deep water masses between Modern and the Last Glacial Maximum conditions, in response to sea ice growth. The expansion of summer sea ice causes the shoaling of the isopyncnal (black dashed line) that separates the upper and lower overturning limbs. The shoaling of the upper limb above the maximum height of the bathymetric features reduces the upward diapycnal mixing, helping sequester carbon in the deep ocean (Ferrarri et al. 2014).*

1.3.2.2 Biological Mechanisms

The role of biological productivity can also have a significant impact on atmospheric CO_2 concentrations (Martin et al., 1990; Sigman and Boyle, 2000). The "biological pump" represents the removal of carbon and inorganic nutrients from the surface waters through photosynthesis and the subsequent 'pumping' of that carbon into the deep ocean via gravitational settling (Figure 7). Changes in the strength of the biological pump are thought to play an important role in influencing global atmospheric CO_2 concentrations (Anderson et al., 2002; Stukel and Ducklow, 2017). Today in the Southern Ocean, the biological pump operates inefficiently as the supply of nutrients to surface waters exceeds nutrient utilization due to restricting environmental parameters, such as limited bio-available iron and sea ice coverage (e.g., Boyd, 2002; Chase et al., 2015; Sigman et al., 2021). Past changes in the efficiency of the biological pump have been invoked to explain a significant portion of the glacial-interglacial difference in CO_2; however, numerous studies suggest that the effects of enhanced biological productivity only reached its full extent during the full glacial when dust deposition to the ocean was the greatest (Kohfeld et al., 2005; Kohfeld and Chase, 2017).

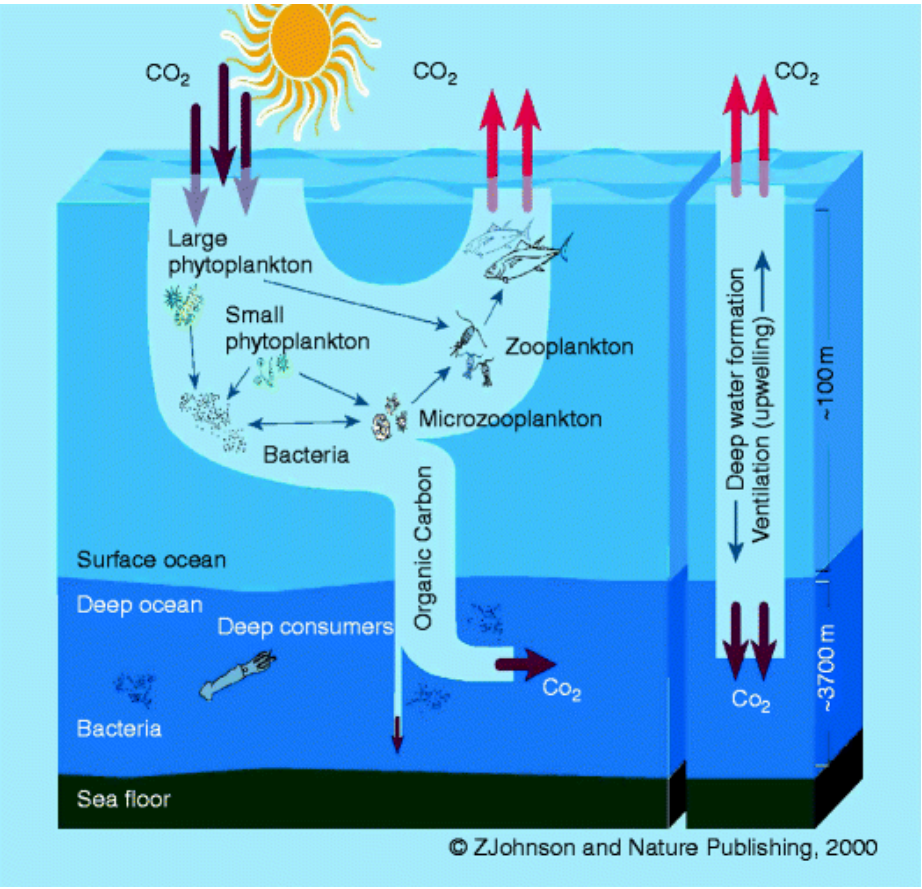

***Figure 7**: Depiction of the processes driving the biological pump (Boyd, 2012).*

One hypothesis linking sea ice expansion to changes in biological and glacial-interglacial CO_2 variability is the 'Silicic Acid Leakage Hypothesis' (SALH), first suggested by Brzezinski et al. (2002) and Matsumoto et al. (2002). The premise of SALH is that excess silicic acid ($Si(OH)_4$) was 'leaked' from the Southern Ocean during glacial times. This $Si(OH)_4$ was entrained into intermediate waters and carried to the low and mid latitudes where a lack of silicic acid limits diatom growth and favours the production of carbonate-based organisms. The leakage of silicic acid could have been caused several factors, including: [1] expanded sea ice coverage, which decreased the consumption of silicic acid in the modern day Southern Ocean and allowed for the export of silicic acid (Chase et al., 2015); and [2] enhanced iron (Fe) deposition, which reduced the Si:N uptake ratio and allowed for excess $Si(OH)_4$ to be exported to the rest of the ocean via

intermediate waters. The additional supply of $Si(OH)_4$ to the mid and low latitudes is proposed to have allowed diatoms to outcompete carbonate-based organisms in these regions, which would have led to a net-CO_2 drawdown (Matsumoto et al., 2014). This hypothesis is discussed in further detail in Chapter 3.

1.3.3 Sea Ice: Past Reconstructions

International collaborative efforts have attempted to bring together multiple proxies in order to map changes in the surface ocean conditions during the last glacial period, including the Climate: Long range Investigation, Mapping, and Prediction (CLIMAP) project in the 1970s (CLIMAP 1976; 1981) and the more recent Multiproxy Approach for the Reconstruction of the Glacial Ocean surface (MARGO) Project (MARGO, 2009). The CLIMAP project developed the first spatially extensive circumantarctic SST and WSIC estimates during the Last Glacial Maximum (LGM). Since then, numerous studies have updated these estimates as new data and refined methodology have become available (e.g., Cooke and Hays, 1982; Gersonde et al., 2005; Benz et al., 2016).

Significant attention has been placed on reconstructing winter sea-ice extent during the LGM. Gersonde et al. (2005) used 122 sediment cores for the Atlantic, Pacific, and Indian sectors of the Southern Ocean and estimated that winter sea ice expanded by approximately 5-10° latitude (depending on the sector) during the last glacial period compared with today. This equatorward expansion corresponds to a near doubling of current sea-ice extent (Figure 8) (Lhardy et al., 2021; Green et al., 2022). Other notable reconstructions, including the work by Allen et al. (2011) and Xiao et al. (2016) in the South Atlantic, and Benz et al. (2016) in the Pacific Oceans, have contributed additional data and helped constrain LGM winter sea-ice extent and SST across the Southern Ocean, while Holloway et al. (2017) and Chadwick et al. (2021) have contributed important estimates focusing on the Last Interglacial, MIS 5e (~128 ka).

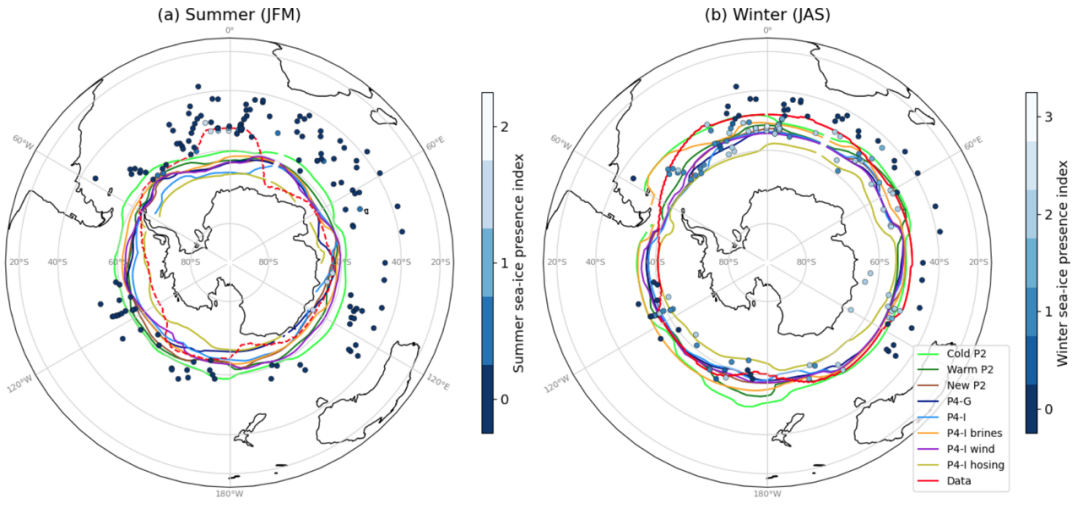

***Figure 8**: The current best estimates of last glacial maximum (LGM) summer sea ice extent (left) and winter sea ice extent (right) Lhardy et al. (2021).*

1.3.4 Sea Ice: Current Gaps & Future Work

While the LGM reconstructions have provided useful information on glacial conditions and the maximum extent of sea ice coverage during MIS 2, these reconstructions are unable to provide clarity on sea ice's contribution to carbon sequestration during the prolonged onset of a glacial period. Recent attention by the C-SIDE (Cycles of Sea-Ice Dynamics in the Earth System) working group has focused on producing full glacial-interglacial sea ice reconstructions over the last 130 ka across the Southern Ocean, as only a handful of published and quantitative records extend past the last glacial period (Gersonde and Zielinksi, 2000; Crosta et al., 2004; Schneider-Mor et al., 2012; Esper and Gersonde 2014a; Ghadi et al. 2020; Jones et al., 2022). The lack of reconstructions has resulted in significant uncertainty in attributing changes in glacial-interglacial CO_2 concentration to sea-ice expansion despite numerous studies suggesting that sea ice may play a significant role (e.g., Stephens & Keeling, 2000; Stein et al., 2020). Several new studies are aimed at understanding changes in Antarctic sea ice over a full glacial-interglacial cycle and are producing new quantitative estimates that extend between 0 and 130 ka (MIS6) (Ghadi et al., 2020; Chadwick et al., 2020; 2022; Jones et

al., 2022). Attention has also focused on reconstructing the sea-ice extent during the warm interglacial period of MIS 5e (~130 to 116 ka BP), which represents a warmer-than-present climate by ~1°C (Fischer et al., 2018). MIS 5e could be used as an analog for future warming scenarios and help to understand the fate of Antarctic sea ice – and its associated feedbacks - in a warmer climate (e.g., Chadwick et al., 2020; 2022).

Another important gap in our understanding is the lack of reliable summer sea ice (SSI) reconstructions (e.g., Esper and Gersonde, 2014). The main factor limiting past SSI reconstructions is the low sedimentation that occurs under perennial sea ice, although other factors such as enhanced dissolution and chronological uncertainties also contribute to difficulties in estimations (Gersonde and Zielinski, 2000; Gersonde et al., 2005). Past reconstructions, such as those in CLIMAP (1981), likely overestimated extent by placing the SSI edge around the present-day WSI edge. Our current estimates suggest that the LGM SSI extent was roughly 2-3 times greater than today (corresponding to 8-12 x 10^6 km^2) (Figure 8) (Gersonde et al., 2005; Lhardy et al., 2021; Green et al., 2022). The uncertainty around SSI extent is an important variable to constrain because it plays a key role in several physical oceanographic hypotheses, such as those by Ferrari et al. (2014), whose fundamental principles rest on an assumed SSI expansion of at least 5° latitude. As a result, the current lack of WSI estimates covering a full glacial-interglacial cycle and reliable SSI extents could lead to erroneous assumptions about past conditions and drivers of carbon sequestration.

Finally, significant uncertainty exists in our current sea-ice modelling predictions, such as those produced by CMIP 5 and 6 (Coupled Model Intercomparison Project) for the IPCC (Intergovernmental Panel on Climate Change) report (IPCC, 2013; Roach et al., 2020). The observed increase in sea-ice extent from 1979 to 2014 followed by the abrupt retreat of the ice edge since has been difficult to model, suggesting issues in our underlying understanding of sea ice dynamics (e.g., Maksym, 2019). As discussed earlier, sea ice exerts an important influence on the high latitude radiative budget, ocean circulation, and marine primary productivity, so our inability to reliably predict historical changes reduces confidence in future sea-ice scenarios. To begin resolving these uncertainties and refine our underlying understanding of sea-ice dynamics, we need to expand our understanding of past changes in sea-ice coverage and how changes in the Earth's climate affect, and are affected by, sea ice.

Chapter 2: Antarctic Winter Sea Ice Concentration and Sea Surface Temperature Reconstructions from TAN1302-96[2]

Jacob Jones[1], Karen E Kohfeld[1,2], Helen Bostock[3, 4], Xavier Crosta[5], Melanie Liston[6], Gavin Dunbar[6], Zanna Chase[7], Amy Leventer[8] Harris Anderson[7], Geraldine Jacobsen[9]

1 School of Resource and Environmental Management, Simon Fraser University, Burnaby, Canada
2 School of Environmental Science, Simon Fraser University, Burnaby, Canada
3 School of Earth and Environmental Sciences, The University of Queensland, Brisbane, Australia
4 National Institute of Water and Atmospheric Research (NIWA), Wellington, New Zealand
5 Université de Bordeaux, CNRS, EPHE, UMR 5805 EPOC, Pessac, France
6 Antarctic Research Centre, Victoria University of Wellington, Wellington, New Zealand
7 Institute of Marine and Antarctic Studies, University of Tasmania, Hobart, Australia
8 Geology Department, Colgate University, Hamilton, NY, USA
9 Centre for Accelerator Science, Australian Nuclear Science and Technology Organisation, Lucas Heights, NSW, Australia

Author Contributions

Study conception and design was completed by KK and HB, and project management was handled by JJ. Diatom identification was completed by JJ. Diatom-based transfer function was completed by XC. Age model construction was completed by HA and HB. Supporting data collection was completed by JJ, KK, HB, XC, ML, GD, ZC, and AL. Data analysis and the interpretation of results was completed by JJ, KK, HB, XC, ZC, AL, HA, and GJ. Draft manuscript preparation and editing was completed by JJ, KK, HB, XC, GD, ZC, AL, HA, and GJ. All authors reviewed the results and approved the final version of the chapter.

2.0 Abstract

Sea ice expansion in the Southern Ocean is believed to have contributed to glacial-interglacial atmospheric CO_2 variability by inhibiting air-sea gas exchange and influencing the ocean's meridional overturning circulation. However, limited data on past sea ice coverage over the last 140 ka (a complete glacial cycle) have hindered our ability to link sea ice expansion to oceanic processes that affect atmospheric CO_2 concentration. Assessments of past sea ice coverage using diatom assemblages have primarily focused on the Last Glacial Maximum (~21 ka BP) to Holocene, with few quantitative reconstructions extending to the onset of glacial Termination II (~135 ka BP). Here we

[2] This thesis chapter has been published in *Climate of the Past* (available at https://cp.copernicus.org/articles/18/465/2022/). During the review process, an anonymous reviewer raised questions regarding the interpretation of the core's age model. An overview of this discussion and the author's response can be found in Appendix H.

provide new estimates of winter sea ice concentrations (WSIC) and summer sea surface temperatures (SSST) for a full glacial-interglacial cycle from the southwestern Pacific sector of the Southern Ocean using the Modern Analog Technique (MAT) on fossil diatom assemblages from deep-sea core TAN1302-96. We examine how the timing of changes in sea ice coverage relates to ocean circulation changes and previously proposed mechanisms of early glacial CO_2 drawdown. We then place SSST estimates within the context of regional SSST records to better understand how these surface temperature changes may be influencing oceanic CO_2 uptake. We find that winter sea ice was absent over the core site during the early glacial period until MIS 4 (~65 ka BP), suggesting that sea ice may not have been a major contributor to early glacial CO_2 drawdown. Sea ice expansion throughout the glacial-interglacial cycle, however, appears to coincide with observed regional reductions in Antarctic Intermediate Water production and subduction, suggesting that sea ice may have influenced intermediate ocean circulation changes. We observe an early glacial (MIS 5d) cooling and a weakening of meridional SST gradients between 42˚ to 59˚S throughout the region, which may have contributed to early reductions in atmospheric CO_2 concentrations through its impact on air-sea gas exchange.

2.1 Introduction

Antarctic sea ice has been suggested to have played a key role in glacial-interglacial atmospheric CO_2 variability (e.g., Stephens & Keeling, 2000; Ferrari et al., 2014; Kohfeld & Chase, 2017; Stein et al., 2020). Sea ice has been dynamically linked to several processes that promote deep ocean carbon sequestration, namely by: [1] reducing deep ocean outgassing by ice-induced 'capping' and surface water stratification (Stephens & Keeling, 2000; Rutgers van der Loeff et al., 2014), and [2] influencing ocean circulation through water mass formation and deep-sea stratification, leading to reduced diapycnal mixing and reduced CO_2 exchange between the surface and deep ocean (Toggweiler, 1999; Bouttes et al., 2010; Ferrari et al., 2014). Numerical modelling studies have shown that sea ice-induced capping, stratification, and reduced vertical mixing may be able to account for a significant portion of the total CO_2 variability on glacial-interglacial timescales (between 40-80 ppm) (Stephens & Keeling, 2000; Galbraith & de Lavergne, 2018; Marzocchi & Jansen, 2019; Stein et al., 2020). However, debate continues surrounding the timing and magnitude of sea ice impacts on glacial-scale carbon sequestration (e.g., Morales Maquede & Rahmstorf, 2002; Archer et al., 2003; Sun & Matsumoto, 2010; Kohfeld & Chase, 2017).

Past Antarctic sea ice coverage has been estimated primarily through diatom-based reconstructions, with most work focusing on the Last Glacial Maximum (LGM), specifically the EPILOG timeslice as outlined in Mix et al. (2001), corresponding to 23 to 19 thousand years ago (ka) before present (BP). During the LGM, these reconstructions

suggest that winter sea ice expanded by 7-10° latitude (depending on the sector of the Southern Ocean), which corresponds to substantial expansion of total winter sea-ice coverage compared to modern observations (Gersonde et al., 2005; Benz et al., 2016; Lhardy et al., 2021). Currently, only a handful of studies provide quantitative sea-ice coverage estimates back to the penultimate glaciation, Marine Isotope Stage (MIS) 6 (~194 to 135 ka BP) (Gersonde & Zielinksi, 2000; Crosta et al., 2004; Schneider-Mor et al., 2012; Esper & Gersonde 2014a; Ghadi et al. 2020). These studies primarily cover the Atlantic sector, with only one published sea ice record from each of the Indian (SK200-33 from Ghadi et al., 2020), eastern Pacific (PS58/271-1 from Esper & Gersonde, 2014a), and southwestern Pacific sectors (SO136-111 from Crosta et al., 2004). These glacial-interglacial sea ice records show heterogeneity between sectors in both timing and coverage. While the Antarctic Zone (AZ) in the Atlantic sector experienced early sea ice advance corresponding to MIS 5d cooling (i.e., 115 to 105 ka BP) (Gersonde & Zielinksi, 2000; Bianchi & Gersonde, 2002; Esper & Gersonde, 2014a), the Indian and Pacific sector cores in the AZ show only minor sea ice advances during this time (Crosta et al., 2004; Ghadi et al., 2020). The lack of spatial and temporal resolution has resulted in significant uncertainty in our ability to evaluate the timing and magnitude of sea ice change during a full glacial cycle across the Southern Ocean, and to link sea ice to glacial-interglacial CO_2 variability.

This chapter provides new winter sea ice concentration (WSIC) and summer sea surface temperature (SSST) estimates for the southwestern Pacific sector of the Southern Ocean over the last 140 ka BP. WSIC, which is a grid-scale observation of the mean state fraction of ocean area that is covered by sea ice over the sample period, and SSST estimates are produced by applying the Modern Analog Technique (MAT) to fossil diatom assemblages from sediment core TAN1302-96 (59.09°S, 157.05°E, water depth 3099 m). We place this record within the context of sea ice and SSST changes from the region using previously published records from SO136-111 (56.66°S, 160.23°E, water depth 3912 m), which has recalculated WSIC and SSST estimates presented in this study, and nearby marine core E27-23 (59.61°S, 155.23°E; water depth 3182 m) (Ferry et al., 2015). Using these records, we compare the timing of sea ice expansion to early glacial-interglacial CO_2 variability to test the hypothesis that the initial CO_2 drawdown (~115 to 100 ka BP) resulted from reduced air-sea gas exchange in response to sea ice capping and surface water stratification (Kohfeld and Chase, 2017). We then consider alternative

oceanic drivers of early atmospheric CO_2 variability and place our SSST estimates within the context of other studies to examine how regional cooling and a weakening in meridional SST gradients might affect air-sea disequilibrium and early CO_2 drawdown (Khatiwala et al., 2019). Finally, we compare our WSIC estimates with regional reconstructions of Antarctic Intermediate Water (AAIW) production and subduction variability using previously published carbon isotope analyses on benthic foraminifera from intermediate to deep-water depths in the southwest Pacific sector of the Southern Ocean, to test the hypothesis that sea ice expansion is dynamically linked to AAIW production and variability (Ronge et al., 2015).

2.2 Methods

2.2.1 Study Site and Age Determination

We reconstruct diatom-based WSIC and SSST using marine sediment core TAN1302-96 (59.09°S, 157.05°E, water depth 3099 m) (Figure 9). The 364 cm core was collected in March 2013 using a gravity corer during the return of the *RV Tangaroa* from the Mertz Polynya in Eastern Antarctica (Williams et al., 2013). The core is situated in the western Pacific sector of the Southern Ocean, on the southwestern side of the Macquarie Ridge, approximately 3-4° south of the average position of the Polar Front (PF) at 157°E (Sokolov & Rintoul, 2009).

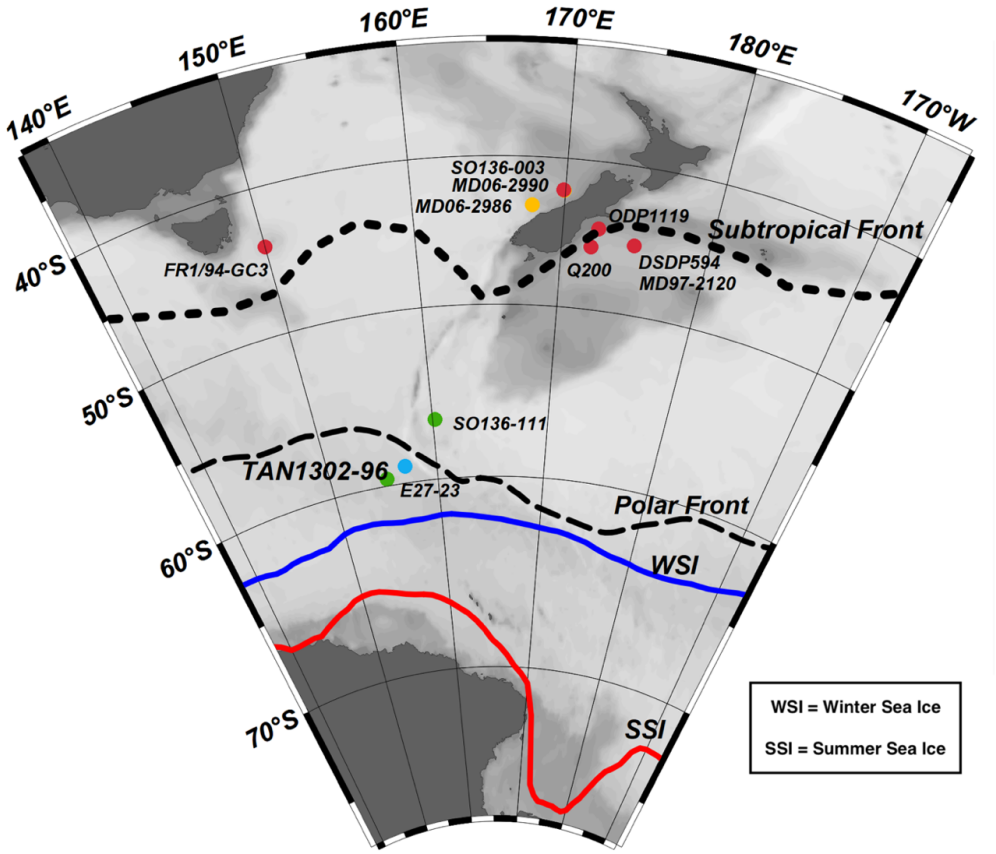

***Figure 9**: Map of the southwestern Pacific sector of the Southern Ocean including the study site, TAN1302-96 (blue circle), and additional published cores providing sea ice extent data, SO136-111 and E27-23 (green circles), SST reconstructions (red circles), and $\delta^{13}C$ of benthic foraminifera (yellow circles). Note that some cores may not appear present in the figure because of their proximity to other cores. Data for all cores are provided in Table 2. Dashed lines show the average location of the Subtropical and Polar Fronts (Smith et al., 2013; Bostock et al., 2015), and red and blue lines show mean positions of modern summer sea ice (SSI) and winter sea ice (WSI) extents, respectively (Reynolds et al., 2002; 2007).*

The age model for TAN1302-96 (Figures 10 and 11) was based on a combination of radiocarbon dating of mixed foraminiferal assemblages and stable oxygen isotope stratigraphy on *Neogloboquadrina pachyderma* (180-250 μm). Seven accelerator mass spectrometry (AMS) ^{14}C samples were obtained (Table 4 in Appendix A) and consisted of mixed assemblages of planktonic foraminifera (*N. pachyderma* and *Globigerina bulloides,* >250 μm). Three of the seven radiocarbon ages (NZA 57105, 57109, and 61429) were previously published in Prebble et al. (2017), and four additional samples (OZX 517-520) were added to improve the dating reliability (Table 4 in Appendix A). OZX 519 and OZX 520 produced ages that were not distinguishable from background (>57.5 ka BP) and were

subsequently excluded from the age model. The TAN1302-96 oxygen isotopes were run at the National Institute of Water and Atmospheric Research (NIWA) using the Kiel IV individual acid-on-sample device and analysed using Finnigan MAT 252 Mass Spectrometer. The precision is ±0.07% for $\delta^{18}O$ and ±0.05% for $\delta^{13}C$.

The age model was constructed using the 'Undatable' MATLAB software by bootstrapping at 10% and using an x-factor of 0.1 (Lougheed & Obrochta, 2019), which scales Gaussian distributions of sediment accumulation uncertainty (Table 5 in Appendix A). Below 100 cm, 9 tie points were selected at positions of maximum change in $\delta^{18}O$ and were tied to the LR04 benthic stack (Lisiecki & Raymo, 2005) (Figure 10; Table 5 in Appendix A). Uncertainty associated with stratigraphic correlation to the LR04 stack has been estimated to be ± 4 ka (Lisiecki & Raymo, 2005). We used a conservative marine reservoir age (MRA) for radiocarbon calibration of 1000 +/- 100 years, in line with regional estimates in Paterne et al. (2019) and modelled estimates by Butzin et al. (2017; 2020). The age model shows that TAN1302-96 extends to at least 140 ka BP, capturing a full glacial-interglacial cycle. Linear sedimentation rates (LSR) in TAN1302-96 were observed to be higher during interglacial periods, averaging ~3.5 cm ka^{-1}, compared to glacial periods, averaging ~2.5 cm ka^{-1}. It is worth noting that there can be significant MRA variability over time due changes in ocean ventilation, sea ice coverage, and wind strength, specifically in the polar high latitudes (Heaton et al., 2020), and as a result, caution should be taken when interpreting the precision of radiocarbon dates. For more information on age model construction and selection, refer to Appendix H.

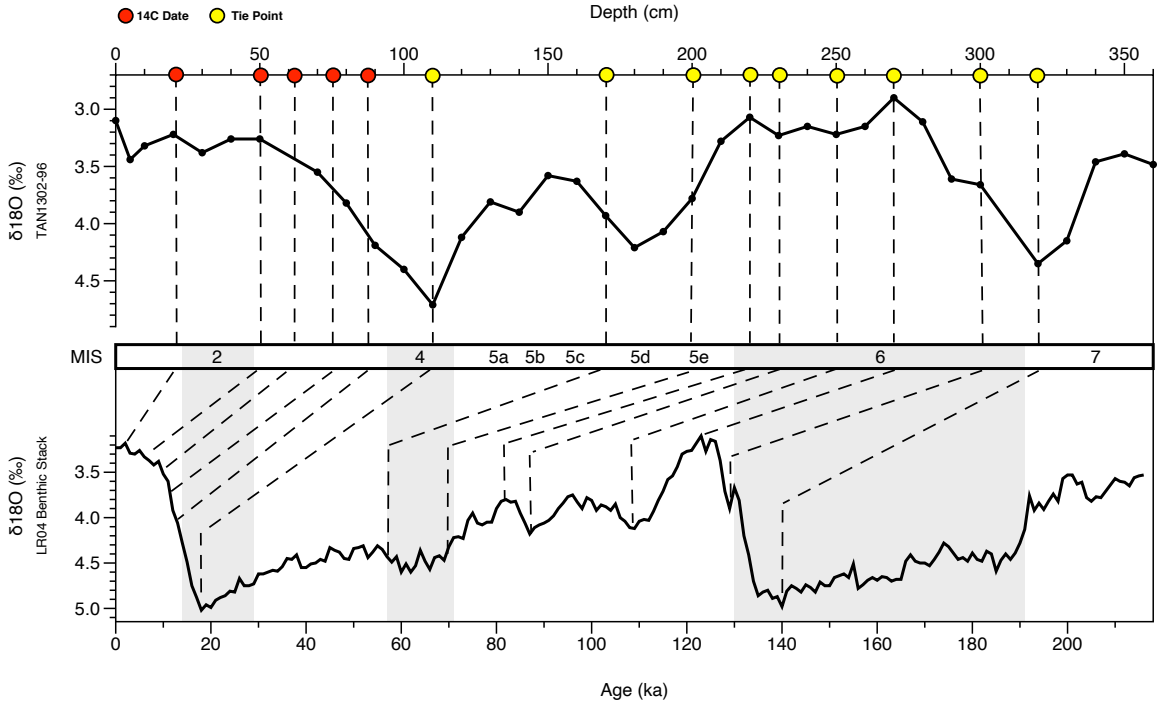

Figure 10: *Age model of TAN1302-96. Red circles indicate the depth of AMS ^{14}C samples and yellow circles indicate tie points between the TAN1302-96 oxygen isotope stratigraphy and the LR04 benthic stack (Lisiecki & Raymo, 2005). Two radiocarbon ages, OZX 519 & 520 (at 130 and 170 cm, respectively), were not included in the age model as they produced dates that were NDFB (not distinguishable from background).*

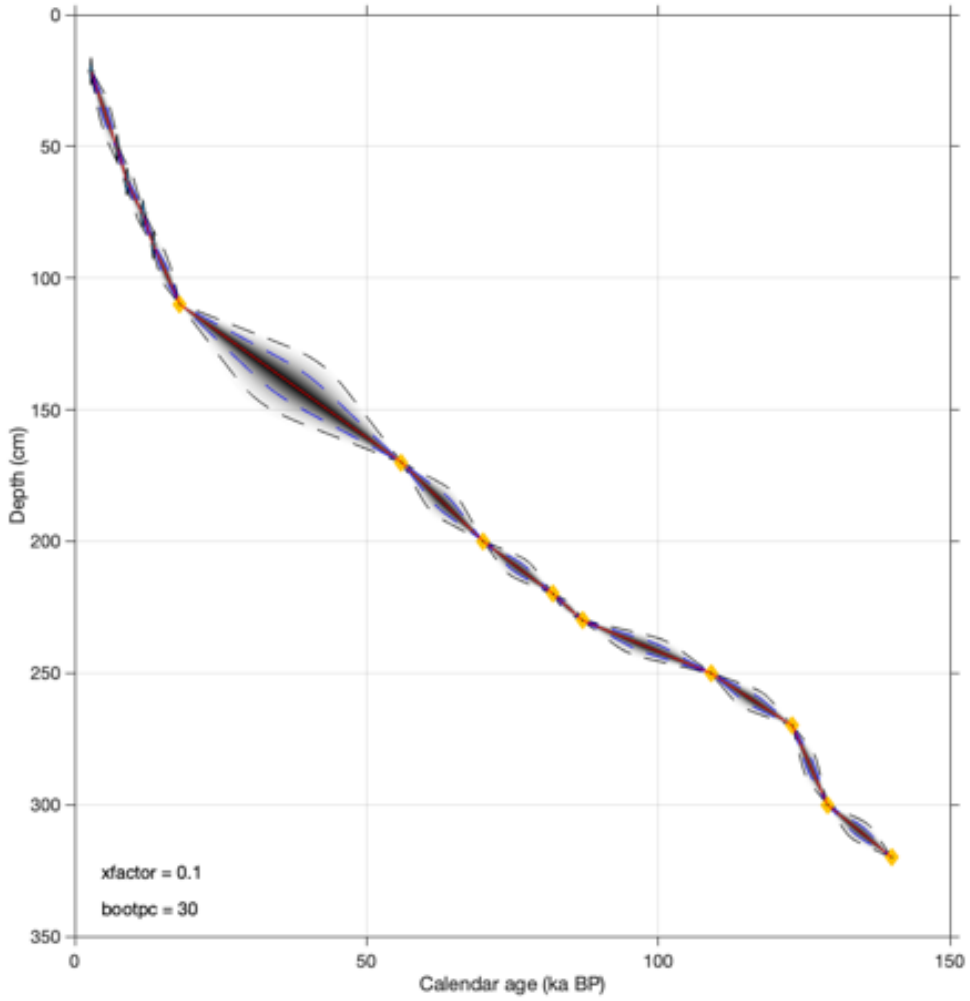

***Figure 11**: Age model of TAN1302-96. Tie points are depicted as yellow dots and grey shading represents associated uncertainty between tie points. The age model used a marine reservoir calibration of 1000 +/- 100 years.*

2.2.2 Diatom Analysis

TAN1302-96 was sampled every 3-4 cm throughout the core except between 130-180 cm, where samples were collected every 10 cm due to limited availability of sample materials (Table 6 in Appendix A). Diatom slide preparation followed two procedures. The first approach approximated the methods outlined in Renberg (1990), while the second followed the protocol outlined in Warnock & Scherer (2015). To ensure there were no

biases between preparation techniques, results from each technique were first visually compared followed by a comparison of sample means (see Figure 22 in Appendix B). No biases in the data were observed between methods.

The first procedure was conducted at Victoria University of Wellington and Simon Fraser University on samples every 10 cm throughout the core. Sediment samples contained high concentrations of diatoms with little carbonaceous or terrigenous materials, so no dissolving aids were used. Instead, approximately 50 mg of sediment was weighed, placed into a 50 ml centrifuge tube, and topped up with 40 ml of deionized water. Samples were then manually shaken to disaggregate sediment, followed by a 10-second mechanical stir using a vortex machine. Samples were then left to settle for 25 seconds. 0.25 mL of the solution was then pipetted onto a microscope slide from a consistent depth, where it was left to dry overnight. Once the sample had dried, coverslips were permanently mounted to the slide using Permount, a high refractive index mountant. Slides were redone if they contained too many diatoms and identification was not possible, or if they contained too few diatoms (generally <40 specimens per transect). Sediment sample weight was adjusted to achieve the desired dilution.

The second procedure was conducted at Colgate University on samples every 3-4 cm throughout the core. Oven-dried samples were placed into a 20 ml vial with 1-2 ml of 10% H_2O_2 and left to react for up to several days, followed by a brief (2-3 second) ultrasonic bath to disaggregate samples. The diatom solution was then added into a settling chamber, where microscope coverslips were placed on stages to collect settling diatoms. The chamber was gradually emptied through an attached spigot, and samples were evaporated overnight. Cover slips were permanently mounted onto the slides with Norland Optical Adhesive #61, a mounting medium with a high refractive index.

Diatom identification was conducted at Simon Fraser University using a Leica Leitz DMBRE light microscope using standard microscopy techniques. Following transverses, a minimum of 300 individual diatoms were identified at 1000x magnification from each sample throughout the core. Individuals were counted towards the total only if they represented at least one-half of the specimen so that fragmented diatoms were not counted twice. Identification was conducted to the highest taxonomic level possible, either to the species or species-group level. Taxonomic identification training was completed prior to analysis and was aided by the help of Dr. Crosta and Dr. Leventer, who provided

numerous identification materials, including (but not limited to): Fenner et al. (1976); Fryxell & Hasle (1976; 1980); Johansen & Fryxell (1985); Hasle & Syversten (1997); Cefarelli et al. (2010); and Wilks & Armand (2017). The relative abundances were calculated by dividing the number of identified specimens of a particular species by the total number of identified diatoms from the sample. It is assumed that some differences in species identification and taxonomic groupings exist between studies; however, final datasets and relative abundances were reviewed during the WSIC and SST estimation stages by Dr. Crosta. In addition, verification of species identification for the same sample was conducted at least once to ensure that consistent identification and counting was occurring.

Based on previously established taxonomic groups (Crosta et al., 2004), diatoms were grouped into one of three categories based on temperature preference and sea ice tolerance. The following main taxonomic groups were used (Table 1):

[1] Sea Ice Group: representing diatoms that thrive in or near the sea ice margin in SSTs generally ranging from -1 to 1 °C.

[2] Permanent Open Ocean Zone (POOZ): representing diatoms that thrive in open ocean conditions, with SSTs generally ranging from ~2 to 10 °C.

[3] Sub-Antarctic Zone (SAZ): representing diatoms that thrive in warmer sub-Antarctic waters, with SSTs generally ranging from 11 to 14 °C.

***Table 1**: Species comprising each of the diatom taxonomic groups (updated from Crosta et al., 2004).*

Sea Ice Group	POOZ Group	SAZ Group
Actinocyclus actinochilus	*Fragilariopsis kerguelensis*	*Azpeitia tabularis*
Fragilariopsis curta	*Fragilariopsis rhombica*	*Hemidiscus cuneiformis*
Fragilariopsis cylindrus	*Fragilariopsis separanda*	*Thalassionema nitzschioides var. lanceolata*
Fragilariopsis obliquecostata	*Rhizosolenia polydactyla* var. *polydactyla*	*Thalassiosira eccentrica*
Fragilariopsis ritscheri	*Thalassionema nitzschioides* (form 1)	*Thalassiosira oestrupii* gp.
Fragilariopsis sublinearis	*Thalassiosira gracilis* gp.	
	Thalassiosira lentiginosa	
	Thalassiosira oliverana	
	Thalassiothrix sp.	
	Trichotoxon reinboldii	

2.2.3 Modern Analog Technique

Past WSIC and SSST (January to March) were estimated for TAN1302-96 and recalculated for SO136-111 by applying the Modern Analog Technique (MAT) to the fossil diatom assemblages, as outlined in Crosta et al. (1998; 2020). Summer (January to March) SST was estimated because it is considered to be a better explanatory variable than spring or annual SST (Esper et al., 2010; Esper & Gersonde, 2014b). The MAT reference database used for this analysis is comprised of 249 modern core top samples (analogs) located primarily in the Atlantic and Indian sectors from ~40°S to the Antarctic coast. The age of the core tops included in the reference database have been assessed through radiocarbon and/or isotope stratigraphy when possible. Core tops were visually evaluated for selective diatom dissolution, so it is believed that sub-modern assemblages contain well-preserved and unbiased specimens. Modern SSST and WSIC were interpolated from the reference core locations using a 1°x1° grid from the World Ocean Atlas (Locarnini et al., 2013) through the Ocean Data View (Schlitzer, 2005). The MAT was applied using the "bioindic" package (Guiot & de Vernal, 2011) through the R-platform. Fossil diatom assemblages were compared to the modern analogs using 33 species or species-groups to identify the five most similar modern analogs using both the LOG and CHORD distance. The dissimilarity threshold, above which the fossil assemblages are considered to be too dissimilar to the modern dataset, is fixed at the first quartile of random distances (Crosta et al., 2020). The reconstructed SSST and WSIC are the distance-weighted mean of the climate values associated with the selected modern analog (Guiot et al., 1993; Ghadi et al., 2020). Both MAT approaches produce an R^2 value of 0.96 and a root mean square error of prediction (RMSEP) of ~1°C for SSST, and an R^2 of 0.93 and a RMSEP of 10% for WSIC (Ghadi et al. 2020). As outlined in Ferry et al., (2015), we consider <15% WSIC to represent an absence of winter sea ice, 15-40% WSIC as present but unconsolidated (i.e., patchwork or rafted), and >40% to represent consolidated (i.e., solid) winter sea ice.

2.2.4 Additional Core Data

We use additional published marine cores from the southwestern Pacific throughout this analysis (Table 2), for WSIC comparisons (E27-23), %AAIW calculations (MD06-2990/SO136-003, MD06-2986, and MD97-2120), and regional SST gradient comparisons (SO136-003, FR1/94-GC3, ODP 1119-181, DSDP 594, and Q200).

***Table 2**: Additional data on published marine cores used throughout this analysis.*

Core Name	Latitude	Longitude	Depth	Age Model Reference	Data Assessed	Data Source
TAN1302-96	59.09°S	157.05°E	3099 m	*This study*	WSIC; SST	*This study*
SO136-111	56.66°S	160.23°E	3912 m	Crosta et al. (2004)	WSIC; SST	Crosta et al. (2004); *recalculated in this study*
E27-23	57.65°S	155.23°E	3182 m	Ferry et al. (2015)	WSIC	Ferry et al. (2015)
MD06-2990	42.01°S	169.92°E	943 m	Ronge et al. (2015)	δ13C	Ronge et al. (2015)
MD06-2986	43.45°S	167.9°E	1477 m	Ronge et al. (2015)	δ13C	Ronge et al. (2015)
MD97-2120	45.54°S	174.94°E	121 0m	Pahnke & Zahn (2005)	δ13C	Pahnke & Zahn (2005)
SO136-003	42.3°S	169.88°E	958 m	Pelejero et al. (2006); Barrows et al. (2007)	δ13C; SST	Pelejero et al. (2006); Ronge et al. (2015)
FR1/94-GC3	44.25°S	149.98°E	2667 m	Pelejero et al. (2006)	SST	Pelejero et al. (2006)
ODP 1119-181	44.75°S	172.39°E	396 m	Wilson et al. (2005)	SST	Wilson et al. (2005); Hayward et al. (2008)
DSDP 594	45.54°S	174.94°E	1204 m	Nelson et al. (1985); Kowalski & Meyers (1997)	SST	Schaefer et al. (2005)
Q200	45.99°S	172.02°E	1370 m	Waver et al., 1998	SST	Weaver et al. (1998)

2.3 Results

2.3.1 TAN1302-96 Diatom Assemblage Results

In this core, fifty-one different species or species groups were identified, of which 33 were used in the transfer function. These 33 species represent >82% of the total diatom assemblages (mean of 92%). Permanent Open Ocean Zone (POOZ) diatoms made up the largest proportion of diatoms identified, representing between 72-91% of the assemblage (Figure 12), with higher values observed during warmer interstadial periods of MIS 1, 3, and 5. Sea ice diatoms made up the second most abundant group, representing between 0.5-7.5% of the assemblage, with higher values observed during cooler stadial periods (MIS 2, 4, and 6). The Sub-Antarctic Zone group had relatively low abundances, with higher values occurring during warmer interstadial periods (MIS 5 and the Holocene) and briefly during MIS 4 at ~65 ka BP.

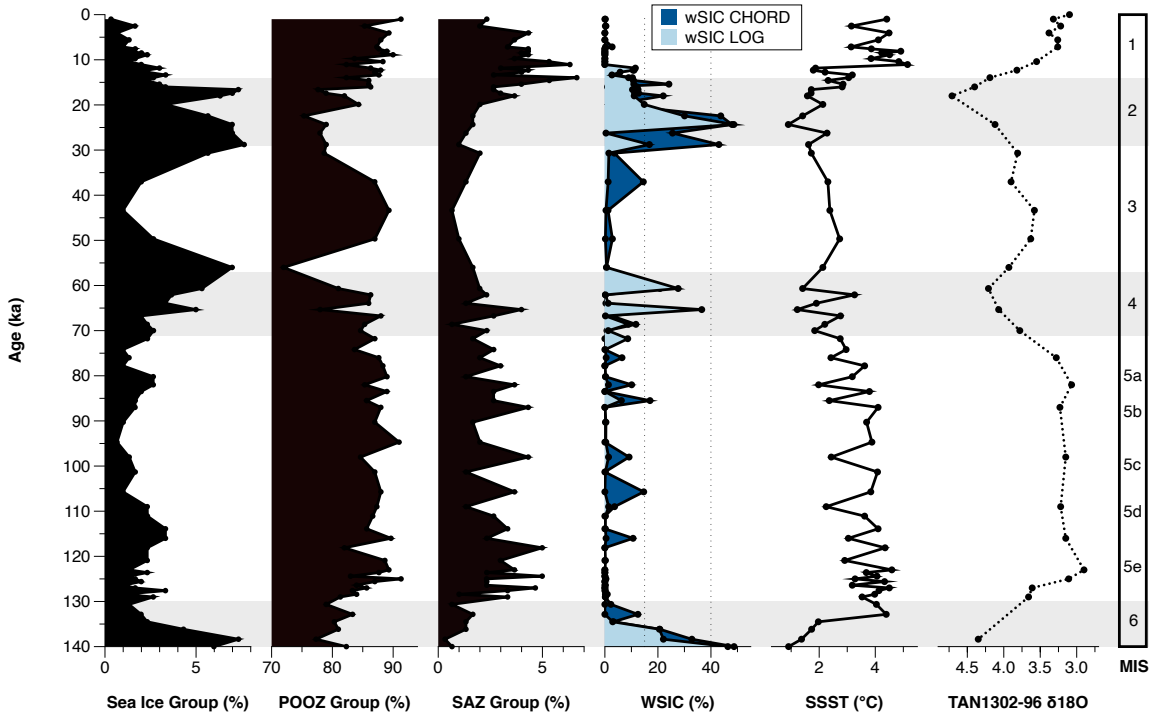

***Figure 12**: Diatom assemblages results from TAN1302-96 separated into % contribution from each taxonomic group (Sea ice Group, POOZ, and SAZ; see Table 1) over a full glacial-interglacial cycle. Using the Modern Analog Technique (MAT), winter sea ice concentration (WSIC) and summer sea surface temperature (SSST) were estimated and compared against the $\delta^{18}O$ signature of TAN1302-96.*

2.3.2 TAN1302-96 SSST and WSIC Estimates

There were no non-analog conditions (i.e., fossil assemblages that have no modern equivalent) observed in TAN1302-96 samples and all estimates were calculated on five analogs. Estimates of SSST and WSIC from both LOG and CHORD MAT outputs produced similar results (Figure 12). During Termination II, SSST began to rise from ~1°C at 140 ka BP (MIS 6) to ~4.5°C at 132 ka BP (MIS 5e/6 boundary). This warming corresponded with a decrease in WSIC from 48% to approximately 0% over the same time periods (Figure 12). Reconstructed SSST were variable throughout MIS 5e, reaching a maximum value of ~4.5°C at 118 ka BP, after which they declined throughout MIS 5. During this period of SSST decline, winter sea ice was largely absent, punctuated by brief periods during which sea ice was present but unconsolidated (WSIC = ~15% and 17% at

105 and 85 ka BP, respectively). During MIS 4 (71 to 57 ka BP), SSST cooled to between roughly 1°C and 3°C, and sea ice expanded to 36%, such that it was present but unconsolidated for intervals of a few thousand years. SSST increased slightly from 1.5°C at 61 ka BP (during MIS 4) to ~2.5°C at 50 ka BP (during MIS 3), followed by a general cooling trend into MIS 2. Sea ice appears to have been largely absent during MIS 3 (57 to 29 ka BP), although sampling resolution is low, but increased rapidly to 48% cover during MIS 2 where winter sea ice was consolidated over the core site. During MIS 2, SSST cooled to a minimum of <1°C at 24.5 ka BP. After 18 ka BP, the site rapidly transitioned from cool, ice-covered conditions to warmer, ice-free winter conditions during the early deglaciation. This warming was interrupted by a brief cooling around 13.5 ka BP, following which SSST quickly reached their maximum values of ~5°C at 11.5 ka BP and remained relatively high throughout the rest of the Holocene. Winter sea ice was not present during the Holocene.

2.3.3 SO136-111 SSST and WSIC Recalculation

In core SO136-111, the 33 species included in the transfer function represent values >79% of the total diatom assemblages (mean of 91%). There were no non-analog conditions observed in SO136-111 samples and all estimates were calculated on five analogs. Recalculated estimates of SSST and WSIC from both LOG and CHORD MAT outputs produced similar results for SO136-111 (Figure 13a, 13d). During Termination II, SSST rose from ~2°C at 137 ka BP (MIS 6) to a maximum value of 6°C at 125 ka BP (MIS 5e), corresponding to a rapid decline in WSIC from 37% to ~0% during the same period. SSST remained relatively high (between 4 and 5°C) from 125 ka BP until 115 ka BP where they declined to ~2°C. SSST remained variable from 110 ka BP until ~40 ka BP, fluctuating between ~2°C and 4°C. Winter sea ice was largely absent during MIS 5, with a brief period where sea ice was present but unconsolidated (WSIC = 17% at 84 ka). Beginning at ~76 ka BP, WSIC began to increase and continued throughout early MIS 4 to a maximum 36% at 69 ka BP. WSIC remained present but unconsolidated throughout most of MIS 3 and 2 with brief periods of absence (WSIC = <15%) lasting a few thousand years. SSST and WSIC reached their coolest values and highest concentration at 24.5 ka before SSST increased to ~5°C and stabilized throughout the Holocene, while WSIC declined to virtually 0% throughout the same period.

2.4 Discussion

2.4.1 Regional SSST and WSIC Estimates

The new WSIC and SSST estimates from TAN1302-96 and recalculated WSIC estimates from SO136-111 show a relatively coherent regional pattern (Figure 13). TAN1302-96 shows slightly higher concentrations during MIS 2 (max WSIC = 48% at 24.5 ka BP) and 4 (max WSIC = 37% at 65 ka BP) compared with SO136-111 (max WSIC = 35% at 24.5 ka BP and 36% at 68 ka BP, respectively), which can be explained by a more poleward position of TAN1302-96 relative to SO136-111. WSIC estimates in TAN1302-96 also appear to be more variable during MIS 4 compared to SO136-111, which may be a result of the differences in sampling resolution between the two cores. The estimates between cores differ during MIS 3, with seemingly lower WSIC in TAN1302-96 than in SO136-111, which might also result from the low sampling resolution in TAN1302-96 during this period. Overall, these cores show a similar and coherent history of sea ice over the last 140 ka BP.

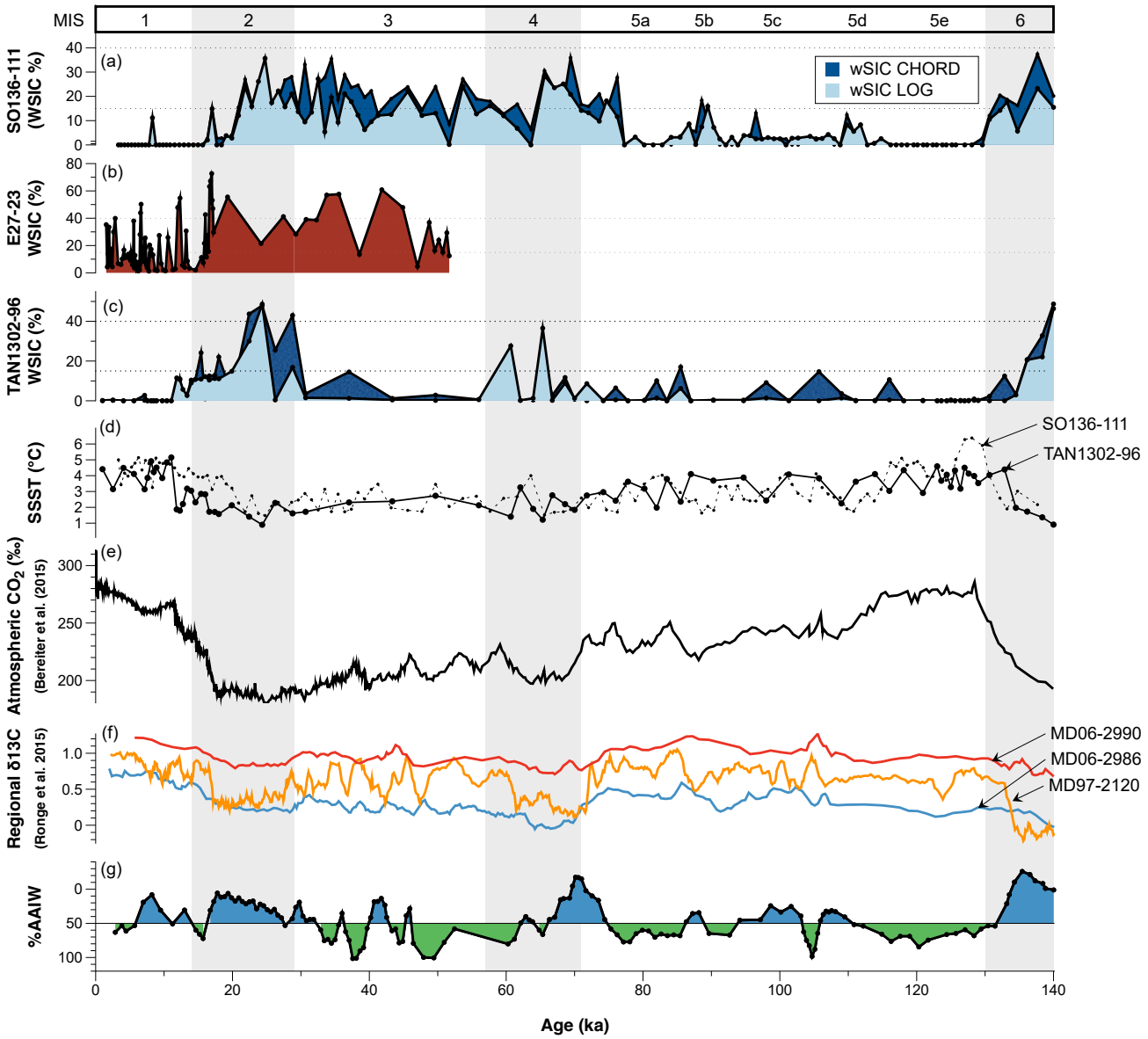

Figure 13: ***(a)*** *WSIC estimates using MAT from SO136-111 (recalculated in this study, see Appendix G);* ***(b)*** *WSIC estimates using GAM from E27-23 (Ferry et al., 2015);* ***(c)*** *WSIC estimates using MAT from TAN1302-96 (this study);* ***(d)*** *SSST estimates using MAT from TAN1302-96 (solid black line) and recalculated SSST for SO136-111 (black dotted line);* ***(e)*** *Antarctic atmospheric CO_2 concentrations over 140 ka BP (Bereiter et al., 2015);* ***(f)*** *$\delta^{13}C$ data from nearby cores MD06-2990/SO136-003, MD97-2120, and MD06-2986 (Ronge et al., 2015);* ***(g)*** *%Antarctic Intermediate Water (%AAIW) as calculated in Ronge et al. (2015), which tracks when core MD97-2120 was bathed primarily by AAIW (green) or Upper Circumpolar Deep Water (UCDW) (blue). Note that the %AAIW y-axis is inverted such that low %AAIW is represented in blue and high %AAIW is represented in green.*

When compared with E27-23 (Figure 13b), which is located only ~120 km to the southwest of TAN1302-96, the TAN1302-96 core shows lower estimates of WSIC, especially during MIS 3. During early and mid-MIS 2, both cores show similar WSIC estimates, while later in MIS 2 (~17 ka BP), E27-23 records a maximum WSIC of 72% compared to only 22% at TAN1302-96. A discrepancy between estimates is also observed during the Holocene, with E27-23 reporting sea ice estimates of up to nearly 50% during the mid-Holocene (~6 ka BP), while TAN1302-96 experienced values well below the RMSEP of 10%.

Possible explanations for the observed differences in WSIC estimates include: [1] differences in statistical applications; [2] lateral sediment redistribution; [3] differences in laboratory protocols; [4] differences in diatom identification/counting methodology; and [5] selective diatom dissolution. Of these explanations, we believe that [1] and [2] are the most likely candidates and are discussed below (for further discussion on [3], [4], and [5], see Appendix C).

The first possible explanation is the use of different statistical applications. Ferry et al. (2015) used a Generalized Additive Model (GAM) to estimate WSIC for both E27-23 and SO136-111, while we have used the MAT for TAN1302-96 and SO136-111. Ferry et al. (2015) provide a comparison of the WSI estimates for both the MAT (published in Crosta et al. 2004) and GAM from SO136-111, which show that the GAM tended to produce higher WSIC estimates relative to the MAT. This difference could indicate a small bias between the GAM and MAT estimations, although we believe it is unlikely that statistical approaches alone could explain the larger difference (i.e., 50%) observed between E27-23 and TAN1302-96 in this study.

The second possible explanation involves lateral sediment redistribution and focusing by the ACC. Sediment redistribution refers to the resuspension and lateral redeposition of sediments, which can result in erroneous interpretations of overlying waters and past environmental conditions. We estimated sediment focusing for E27-23 using ^{230}Th data from Bradtmiller et al. (2009) together with dry bulk density estimated using calcium carbonate content (Froelich, 1991). Both sedimentation rates and focusing factors (FF) for the E27-23 are relatively high (max. = ~35 cm ka^{-1} and 26, respectively) during the LGM and Holocene, which could influence the reliability of WSIC and SSST estimation (see Figure 23 in Appendix C). Several peaks in focusing occurring around 16,

12, and 3 ka BP appear to closely correspond to periods of peak WSIC (~67%, ~54%, and ~35%, respectively), suggesting a possible link. Lateral redistribution could artificially increase or decrease relative abundances of some diatom groups, which could lead to over- or under-estimations of sea ice coverage. Thorium analysis for TAN1302-96 is beyond the scope of this study; however, future work could help address this uncertainty.

2.4.2 The Role of Sea Ice on Early CO_2 Drawdown

Kohfeld & Chase (2017) hypothesized that the initial drawdown of atmospheric CO_2 (~35 ppm) during the glacial period of MIS 5d (~115 to 100 ka BP) was primarily driven by sea ice capping and a corresponding stratification of surface waters, which reduced the CO_2 outgassing of upwelled carbon-rich waters. This hypothesis is supported by several lines of evidence, including: [1] sea salt sodium (ssNA) archived in Antarctic ice cores, suggesting sea ice expansion near the Antarctic continent (Wolf et al., 2010); [2] $\delta^{15}N$ proxy data from the central Pacific sector of the Southern Ocean, suggesting increased stratification south of the modern-day Antarctic Polar Front (Studer et al., 2015); and [3] diatom assemblages in the Permanent Open Ocean Zone (POOZ) of the Atlantic sector, suggesting a slight cooling and northward expansion of sea ice during MIS 5d (Bianchi & Gersonde, 2002). Our data address this hypothesis by providing insights into early sea ice expansion into the polar frontal zone of the western Pacific sector.

Our data show that, in contrast to the Atlantic sector (Bianchi & Gersonde, 2002), there does not appear to be any evidence of sea ice expansion in the southwestern Pacific during MIS 5d at either the TAN1302-96 or SO136-111 core sites (Figure 13). Unfortunately, the lack of spatially extensive quantitative records extending back to Termination II limits our ability to estimate the timing and magnitude of sea ice changes for regions poleward of 59°S in the southwestern Pacific. We anticipate, however, that an advance in the sea ice edge, consistent with those outlined in Bianchi and Gersonde (2002), likely would have reduced local SST as the sea ice edge advanced closer to the core site. Indeed, the TAN1302-96 SSST record does show a decrease to ~2°C (observed at 108 ka BP), which quickly rebounded to ~4°C by ~102 ka BP (Figure 13). However, this SSST drop occurred roughly 7 ka BP after the initial CO_2 reduction, suggesting that the CO_2 drawdown event and local SSST reduction may not be linked. Thus, while we cannot rule out the possibility of modest sea ice advances or consolidation of pre-existing sea ice

(particularly to the south of the core sites), the quantitative WSI and SSST reconstructions suggest that sea ice cover over our core site was limited during glacial inception.

Given that sea ice was not at its maximum extent during the early glacial, it stands to reason that any reductions to air-sea gas exchange in response to the hypothetically expanded sea ice would not have been at its maximum impact either. Previous modeling work has suggested that the maximum impact of sea ice expansion on glacial-interglacial atmospheric CO_2 reductions ranged from 5 to 14 ppm (Kohfeld and Ridgwell, 2009). More recent modeling studies are consistent with this range, suggesting a 10-ppm reduction (Stein et al., 2020), while some studies even suggest a possible increase in atmospheric CO_2 concentrations due to sea ice expansion (Khatiwala et al., 2019). Furthermore, Stein et al. (2020) suggest that the effects of sea ice capping would have taken place after changes in deep ocean stratification had occurred and would have contributed to CO_2 drawdown later during the mid-glacial period. These model results, when combined with our data, suggest that even if modest sea ice advances did take place during the early glacial (i.e., MIS 5d), their impacts on CO_2 variability likely would have been modest, ultimately casting doubt on the hypothesis that early glacial CO_2 reductions of 35 ppm can be linked solely to the capping and stratification effects of sea ice expansion.

2.4.3 Other Potential Contributors to Early Glacial CO_2 Variability

The changes observed in WSIC and SSST from TAN1302-96 suggest that sea ice expansion was likely not extensive enough early in the glacial cycle for a sea ice capping effect to be solely responsible for early atmospheric CO_2 drawdown. This leaves open the question of what may have contributed to early drawdown of atmospheric CO_2. In terms of the ocean's role, we highlight three contenders: [1] a potentially non-linear response between sea ice coverage and CO_2 sequestration potential; [2] links between sea ice expansion and early changes in global ocean overturning, and [3] the impact of cooling on air-sea disequilibrium in the Southern Ocean.

The first possible explanation considers that not all sea ice has the same capacity to facilitate or inhibit air-sea gas exchange. We previously suggested that because sea ice was not at its maximum extent during MIS 5d, the contribution of sea ice on CO_2 sequestration would likely not be at its maximum extent either. However, this assumes a linear relationship between sea ice coverage and CO_2 sequestration potential. We know

that different sea ice properties, such as thickness and temperature, determine overall porosity, with thicker and colder sea ice being less porous and more effective at reducing air-sea gas exchange compared to thinner and warmer sea ice (Delille et al., 2014). It is therefore possible that if modest sea ice advances took place closer to the Antarctic continent (and were therefore not captured by TAN1302-96), they may have been more effective at reducing CO_2 outgassing either by experiencing some type of reorganization or consolidation, or through a change in properties such as temperature or thickness. It is also possible that sea ice coverage over some regions leads to more effective capping, while in other regions sea ice growth contributes only to marginal reductions in air-sea gas exchange. This, theoretically, could point to a non-linear response between sea ice expansion and CO_2 sequestration potential, and thus modest sea ice growth around the Antarctic continent could have contributed in part to the ~35 ppm initial CO_2 drawdown event. While this is theoretical and cannot be adequately addressed in this analysis, it is worthy of deeper consideration.

The second possible explanation involves changes in the global overturning circulation. Kohfeld and Chase (2017) previously examined the timing of changes in $\delta^{13}C$ of benthic foraminifera solely from the Atlantic basin and observed that the largest changes in the Atlantic Meridional Overturning Circulation (AMOC) coincided with the mid-glacial reductions in atmospheric CO_2 changes mentioned above. Subsequent work of O'Neill et al. (2020) examined whole-ocean changes in $\delta^{13}C$ of benthic foraminifera and noted that the separation between $\delta^{13}C$ values of abyssal and deep ocean waters – and therefore the isolation of the abyssal ocean - was actually initiated between MIS 5d and MIS 5a (114 to 71 ka BP). Evidence for early changes in abyssal circulation and reductions in deep-ocean overturning have also been detected in Indian Ocean $\delta^{13}C$ records (Govin et al., 2009). More recently, Indian Ocean εNd records (Williams et al., 2021) have suggested that the abyssal ocean may have responded to sea ice changes around the Antarctic continent early in the glacial cycle, with colder and more saline AABW forming as sea ice expanded near the continent. If indications of an early-glacial response in the global ocean circulation in the Indo-Pacific are correct, these data may also point to an elevated importance of sea ice near the Antarctic continent in triggering early, deep-ocean overturning changes.

The third possible explanation involves changes in surface ocean temperature gradients in the Southern Ocean, and how they could influence air-sea gas exchange.

Several recent studies have pointed to the importance of changes to air-sea disequilibrium, which, in this case, refers to the undersaturation of carbon in surface waters relative to atmospheric concentrations, as a key contributor to CO_2 uptake in the Southern Ocean (Eggleston & Galbraith, 2018; Marzocchi & Jansen 2019; Khatiwala et al. 2019). Khatiwala et al. (2019) suggested that modelling studies have traditionally underrepresented (or neglected) the role of air-sea disequilibrium in amplifying the impact of cooling on potential CO_2 sequestration in the mid-high southern latitudes during glacial periods. In the modern ocean, the slow air-sea gas exchange of CO_2 due to the carbon buffering chemistry (~1 year) results in the the surface waters in the Southern Ocean remaining undersaturated in CO_2 (Khatiwala et al., 2019). Thus, a weakening of the SST gradients between the polar and mid-latitude surface waters would slow surface currents and allow for a more complete equilibration of the surface waters, ultimately leading to a net drawdown of CO_2 (Khatiwala et al., 2019). They argue that when the full effects of air-sea disequilibrium are considered, this mid-latitude surface cooling can result in a 44 ppm decrease due to temperature-based solubility effects alone. They attributed this increased impact of SST to a reduction in sea-surface temperature gradients explicitly in polar mid-latitude regions (roughly between 40° and 60° north and south).

If we compare the SST gradients in the southwest Pacific sector over the last glacial-interglacial cycle (Figure 14), we see an early cooling response between MIS 5e-d corresponding to roughly half of the full glacial cooling, specifically in the cores located south of the modern STF. While not quantified, Bianchi and Gersonde (2002) also described a weakening of meridional SST gradients between the Subantarctic and Antarctic Zones during MIS 5d in the Atlantic sector. Although this analeysis is based on sparse data, our SSST reconstructions are consistent with the notion that surface ocean cooling, a weakening of meridional SST gradients, and changes to the overall air-sea disequilibrium could allow more carbon to be absorbed into the oceans and may be responsible for at least some portion of the early CO_2 drawdown. Further SST estimates from the region, and from the global ocean, are needed to substantiate this hypothesis.

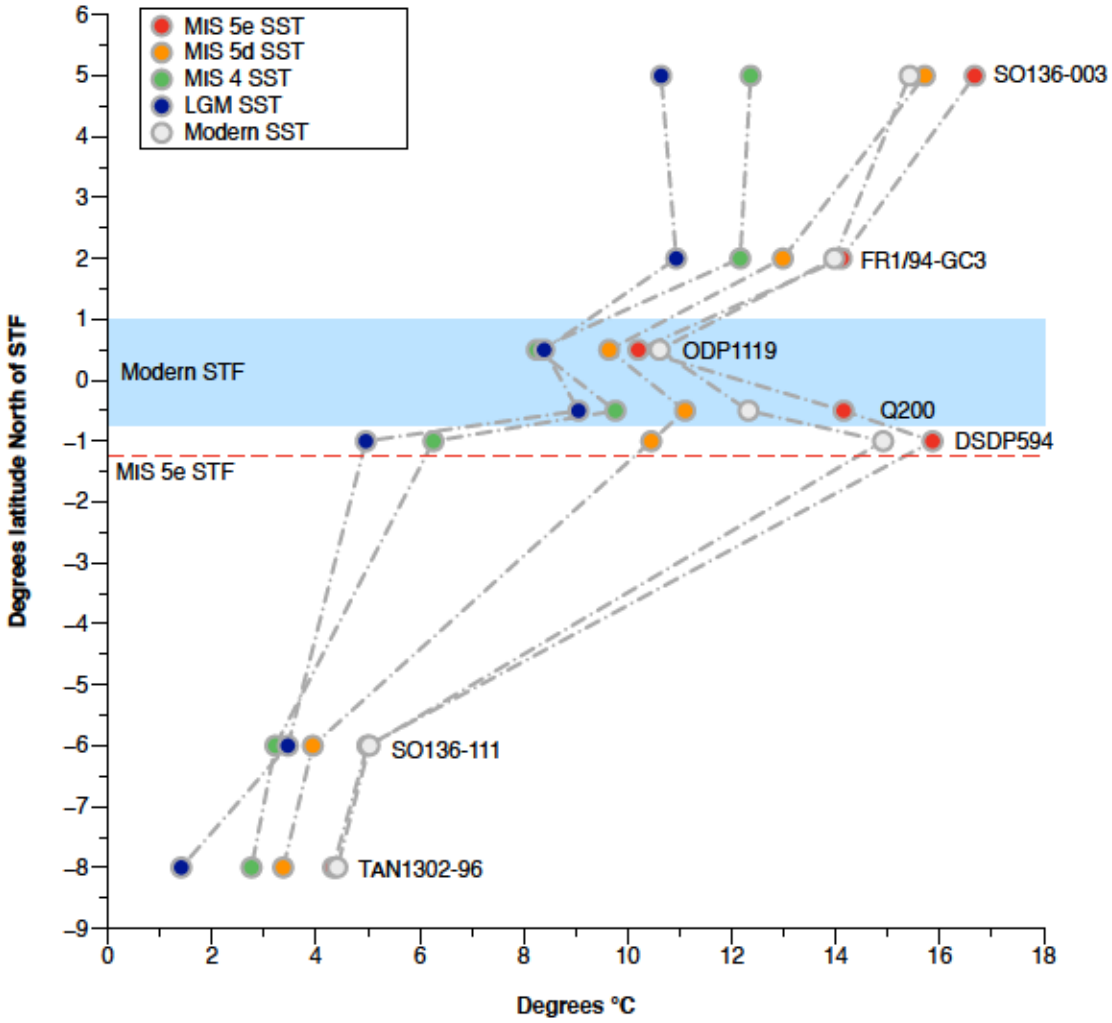

Figure 14: *SST estimates from 7 cores located in the southwestern Pacific. SST used were 5-point averages (depending on sampling resolution) taken at MIS peaks/median dates in accordance with boundaries outlined in Lisiecki & Raymo, (2005). Due to the complex circulation and frontal structures in the region, cores were plotted in +/- distance from the average position of the modern STF. Cores used include: SO136-003 (SSTs calculated from alkenones, Pelejero et al., 2006); FR1/94-GC3 (alkenones, Pelejero et al., 2006); ODP 181-1119 (PF-MAT, Hayward et al., 2008); DSDP594 (PF-MAT, Schaefer et al., 2005); Q200 (PF-MAT, Weaver et al., 1998); SO136-111 (D-MAT, Crosta et al., 2004); and TAN1302-96 (D-MAT; this study). The blue band represents the modern STF zone while the red dotted line represents the southern shift in the STF during MIS 5e (Cortese et al., 2013).*

2.4.4 Sea Ice Expansion and Ocean Circulation

Although the TAN1302-96 WSIC record suggests that sea ice was largely absent at the core site until the mid-glacial (~65 ka BP), the observed changes in sea ice could have modulated regional fluctuations in Antarctic Intermediate Water (AAIW) subduction throughout the glacial-interglacial cycle. The annual growth and decay of Antarctic sea ice

plays a critical role in regional water mass formation. Brine rejection results in net buoyancy loss in regions of sea ice formation, while subsequent melt results in freshwater inputs and net buoyancy gains near the ice margin (Shin et al., 2003; Pellichero et al., 2018). This increased freshwater input and buoyancy gain near the ice margin can hinder AAIW subduction, with direct and indirect impacts on both the upper and lower branches of the meridional overturning circulation (Pellichero et al., 2018).

Previous research has used $\delta^{13}C$ in benthic foraminifera to track changes in the depth of the interface between AAIW and Upper Circumpolar Deep Water (UCDW) (Pahnke and Zahn, 2005; Ronge et al., 2015). Low $\delta^{13}C$ values are linked to high nutrient concentrations found at depths below ~1500 m in the UCDW, and higher $\delta^{13}C$ values are associated with the shallower AAIW waters (Figure 13). Marine sediment core MD97-2120 (45.535°S, 174.9403°E, core depth 1210 m) was retrieved from a water depth near the interface between the AAIW and UCDW water masses (Pahnke & Zahn, 2005). Over the last glacial-interglacial cycle, fluctuations in the benthic $\delta^{13}C$ values from MD97-2120 suggest that the core site was intermittently bathed in AAIW and UCDW, and that the vertical extent of AAIW fluctuated throughout the last glacial-interglacial cycle. Ronge et al. (2015) used the $\delta^{13}C$ values from MD97-2120 and other core sites to quantify the contributions of AAIW to the waters overlying MD97-2120 (%AAIW, Appendix D). These results suggest that during warm periods, MD97- 2120 exhibited more positive $\delta^{13}C$ values, corresponding to higher %AAIW, while cooler periods exhibited more negative values, corresponding to lower %AAIW (Figure 13). This suggests that during cooler periods, the AAIW-UCDW interface shoaled, reducing the total volume of AAIW and indirectly causing an expansion of UCDW (Ronge et al., 2015).

Our comparison between %AAIW and regional WSIC estimates suggest a strong link between the two (Figure 13). Specifically, we observe that AAIW shoaled and UCDW expanded (i.e., %AAIW is low) during periods when sea ice expansion occurred. In contrast, during periods of low WSIC, a reduced seasonal sea ice cycle, and warmer summer sea surface temperatures (e.g., MIS 5e), %AAIW is observed to be high. This correlation supports the idea that increased concentrations of regional sea ice resulted in a substantial summer freshwater flux into the AAIW source region. This regional freshening likely promoted a shallower subduction of AAIW and a corresponding volumetric expansion of UCDW, which can be seen by the isotopic offset of the $\delta^{13}C$

values between the reference cores, and also by the increased carbonate dissolution in MD97-2120 during glacial periods (Figure 15) (Pahnke et al., 2003; Ronge et al., 2015). These findings directly link sea ice proxy records to observed changes in ocean circulation and water mass geometry.

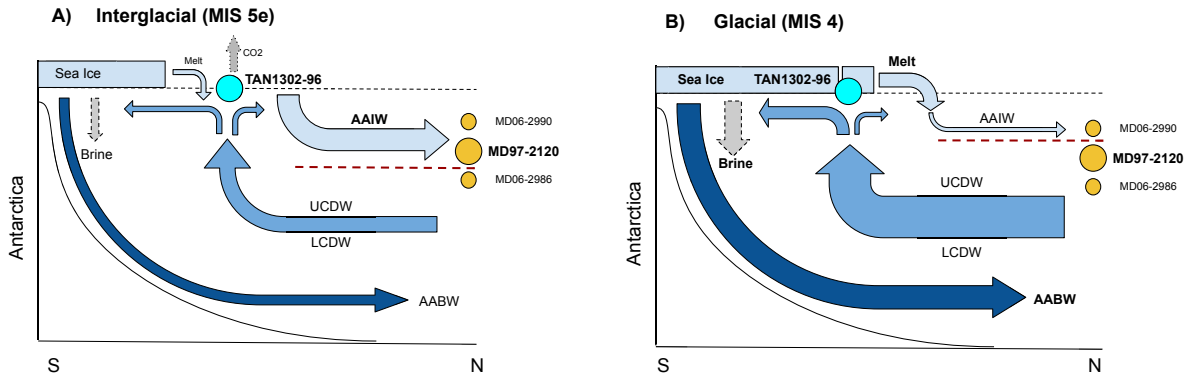

Figure 15: *Schematic of changes in southwestern Pacific sector sea ice coverage and water mass geometry between interglacial and glacial stages.* ***A)*** *Depicts interglacial conditions where sea ice coverage is minimal and freshwater input from summer sea ice melt is low. This lack of freshwater input allows AAIW to subduct to deeper depths and bath core MD97-2120, capturing the higher $\delta^{13}C$ signature of the overlying AAIW waters. The AAIW-UCDW interface (red dashed line) is located beneath MD97-2120. CO_2 outgassing is occurring as carbon-rich Circumpolar Deep Waters upwell near Antarctica.* ***B)*** *Depicts glacial conditions where sea ice expansion has occurred beyond TAN1302-96, increasing brine rejection, and stabilizing the water column. As a result of the increased sea ice growth, subsequent summer melt increases the freshwater flux into the AAIW source region and increases AAIW buoyancy. This buoyancy gain shoals the AAIW-UCDW interface above core MD97-2120, causing the core site to be bathed in low $\delta^{13}C$ UCDW. The shoaling of AAIW causes an indirect expansion of CDW, increasing the glacial carbon stocks of the deep ocean while sea ice reduces CO_2 outgassing via the capping mechanism.*

In addition to its influence on regional freshwater forcing and AAIW reductions, these sea ice changes may also coincide with larger-scale deep ocean circulation changes. The most dramatic increases in winter sea ice observed in TAN1302-96 and SO136-111, along with changes in %AAIW, are initiated during MIS 4. These shifts also correspond to basin-wide changes in benthic $\delta^{13}C$ values in the Atlantic Ocean that suggest a shoaling in the AMOC during MIS 4 (Oliver et al., 2010; Kohfeld & Chase, 2017). Changes in deep ocean circulation are also recorded in εNd isotope data in the Indian sector of the Southern Ocean (Wilson et al., 2015), suggesting extensive reductions in the AMOC during this period. Recent modelling literature (Marzocchi & Jansen, 2019; Stein et al., 2020) suggests that sea ice formation directly impacts marine carbon storage by

increasing density stratification and reducing diapycnal mixing, especially in simulations where brine rejection is enhanced near the Antarctic continental slope and open ocean vertical mixing (and subsequent CO_2 outgassing) is reduced (Bouttes et al. 2010; 2012; Menviel et al. 2012). These simulations suggest a resulting CO_2 sequestration of 20-40 ppm into the deep ocean.

Taken collectively, the available data show that sea ice expansion, AAIW-UCDW shoaling, changes in the AMOC, and a decrease in atmospheric CO_2 all occur concomitantly during MIS 4 (Figure 13). It appears likely, therefore, that sea-ice expansion during this time influenced intermediate water density gradients through increased freshening and consequent shoaling of AAIW. These changes may have led to a volumetric expansion in carbon-rich deep waters, and may also have increased the efficiency of the carbon pump and increased CO_2 uptake by phytoplankton (Sigman et al., 2021). This appears to have occurred while simultaneously influencing deep-ocean density, and therefore stratification, through brine rejection and enhanced deep-water formation, which ultimately lead to decreased ventilation (Abernathey et al., 2016). These changes in ocean stratification, combined with the sea ice 'capping' mechanism, appear to agree with both the recent modelling efforts (Stein et al., 2020) and observed proxy data, and fit well within the hypothesis that mid-glacial CO_2 variability was primarily the result of a more sluggish overturning circulation (Kohfeld & Chase, 2017).

2.5 Summary & Conclusion

This study presents new WSIC and SSST estimates from marine core TAN1302-96, located in the southwestern Pacific sector of the Southern Ocean. We find that the WSIC remained low during the early glacial cycle (MIS 5, ~130 to 70 ka BP), expanded during the middle glacial cycle (MIS 4, ~65 ka BP), and reached its maximum just prior to the LGM (MIS 2, ~24.5 ka BP). These results largely agree with nearby core SO136-111 but display some differences in WSIC magnitude with E27-23. This discrepancy may be explained by differences in statistical applications and/or lateral sediment redistribution, although more analysis is required to determine the exact cause(s).

The lack of changes in SSST and the absence of winter sea ice over the core site during the early glacial suggests that the sea ice capping mechanism and corresponding surface stratification in this region is an unlikely cause for early CO_2 drawdown, and that

alternative hypotheses should be considered when evaluating the mechanism(s) responsible for the initial drawdown. More specifically, we consider the impact of changes in SSST gradients between ~40˚ to 60˚S and support the idea that changes in air-sea disequilibrium associated with reduced sea-surface temperature gradients could be a potential mechanism that contributed to early glacial reductions in atmospheric CO_2 concentrations (Khatiwala et al., 2019). Another key consideration is the potentially non-linear response between sea ice expansion and CO_2 sequestration potential (i.e., that not all sea ice is equal in its capacity to sequester carbon). More analyses are required to adequately address this.

We also observe a strong link between regional sea ice concentrations and vertical fluctuations in the AAIW-UCDW interface. Regional sea ice expansion appears to coincide with the shoaling of AAIW, likely due to the freshwater flux from summer sea ice melt increasing buoyancy in the AAIW formation region. Furthermore, major sea ice expansion and AAIW shoaling occurs during the middle of the glacial cycle and is coincident with previously recognized shoaling in AMOC and mid-glacial atmospheric CO_2 reductions, suggesting a mechanistic link between sea ice and ocean circulation.

In conclusion, this paper has focused exclusively on sea ice as a driver of physical changes, but we recognize that these changes in sea ice will be accompanied by multiple processes that interact and compete with each other. Marzocchi & Jansen (2019) note that teasing apart the individual components of CO_2 fluctuations is complicated because of interactions between sea ice capping, air-sea disequilibrium, AABW formation rates, and the biological pump. We recognize that these processes may not act independently, and as such, have contributed new data to help advance our collective understanding of the role of sea ice on influencing atmospheric CO_2 variability on a glacial-interglacial time scale.

Chapter 3: Reconstructing Opal Burial from TAN1302-96: Insights into the Role of Sea Ice, Migrating Fronts, and the Effects of Dilution and Dissolution

3.0 Abstract

Reconstructing past opal burial in the Southern Ocean can provide useful information on the contribution of diatoms to biological productivity in the surface ocean and the degree of silica (Si) utilization, which can help shed light on surface ocean conditions during past glacial-interglacial periods. The Subantarctic and Antarctic Polar Front Zones of the Southern Ocean are areas of particular interest to studying changes in opal burial because of the proximity to intermediate water source regions which supply nutrients to the mid- and low latitudes and help sequester carbon into the deep ocean. Changes in opal burial rates can be influenced by environmental conditions, such as sea-ice coverage or iron deposition, or by water column and sedimentation processes, such as preservation, dilution, and lateral sediment redistribution. This chapter presents newly measured opal concentrations from marine core TAN1302-96 over the last 140 ka and compares them with previously calculated sea-ice estimates, $CaCO_3$, and iron (Fe) concentrations, and mass accumulation rates, to better understand the larger processes that govern opal burial in this region. The results from this analysis suggest that periods of extended sea-ice coverage and warm, interglacial periods when the Antarctic Polar Front migrated poleward both coincided with periods of reduced opal burial. In contrast, increased productivity during warm, interglacial periods may have driven higher opal burial rates than those observed during the glacial period. There are several possible ways of interpreting changes in opal burial over the last glacial-interglacial cycle within the larger context of multiple proxies, although limited interpretations can be drawn with the current dataset. The current lack of constant flux proxies (i.e., a U-Th systematics analysis) inhibits our ability to determine if the sediment was deposited vertically or if it was subject to lateral redistribution, which would alter interpretations. Currently, a U-Th systematics analysis is being conducted on TAN1302-96, although the results are pending at the time of writing.

3.1 Introduction

Reconstructing biogenic opal concentrations (i.e., biologically produced silica (Si)) and burial rates from marine sediment cores can provide useful information on past surface conditions, such as ocean circulation and frontal locations (Cortese et al., 2004; Honjo, 2004), rates of upwelling and nutrient availability (Anderson et al., 2009), and overall diatom productivity (Mortlock et al., 1991). Numerous factors contribute to diatom productivity at the sea surface, including sea ice coverage (e.g., Burckle & Mortlock, 1998; Chase et al., 2003; Chase et al., 2015), nutrient availability (e.g., Martin et al., 1990;

Sigman et al., 2002; Anderson et al., 2009), and favourable environmental conditions, such as adequate sunlight and a shallow mixed layer (Chase et al., 2015). However, additional processes throughout the water column and during sedimentation can complicate interpretations. These processes include enhanced (or decreased) preservation (e.g., Emerson & Archer, 1990; Archer et al., 1993; Howard & Prell, 1994), relative dilution by other sedimentary components, and lateral sediment redistribution (i.e., postdepositional redistribution) (Chase et al., 2003; Francois et al., 2004). Accurate interpretation of past opal burial is an important component in evaluating the past efficiency of the biological pump, which describes processes that work to remove CO_2 and inorganic nutrients from the surface waters and 'pump' them into the deep ocean via photosynthesis and subsequent gravitational settling (Anderson et al., 2002; Stukel & Ducklow, 2017). While the biological pump operates inefficiently in the Southern Ocean today (Sigman et al., 2021), this may not always have been the case. Past changes in its efficiency have been proposed to be able to account for a significant proportion of the total glacial-interglacial CO_2 variability, with 'best' estimates around 15 to 20 ppm (Röthlisberger et al., 2004; Kohfeld & Ridgwell, 2009).

Changes in opal burial are particularly relevant to the silicic acid leakage hypothesis (SALH), initially proposed by Brzezinski et al. (2002) and Matsumoto et al. (2002). This hypothesis suggests that during glacial periods, excess silicic acid ($Si(OH)_4$) from the Southern Ocean was exported via intermediate waters and supplied mid-latitude regions with sufficient silicic acid to allow diatoms to outcompete $CaCO_3$-bearing phytoplankton, ultimately leading to net CO_2 drawdown. Proposed mechanism(s) that could have caused the increased supply of silicic acid to escape the Southern Ocean include [1] an increase in iron (Fe) supply, which decreased the Si:N uptake ratio of diatoms in the Southern Ocean (SO) (Takeda, 1998), or [2] an increase in sea ice coverage, which decreased the Si uptake in the region covered by sea ice (Chase et al., 2003; Matsumoto et al., 2014). The leakage of silicic acid from the Antarctic region is proposed to have caused a "dipole" in diatom productivity on either side of the winter sea ice edge (approximately the modern Antarctic Polar Front (APF) during the Last Glacial Maximum (LGM), ~21 ka), with lower rates of productivity occurring to the south and higher productivity to the north (Charles et al., 1991; Mortlock et al., 1991; Chase et al., 2003; Bradtmiller et al., 2009: Benz et al., 2016). Large-scale reconstructions of opal export support the presence of the proposed dipole in the Southern Ocean during the last glacial

period (e.g., Kohfeld et al., 2005; Bradtmiller et al., 2009; Kohfeld et al., 2013), although reconstructions from the eastern equatorial Pacific have shown that the silicic acid enhancement caused by the leakage was likely not occurring on the scale proposed by Brzezinski et al. (2002) and Matsumoto et al. (2002) (Dubois et al., 2010).

The Subantarctic Zone and Antarctic Polar Front Zones of the southwestern Pacific are important to the formation of Antarctic Intermediate Waters (AAIW), which contribute biologically important nutrients and carbon to the interior waters of the Pacific Ocean (Panassa et al., 2018). Glacial-interglacial changes in sea ice, frontal systems, nutrients, and Fe inputs could influence how the waters of this region are preconditioned, thereby influencing downstream processes where these intermediate waters upwell, such as mid- and low-latitude primary production and carbon sequestration (e.g., Pahnke & Zahn, 2005; Ronge et al., 2015). Past work has shown that this part of the world is affected by both sea-ice expansion (e.g., Crosta et al., 2004; Ferry et al., 2015; Benz et al., 2016; Jones et al., 2022) and changes in Fe deposition during glacial-interglacial cycles (e.g., Wu et al., 2021; Durand et al. 2017); although most dust-related work is focused either in the central and southeast Pacific (Lamy et al., 2015) or north in the Sub-Antarctic Zone (SAZ) and Subtropical Front Zones (STF). Previous studies have provided examinations of changes in sea ice (e.g., Benz et al., 2016) and opal burial (Chase et al., 2003; Bradtmiller et al., 2009) during the LGM and Holocene time periods, but few have examined the temporal relationships between opal concentration, iron, and sea ice to better understand the interplay between these factors through time.

Within this chapter, I compare winter sea-ice estimates provided in Chapter 2 with newly measured opal concentrations from marine sediment core TAN1302-96 and previously collected calcium carbonate ($CaCO_3$) and iron (Fe) concentrations. I explore the influences that sea-ice expansion and iron deposition may have had on opal burial and consider the additional effects that changes in productivity, preservation, and dilution may have had on opal concentration. Opal is of particular importance in this region, as the degree of Si utilization in the Southern Ocean has been hypothesized to have modulated atmospheric CO_2 in the past (Chase et al., 2015).

The analysis presented in this chapter represent the first step in a larger research study designed to understand the interactions between sea ice, iron deposition, and changes in marine productivity. Analyses are planned to provide a better understanding

of changes in surface ocean productivity using $^{231}Pa/^{230}Th$ (Anderson et al., 1983; Kumar et al., 1993) and deep ocean preservation using authigenic Uranium concentrations (e.g., Chase et al., 2003). Furthermore, the addition of ^{230}Th measurements (known as a "constant flux proxy") (Francois et al., 2004) will be used to a to account for uncertainties associated with the impact of lateral sediment redistribution on biogenic accumulation rates. This 'U-Th systematics' analysis for TAN1302-96 is currently underway by colleagues at the University of Tasmania, and the results are still pending at the time of writing. As such, the goal of this chapter is to provide a preliminary framework that identifies potential drivers of changes in opal burial in this region of the ocean during the last glacial cycle.

3.2 Methods

3.2.1 Study Site & Study Area

This chapter uses data collected from marine core TAN1302-96 (59.09°S, 157.05°E, water depth 3099 m), introduced in Chapter 2. The core is from the southwestern Pacific sector of the Southern Ocean (SO) (Figure 16), approximately 3° south of the average position of the APF at 157°E (Sokolov & Rintoul, 2009). The age model for TAN1302-96, outlined in Chapter 2, is based on radiocarbon ages and $\delta^{18}O$ stratigraphy tied to the LR04 benthic stack (Lisiecki & Raymo, 2005), and extends to at least 140 ka, capturing a full glacial-interglacial cycle (Jones et al., 2022).

The southwestern Pacific sector of the SO, corresponding to roughly between 90°W and 90°E, and ~40°S to the Antarctic coastline, contains a complex series of fronts along steep temperature and nutrient gradients (Sokolov & Rintoul, 2002; Sokolov & Rintoul, 2009). The region has complex bathymetry which constrains frontal flow east of New Zealand in and around the Campbell Plateau and Chatham Rise (Bostock et al., 2013). The APF divides warmer, nutrient-poor waters in the north from cooler, nutrient-rich waters in the south. The waters south of the APF contain high silicic acid and nitrate concentrations due to upwelled Circumpolar Deep Water (CDW) (Anderson et al., 2009; Bostock et al., 2013), and these high silicic acid concentrations are necessary to sustain diatom populations and provide silica for frustule formation (Hildebrand et al., 2018). Despite the high nutrient concentrations south of the APF, the region is considered a high-nutrient, low chlorophyll (HNCL) area, as low primary production is the result of iron and

light limitation (De Baar et al., 1990; Mitchell et al., 1991; Chase et al., 2003). Sedimentation north of the APF is dominated by calcium carbonate, largely due to the deposition of coccoliths and foraminifera resulting from low silicic acid availability, while south of the APF is silica-dominant due to the deposition of diatoms (and lack of coccoliths) (Honjo, 2004).

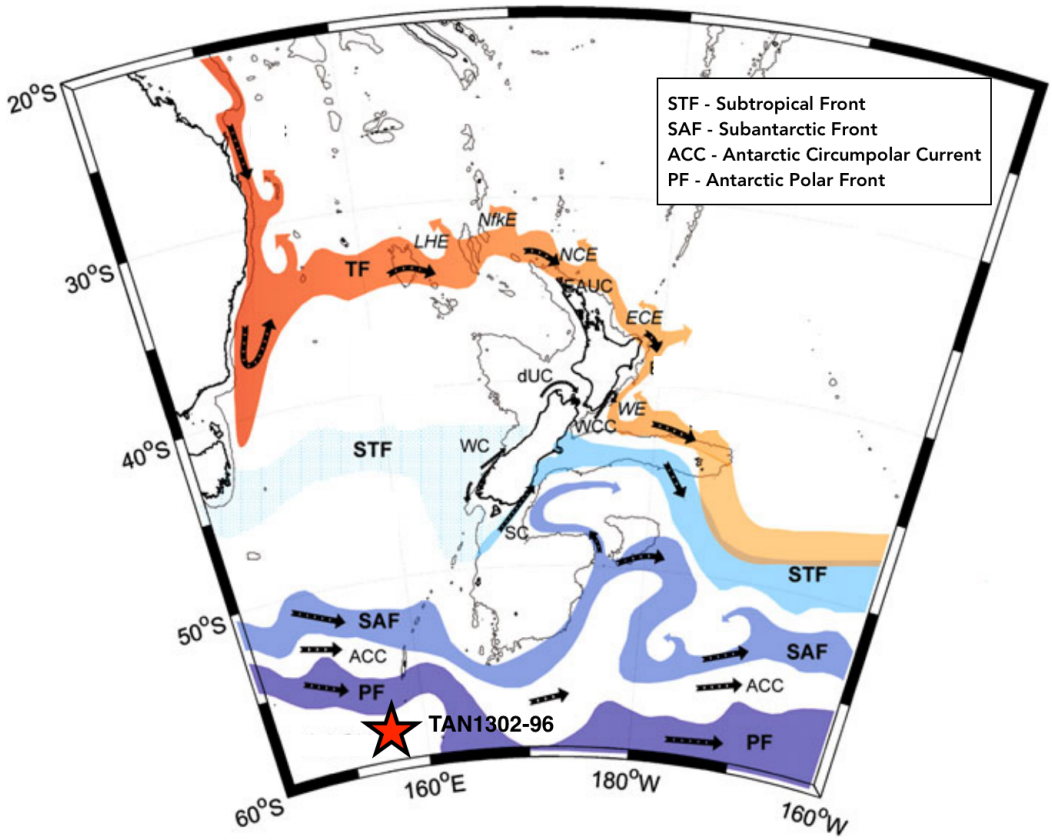

***Figure 16**: Map of the Australian/New Zealand sub-sector of the southwestern Pacific sector of the SO. Location of TAN1302-96 is indicated by the red circle. Location of the average positions of the fronts across the SO (Chriswell et al., 2015).*

3.2.2 Previously Collected Data

This chapter uses previously collected dry bulk density (ρ) and X-ray fluorescence (XRF) data, including Fe and $CaCO_3$ concentrations from TAN1302-96 (Liston 2018). As outlined in Chapter 2, winter sea ice presence (WSIP), expressed in months/year, was calculated using the modern analog technique (MAT) (see Appendix G). WSIP is a similar

metric as winter sea ice concentration (WSIC) but expresses coverage in terms of a semi-monthly presence/absence of sea ice instead of a grid-scale observation of the mean state fraction of area covered by ice over the sample period (Crosta et al., 1998; Crosta et al., 2004). WSIP is used in this chapter instead of WSIC (as was used in Chapter 2) because the prominent literature (e.g., Chase et al., 2015) relating opal to sea ice expresses sea ice coverage in terms of presence/absence (WSIP) rather than concentration. Both metrics (WSIC and WSIP) describe a similar quantitative estimate of sea ice coverage over the core site.

3.2.3 Opal Analysis

Biogenic opal concentrations reflect the amount of opal buried relative to other sediment constituents (Chase et al., 2015). Opal concentrations are a new contribution of this thesis and were measured using a rapid wet-alkaline extraction procedure (Mortlock and Froelich, 1989). Samples were freeze-dried overnight, crushed, and weighed into 50-ml polypropylene centrifuge tubes. Five ml of 10% H_2O_2 solution was added for 30 minutes and followed by an addition of 5 ml of a ~1 NHCl solution. Samples were then sonified and let rest for 30 minutes, followed by the addition of 20 ml of deionized water, and then centrifuged for 5 minutes. Afterwards, the supernatant was decanted, and the samples were placed overnight in an oven to dry (60°C). Then, 40 ml of Na_2CO_3 solution was added to the samples which were then vortexed, sonified, and placed in an 85°C water bath for 5 hours. Samples were then manually shaken after 2 and 4 hours in the water bath. Samples were centrifuged for 5 minutes and transferred into cuvettes, where measurements were made using a molybdate-blue spectrometer.

3.2.4 Mass Accumulation Rates

Mass accumulation rate (MAR, g cm^{-2} ka^{-1}) refers to the rate of sediment accumulation (in grams) over a particular area (cm^2) through time. For each sediment depth, MAR was calculated using the following equation:

$$MAR_{Total} = LSR \times \rho$$

where LSR is the linear sedimentation rate (cm ka^{-1}) determined in Chapter 2, and ρ is the dry bulk density (g cm^{-3}).

The MARs of each sediment component (i.e., opal, Fe, and $CaCO_3$) were calculated using the sediment fraction of each component relative to the total MAR. For example, Opal MARs were calculated for each depth interval using the following equation:

$$MAR_{Opal} = f_{opal} * MAR$$

where f_{opal} is fraction of sediment composed of opal, estimated as the % concentration divided by 100. $CaCO_3$ and Fe MARs were estimated for each depth interval in the same manner, using the fraction of sediment composed of $CaCO_3$ and Fe (after converting ppm to %).

3.3 Results

3.3.1 Opal, $CaCO_3$, and Fe Concentrations

Opal concentrations were relatively high (66%) during the Penultimate Glaciation (MIS 6) and underwent a rapid decrease during Termination II, reaching their lowest value of 33% at 125 ka (Figure 17). Following minimum values during MIS 5e, concentrations increased steadily, reaching 61% by 118 ka and 70% during mid-MIS 4 (65 ka). Opal concentrations then decreased to 52% at the MIS ¾ boundary (57 ka) before reaching their highest value of 77% at 44 ka, which was followed by a steady decline into MIS 2. Concentrations declined to 56% by 18 ka before increasing to 71% at 16 ka. Opal concentrations then decreased and remained between 55% and 64% throughout the Holocene (~12 ka BP onwards).

In contrast, $CaCO_3$ concentrations were low (between 2% and 9%) during MIS 6 and rapidly increased to reach peak concentrations (47%) at 125 ka during MIS 5e (Figure 17). Concentrations rapidly declined to 17% by 123 ka BP before slightly increasing to 24% at 116 ka BP before a steady decline until reaching a low of 3% during MIS 4 (65 ka). Concentrations briefly rose to 20% at the MIS 3/4 boundary (55 ka), before declining and remaining near ~5 % during the rest of MIS 3 and 2. During the early Holocene (~10 ka), $CaCO_3$ concentrations began rising and continued to until reaching values of 22% in the shallowest part of the core.

Fe concentrations follow a glacial-interglacial pattern in that they are relatively high during the cold glacial periods of MIS 2, 4, and 6, and low during warm, interstadial periods of MIS 1, 3, and 5 (Figure 17).

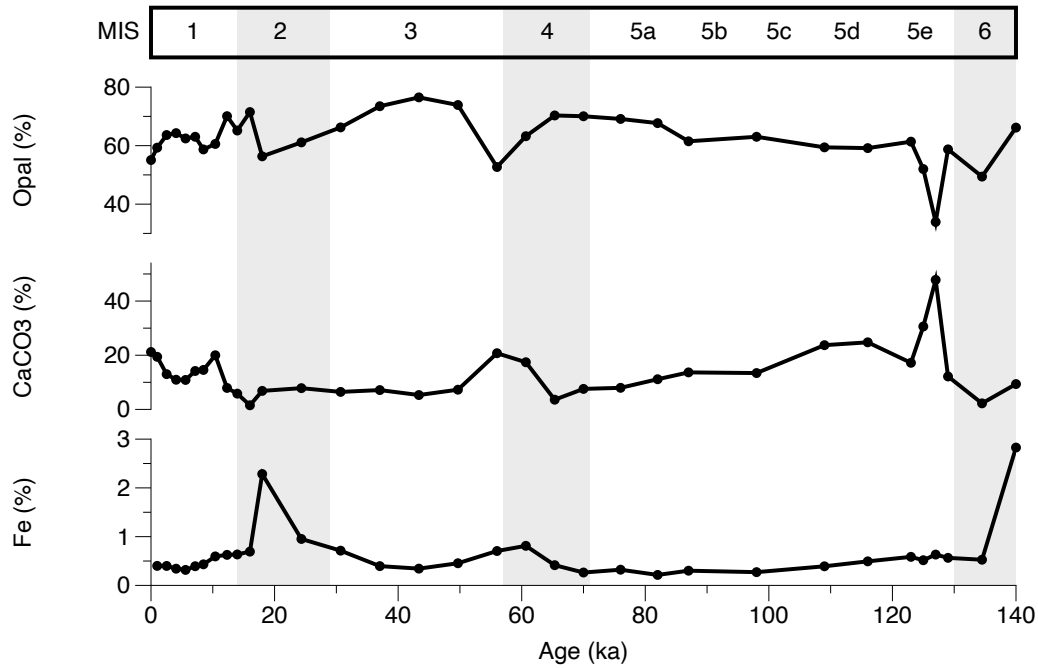

***Figure 17**: Opal, $CaCO_3$, and Fe concentrations from TAN1302-96 over a full glacial-interglacial cycle.*

3.3.2 Mass Accumulation Rates

MAR_{opal} is relatively low at ~0.3 g cm^{-2} ka^{-1} throughout most of the record, with an increase at MIS 5e (127 ka BP) to ~1 g cm^{-2} ka^{-1} and a smaller increase during MIS 4 (61 ka BP) to 0.5 g cm^{-2} ka^{-1}. MAR_{opal} increases substantially following MIS2 through the Holocene, from ~0.3 g cm^{-2} ka^{-} in MIS 2 to 2 g cm^{-2} ka^{-1} the top of the core (Figure 18).

MAR_{CaCO3} ranges from ~0.01 to 0.06 g cm^{-2} ka^{-1} throughout most of the record, with substantial increases to 0.86 g cm^{-2} ka^{-1} during MIS 5e (127 ka BP) and ~0.14 g cm^{-2} ka^{-1} during MIS 4 (61 ka BP). MAR_{CaCO3} increases towards the end of MIS 2 (14 ka BP) from ~0.1 g cm^{-2} ka^{-1} to a maximum of ~0.6 g cm^{-2} ka^{-1} at top of the core.

MAR_{Fe} shows low accumulation of ~0.003 g cm^{-2} ka^{-1} throughout most of the record, with increased accumulation rates during glacial periods of ~0.03 g cm^{-2} ka^{-1} during MIS 6 (127 ka BP), ~0.01 g cm^{-2} ka^{-1} during MIS 4 (61 ka BP), and ~0.4 cm^{-2} ka^{-1} during MIS 2 (18 ka BP). MAR_{Fe} remained low during the Holocene.

MAR_{Total} shows a similar pattern as MAR_{opal} and MAR_{CaCO3} with relatively low accumulation during MIS 6 (between 0.4 and 0.7 g cm^{-2} ka^{-1}) before abruptly increasing to an MIS 5e peak of 1.8 g cm^{-2} ka^{-1} at 127 ka BP. MAR_{Total} remained relatively low, with a slightly increase during MIS 4 (61 ka BP) to 0.8 g cm^{-2} ka^{-1} and a larger increase beginning at 18 ka BP to a maximum of 3.3 g cm^{-2} ka^{-1} at the core top.

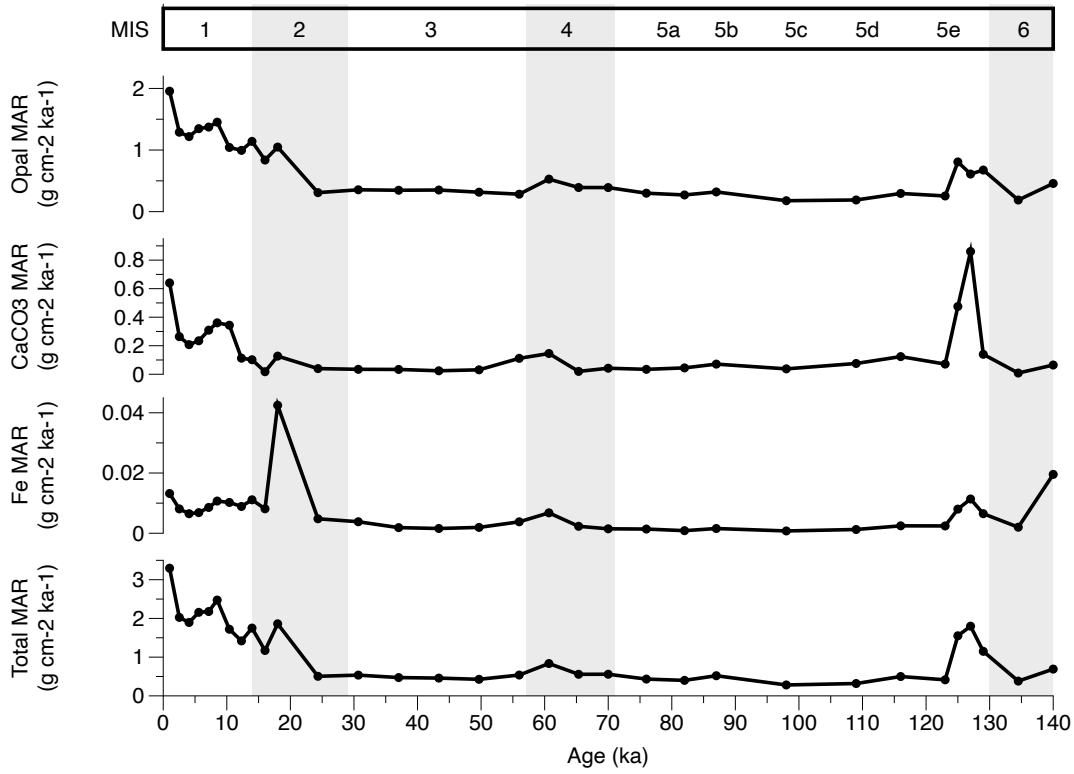

Figure 18: *Mass accumulation rates (MAR) for opal, $CaCO_3$, Fe, and total.*

3.3.3 Opal, $CaCO_3$, and Fe Concentrations vs. Accumulation Rates

While $CaCO_3$ and Fe show very similar patterns between concentrations and MARs, opal concentration and MAR_{opal} have a quite different relationship (Figure 19). During MIS 6, opal concentration appears to be relatively high (66%) while MAR_{opal} are low (0.3 g cm^{-2} ka^{-1}). A similar relationship occurs during MIS 5e, 4, and 2, where opal concentrations declined while MAR_{opal} increased, albeit only slightly. This relationship holds true during MIS 2 and the transition into Termination I, where opal concentrations and MAR_{opal} change in opposing directions.

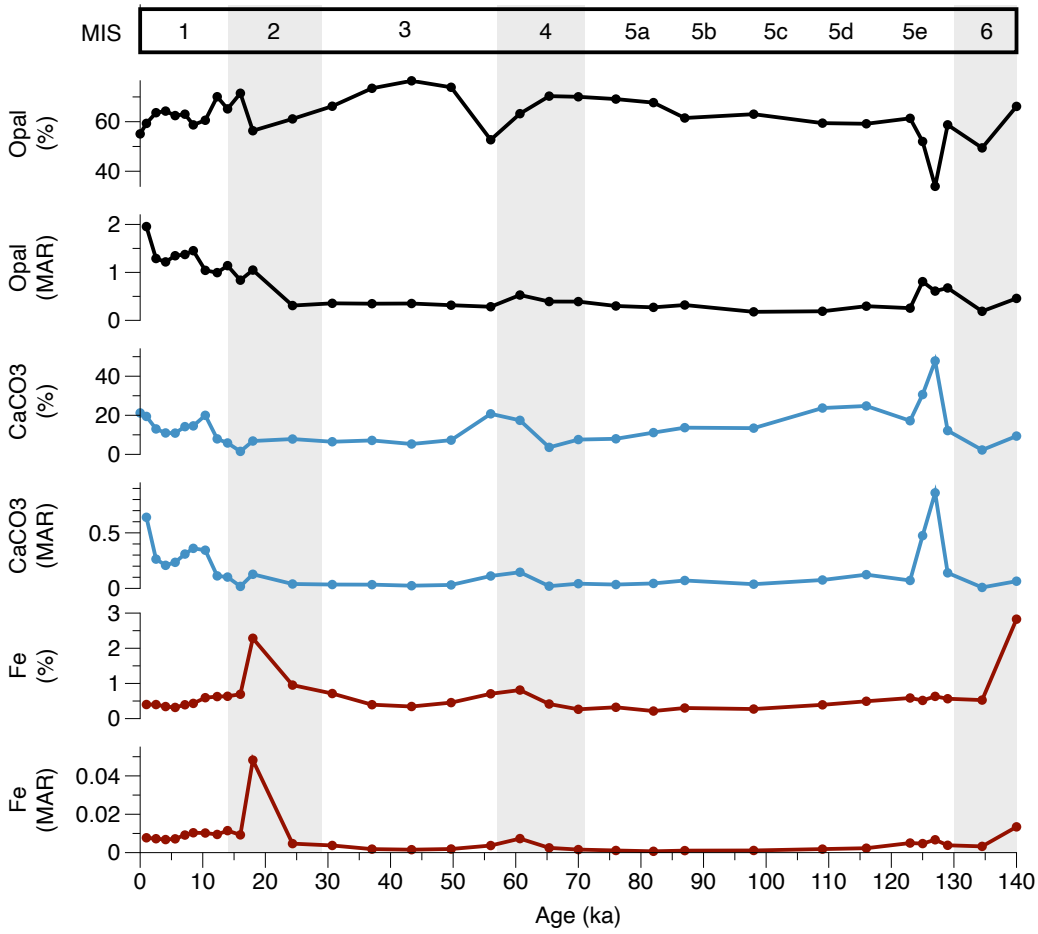

***Figure 19**: Comparison of concentrations and MARs for opal (black), $CaCO_3$ (blue), and Fe (dark red).*

3.4 Discussion

The results from TAN1302-96 suggest that opal concentrations have remained relatively high over the last glacial-interglacial cycle with some notable periods with lower concentrations, including MIS 5e and the Holocene. In the following sections, I highlight four possible mechanisms that could be driving reductions in opal concentrations throughout TAN1302-96, including: [1] the effects of sea ice; [2] changes in productivity; [3] changes in preservation; and [4] the effects of dilution.

3.4.1 Opal Concentration and Sea Ice

Opal concentrations have their lowest values during both cool, stadial periods (MIS 2 and the 3/4 boundary) and warm interstadials (MIS 5e and the Holocene), while WSIC maxima are found only during stadials (MIS 2, 4, and 6) (Figure 20). This dichotomy suggests that sea-ice expansion may not be the only factor governing opal concentrations at the core site. Sea ice expansion could explain the reductions in opal concentrations observed during stadial periods of MIS 2 and 4, but likely not MIS 6 (discussed later).

Chase et al. (2003) previously noted that while the length of the ice-free season places an upper limit on opal burial rates, reductions in opal burial cannot be taken as evidence of sea ice expansion alone. Chase et al. (2015) further noted that even minor increases in winter sea ice coverage corresponding to only 1-2 months per year can result in significant reductions in opal burial rates. In our records, periods when winter sea ice presence (WSIP) exceeds 2 months/year occur during MIS 2, 4, and 6 (Figure 20). Opal concentrations decrease during MIS 2 and 4 at roughly the same time as WSIP increases to >2 months/year. These reductions are followed by opal concentration increases as the sea-ice edge retreated, suggesting a possible link. Benz et al. (2016) similarly identified the average position of the winter sea ice edge (where WSIC ≥40%) as having reduced opal burial due to the presence of winter sea ice. These contemporaneous changes suggest that sea ice expansion may have contributed to reduced opal concentrations during MIS 2 and 4. However, unlike during MIS 2 and 4, opal concentrations remain relatively high (~66%) during MIS 6, even though WSIP is >2 months/year. This suggests that expanded WSIP is not always the dominant factor governing reduced opal concentrations, and therefore we must consider additional mechanisms.

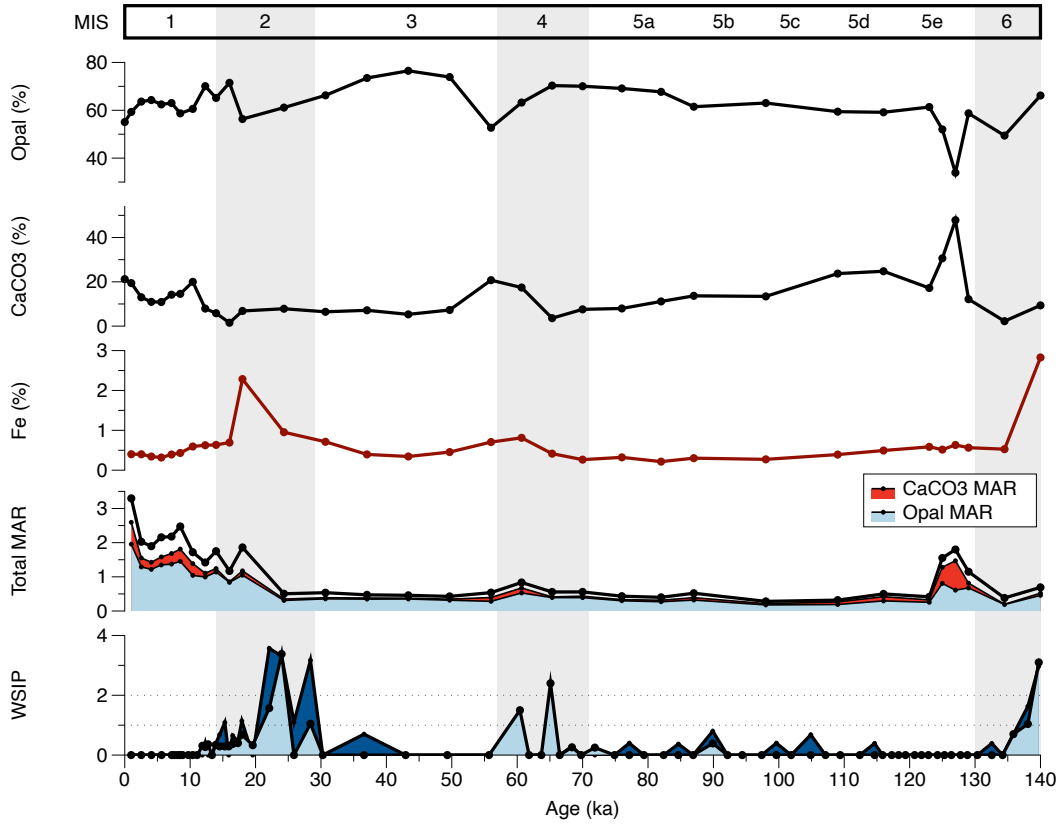

***Figure 20**: Comparison of opal, $CaCO_3$, and Fe concentrations with MAR_{Total} and calculated WSIP (expressed as coverage in months per year).*

3.4.2 Other Controls on Opal Concentration

While sea ice presence is a possible explanation for reduced opal concentrations during MIS 2 and 4, additional factors appear to control opal burial during other critical periods of the last glacial-interglacial cycle. Here I explore three additional explanations, specifically that changes in opal burial may be caused by changes in: [1] productivity; [2] preservation; and/or [3] sedimentary composition (i.e., dilution). Importantly, changes in opal burial can be controlled by multiple factors operating simultaneously, such as increases in productivity or a reduction in preservation leading to dilution by additional (or fewer) inputs.

3.4.2.1 Productivity

Changes in overall diatom productivity have a direct impact on sedimentary opal concentrations (e.g., Mortlock et al., 1991; Bradtmiller et al., 2006). A comparison of opal and $CaCO_3$ concentrations and MARs suggests that changes in productivity are a likely candidate to explain the changes during the Holocene and perhaps during MIS 5e. While opal and $CaCO_3$ concentrations are inversely correlated, the MARs of opal and $CaCO_3$ both increase substantially during these periods (Figure 20). This increase in MARs for both opal and $CaCO_3$ could suggest a real increase in burial rates in response to favourable environmental conditions. Increases in primary productivity during the Holocene has been suggested by other studies across the Southern Ocean, which show that glacial opal fluxes were generally lower south of the modern-day APF relative to the Holocene (e.g., Bradtmiller et al., 2009; Chase et al., 2015). Thus, increases in Holocene opal concentration and MAR may similarly be linked to overall increases in productivity. A similar pattern is observed during the brief interglacial period of MIS 5e, which could have been caused by favourable environmental conditions and enhanced productivity, although fewer studies have evaluated primary productivity in this region during MIS 5e compared to the Holocene.

Shifts in the position of the Antarctic Polar Front could also modulate the supply of silicic acid via upwelling, and therefore also explain some of the fluctuations in opal burial through time. During periods of glacial cooling, lowered SSTs and increased sea-ice coverage have been associated with equatorward shifts in the position of the APF, an idea supported by proxy reconstructions in other basins of the Southern Ocean (e.g., Crosta et al., 2004; Gersonde et al., 2005; Nair et al., 2019). Conversely, during periods of warming associated with glacial terminations and interglacial periods, increases in SST and decreased sea-ice coverage have been associated with poleward migrations of the APF (e.g., Howard & Prell, 1992; Weaver et al., 1998; Anderson et al., 2009; Kohfeld et al., 2013). The APF in the Atlantic sector has been reconstructed to have fluctuated south by as much as 3-5° latitude (relative to modern) during MIS 5e (Bianchi & Gersonde, 2002). Considering that the APF is a biogeochemical gradient that separate waters rich in silicic acid in the south from waters poor in silicic acid to the north (Pollard et al., 2002; Freeman et al., 2018), a poleward shift of the APF could have caused TAN1302-96 to be located north of the APF and underlying the carbonate-dominant waters of the Subantarctic Zone (SAZ). Based on the regional bathymetry, the APF was likely tightly constrained in its

equatorward migration during glacial periods near Campbell Plateau (Weaver et al., 1998; Hayward et al., 2008). However, given the proximity of TAN1302-96 to the modern-day APF, a poleward shift or increased variability in the APF by only a few degrees could have been sufficient to create a regime shift from a silica-based to a $CaCO_3$-based planktonic assemblage, thus producing the observed decrease in opal concentrations and concomitant increases in $CaCO_3$ concentrations during the warm interglacial period of MIS 5e. Although decreases in opal concentrations are observed during this time, the slight increase in opal MAR may have been the result of enhanced total primary production in the region, as observed during the Holocene interglacial period. During the deglacial warming between the LGM and early Holocene, the poleward migration of the APF could have been associated with a similar poleward shift in opal productivity and the zone of vigorous upwelling. This poleward shift may have reduced the supply of silica to the surface waters and therefore limited diatom productivity over the core site (Anderson et al., 2009).

3.4.2.2 Preservation

Changes in preservation could also influence biogenic opal and $CaCO_3$ concentrations. Numerous factors contribute to biogenic opal preservation and dissolution, including species composition (Warnock & Scherer, 2015b), temperature (Van Cappellen & Qiu, 1997; Varkouhi & Wells, 2020), porewater pH (Hurd, 1973), and sedimentation rates (Sayles et al., 2001), although debate continues whether dissolution occurs primarily in the water column or at the sediment-water interface (Warnock et al., 2007). Similarly, additional factors contributing to $CaCO_3$ preservation include changes in sedimentation rates (Emerson & Archer, 1990) as well as changes in ocean circulation and corresponding shifts in the carbonate compensation depth (Howard & Prell, 1994).

In Chapter 2 (and discussed in Appendix C), a simple comparison of relative preservation of diatom frustules throughout the core suggested no change in general diatom preservation throughout the sediment core. In other words, diatom preservation did not appear to be dependent on sedimentation rate or climatic period. If preservation were driving changes in opal concentrations, we would expect to see a decrease in the average preservation of samples during MIS 5e, the 3/4 boundary, and during the LGM, which we do not (full dataset provided in Appendix E). Additional analyses to assess the relative preservation could include an analysis of $^{231}Pa/^{230}Th$, which could provide proxies

for opal flux independent of dissolution (Kumar et al., 1993) and authigenic U which would reflect a combination of export production and deep-water oxygen content (Francois et al., 2004; Costa et al., 2020).

Alternatively, changes in the preservation of carbonate could also influence opal concentrations by influencing the relative contributions of carbonate relative to opal content. Sturm (2004) suggested that the carbonate minima observed in nearby marine core SO136-111 (Figure 9) during MIS 6 and 8 may have been the result of dissolution via a shoaling of the lysocline, although this interpretation is at odds with other cores from the region (Hodell et al., 2001; Sturm, 2004). Irrespective of the depth of the lysocline, the $CaCO_3$ concentration during MIS 6 at the TAN1302-96 core site reaches some of the lowest values (2%) at the same time as SO136-111 experiences its carbonate minima. This suggests that the dissolution that occurred at SO136-111 during MIS 6 may have been a regional phenomenon that also influenced carbonate preservation at the TAN1302-96 core site. A broader synthesis of $CaCO_3$ concentrations from nearby cores in the southwest Pacific Ocean could provide supporting information on localized carbonate dissolution and provide clarity surrounding the causes of low $CaCO_3$ during MIS 6 in SO136-111 and TAN1302-96.

3.4.2.3 Dilution

A final explanation for changes in opal concentrations is via dilution by other sedimentary components. Because opal and $CaCO_3$ comprise a significant proportion of the total sedimentary constituents (between 51% to 83%), the relative abundances of either opal or $CaCO_3$ may appear higher or lower because of relative changes in the input of each. Apparent dilution could be the result of real changes in productivity or preservation, and as such, attributing observed changes to dilution alone may be an oversimplification. A simple comparison of opal and $CaCO_3$ concentrations with changes in MAR_{opal}, $MAR_{CaCO3,}$ and MAR_{Total} can help to better understand where dilution is likely to be occurring within this sediment core (Figure 20).

The inverse relationship observed between opal and $CaCO_3$ concentrations initially suggests a dilution effect of opal by $CaCO_3$; however, the same pattern does not exist for MARs. Instead, MAR_{opal} and MAR_{CaCO3} tend to co-vary throughout the core, both dramatically increasing during MIS 2 and continuing throughout the Holocene, supporting

the earlier attribution to increased total productivity. Despite the increases in MAR_{opal} and MAR_{CaCO3} during in the Holocene, some effects of dilution are indicated by the difference between MAR_{Total}, MAR_{opal}, and MAR_{CaCO3} (Figure 20). While the changes in opal concentration may primarily be driven by changes in productivity, dilution is nonetheless influencing the concentrations in some capacity. However, the peak in opal concentration during MIS 3 may have been driven by dilution, or more specifically, the lack thereof (i.e., decreases in other sedimentary components). MAR_{opal} and MAR_{CaCO3} have some of their lowest levels during this period, and MAR_{Total} has only slightly higher rates than those seen in MAR_{opal}. The same may be true for MIS 5a-d, where declining $CaCO_3$ concentrations and little additional accumulation may be contributing to the increasing opal concentration.

The explanation of the relatively high concentration of opal during MIS 6 at 140 ka BP (66%) remains somewhat elusive. One would expect to see lower opal concentrations in response to the more extensive sea-ice cover (WSIP >2), which would likely have limited productivity (Chase et al. 2003; 2015); however, this does not appear to be the case. The high concentration of opal at 140 ka BP may be in part the result of a lack of dilution, as evidenced from the little MAR_{CaCO3} contributions at this time. This may also be supported by carbonate minima in nearby marine core SO136-111 during MIS 6, which was suggested by Sturm (2004) to have indicated a shoaling of a lysocline, although this conclusion is contested (Hodell et al., 2001; Strum, 2004; Liston, 2018). Based on the available data, dilution (driven by dissolution) may be the most likely cause of the relatively high opal concentrations during MIS 6.

3.4.3 Fe Concentrations

Australia and New Zealand have been identified as important sources of atmospheric dust to the ocean surface downstream, both in the present (e.g., Li et al., 2008; Neff and Bertler, 2015) and in the past (Lamy et al., 2015; Durand et al., 2017; Wu et al., 2021). Dust reconstructions from the region suggest that enhanced aeolian Fe input was highest during glacial periods, corresponding to periods of increased westerly wind strength and global aridity (e.g., Kohfeld and Harrison, 2001; Kohfeld et al., 2013). Fe concentrations and MAR_{Fe} from TAN1302-96 show signs of enhanced deposition during glacial periods, especially during MIS 2 and 6, in line with these reconstructions (e.g., Lambert et al., 2015). Based on the importance of Fe as a necessary nutrient for diatom productivity, we would expect to see an increase in opal concentrations during periods of

enhanced Fe input (e.g., Martin et al., 1990; Martínez-García et al., 2014). However, Fe and opal concentrations in TAN1302-96 lack any coherent relationship. For example, during MIS 6, both opal and Fe concentrations were relatively high. In contrast, during the LGM, Fe deposition (both concentrations and MAR) reached peak values while opal concentrations were at their lowest values. A similar inverse relationship existed during MIS 4, when Fe concentrations began increasing at 70 ka BP just as opal concentrations began to decrease. Here, two possible explanations are offered: [1] enhanced Fe input results in diatoms shifting to a lower Si:N uptake ratio, and [2] sea ice limits diatom productivity while acting as a substrate which collects and deposits dust-born Fe during melt.

The apparent inverse relationship between opal concentrations and Fe over the last glacial cycle could reflect reductions in biogenic opal production as diatoms shift to a lower Si:N uptake ratio when Fe inputs increase (Matsumoto et al, 2002; Bradtmiller et al., 2009; Chase et al., 2015). As suggested by the SALH, enhanced Fe supply could have caused diatoms to reduce their uptake of Si relative to N (i.e., lower their Si:N uptake ratio). This Fe-induced shift towards weakly silicified species assemblages (Boyle 1998; Marchetti & Cassar, 2007) could increase the susceptibility of diatom frustules to dissolution and perhaps drive the apparent reduction in opal concentrations during MIS 2 and 4. This hypothesis could be tested by: [1] examining diatom assemblages throughout the core for any shifts from heavily silicified towards lightly silicified species; [2] quantifying the relative preservation of diatoms throughout the core; or [3] the addition of dissolution-resistant proxies, such as the ratio of $^{231}Pa/^{230}Th$ (Kumar et al., 1993). Assessing changes in the diatom assemblages from heavily to weakly silicified species is beyond the scope of this thesis; however, a comparison of relative preservation over the glacial-interglacial cycle was previously conducted in Chapter 2. No significant changes were observed throughout the core (see Appendix E), suggesting that a shift in the diatom assemblage from heavily to weakly silicified species due to a shift to lower Si:N uptake ratio may be unlikely. One additional analysis that could help resolve this uncertainty is the inclusion of a $^{231}Pa/^{230}Th$ ratio analysis, which could be used to confirm changes in surface opal productivity and therefore providing a means of assessing whether reductions in opal concentrations were due to reduced productivity or opal dissolution. If elevated $^{231}Pa/^{230}Th$ exist during MIS 2 and 4, this could suggest that Fe-induced changes to the Si:N uptake ratio may have caused enhanced dissolution, potentially supporting this hypothesis.

Secondly, sea ice may act as a substrate which collects dust-born Fe during periods of growth and releases it to the surface water during periods of melt (Sedwick & DiTullio, 1997; Wang et al., 2014). This phenomenon has been documented within the Antarctic, with phytoplankton blooms commonly being associated with the marginal ice zone, especially during melt (e.g., Smith & Nelson, 1985). While this process may be occurring, the competing effects of sea-ice coverage limiting diatom productivity with enhanced Fe deposition promoting growth may be difficult to decouple. A simple comparison of WSIP and Fe concentration shows that Fe is high during MIS 6 and 4 when WSIP is >1; however, during MIS 2, Fe concentrations increase dramatically only after sea ice disappears from the region, suggesting this process may not explain the entire relationship between opal and Fe. Alternatively, the enhanced deposition during MIS 2 could simply be the result of the dust cycle having reached its peak, with enhanced Fe deposition at the core site being a by-product of an increase in total aeolian Fe input from Australia and New Zealand, irrespective of sea-ice coverage.

These hypotheses rest on the assumption that total Fe deposition is equally bioavailable across glacial-interglacial periods, which has recently been questioned (Shoenfelt et al., 2018). Instead, the deposition of highly bioavailable Fe is documented to have been higher during glacial periods relative to interglacial periods, which may enhance the relative contribution of Fe fertilization to glacial-interglacial CO_2 variability (Shoenfelt et al., 2018). Despite this, an analysis of Fe speciation is outside the scope of this thesis and for simplicity it is assumed that total Fe deposition was equally bioavailable over the last 140 ka.

3.5 Future Work

Based on the data available, this chapter has outlined the possible roles that sea-ice expansion, a southern migration of the APF, changes in total productivity, and the effects of preservation and dilution may have had on opal burial at the TAN1302-96 core site. To confirm these hypotheses, additional data are needed, including:

[1] An increased number of proxies examined on TAN1302-96; and

[2] An increase in the spatial resolution of the analysis through measurements on nearby marine core TAN1302-97, and a data synthesis of all regional measurements across important frontal gradients.

3.5.1 Increased Number of Proxies on TAN1302-96

First, an increase in the number of proxies examined on TAN1302-96 could help resolve uncertainties surrounding the effects of sediment redistribution and dissolution. Specifically, the inclusion of a U-Th systematics analysis on TAN1302-96 could provide: (i) ^{230}Th measurements to calculate Th-normalized opal burial, which can identify if and where lateral sediment redistribution has contributed to changes in the mass accumulation rates (Section 3.5.1.1), (ii) measurements of changes in the ^{231}Pa/^{230}Th ratio, which can be used as a proxy for opal rain rates (Section 3.5.1.2), and (iii) changes in the concentrations of authigenic U, which can be used as a proxy for changes in ocean carbon export, deep-water oxygen content, and sediment corrosiveness (e.g., Francois et al., 2004; Costa et al., 2020) (Section 3.5.1.2). Additionally, an assessment of TAN1302-96's benthic δ^{13}C record could provide additional insights into deep water mass changes, which could be related to deep-water oxygen content and related dissolution (e.g., Tschumi et al., 2011).

3.5.1.1 Constant Flux Proxies

The addition of constant flux proxies (i.e., proxies that are produced in the water column at a constant and known rate) would help to determine whether the accumulation of sediment is from the vertical deposition from overlying waters or lateral sediment transport. Bacon (1984) suggested that the flux of ^{230}Th to the seafloor should, theoretically, be approximately equal to its known production rate throughout the ocean. The measured flux of ^{230}Th throughout the sediment core (after accounting for radioactive decay) would theoretically be equal to the rate of production if no redistribution has occurred (Bacon, 1984; Francois et al., 2004). This analysis, known as Th-normalization, can provide estimates of lateral sediment redistribution by identifying post-depositional sediment winnowing or accumulation, allowing for the calculation of Th-normalized burial rates and increased certainty regarding sedimentary chronology (Francois et al., 2004). Lateral redistribution is particularly strong in this region as strong bottom currents within the Southern Ocean have been documented to laterally transport a significant amount of

sediment (Dezileau et al., 2000**)**. Thus, the addition of ^{230}Th measurements to normalize biogenic fluxes throughout TAN1302-96 would allow for an accurate calculation of opal burial rates.

3.5.1.2 Dissolution Proxies

To resolve uncertainties regarding dissolution, other components of the U-Th systematics analysis, including ^{231}Pa/^{230}Th and authigenic U, and an analysis of benthic δ^{13}C, could provide insights surface water productivity, organic rain rates, and bottom water oxygenation conditions (Chase et al., 2003; Francois et al., 2004; Tschumi et al., 2011). Previous work has shown that ^{231}Pa preferentially scavenges to raining opal, suggesting that elevated ^{231}Pa/^{230}Th ratios can be used as an indicator of increased diatom rain rates and surface productivity (e.g., Anderson et al., 1983; Kumar et al., 1993; Chase et al., 2003; Bradtmiller et al., 2006). In other words, if periods of elevated ^{231}Pa/^{230}Th are present while opal concentration is low, dissolution of opal may be occurring. Deep-water corrosiveness also contributes to opal and $CaCO_3$ dissolution (e.g., Hayward et al., 2004), and therefore an assessment of past deep-water characteristics could provide additional supporting information on preservation. Authigenic U is often completely absent in oxic sediments, suggesting that its presence is indicative of an anoxic (or suboxic) environment caused by low oxygen bottom water content (Barnes & Cochran, 1990; Chase et al., 2001; Francois et al., 2004; McManus et a., 2005). Alternatively, high oxygen consumption by respiration of organic matter can lead to authigenic U precipitation (Thiagarajan and McManus, 2019), suggesting that its presence may also be interpreted as a proxy for high rates of carbon export from the surface (e.g., Kumar et al., 1995; Anderson et al., 1998; Chase et al., 2003). If the results show the presence of authigenic U in TAN1302-96, this could suggest low oxygen content and the potential for opal and carbonate dissolution. Relatedly, the inclusion of the benthic δ^{13}C signature could supplement the authigenic U analysis and provide additional information on the deep-water oxygen content, as benthic δ^{13}C is influenced by the dissolved inorganic carbon (DIC), which itself is determined by the remineralization of organic matter (Schmiedl and Mackensen, 2006; Tschumi et al., 2011). Higher rates of remineralization would result in a more negative (lighter) δ^{13}C, suggesting reduced dissolved oxygen and therefore enhanced corrosiveness (Tschumi et al., 2011).

The U-Th systematics analysis, which includes an analysis of ^{230}Th, ^{231}Pa/^{230}Th, and authigenic U, is currently underway by Zanna Chase and colleagues at the University of Tasmania, and results are expected later in 2022.

3.5.2 Increased Spatial Representation

Secondly, increasing the spatial representation of these analyses through measurements on: [1] nearby marine core TAN1302-97; and [2] a larger synthesis of additional cores across the southwestern Pacific Ocean, could help resolve uncertainties relating to sea-ice extent, the possible southern migration of the APF during MIS 5e, and changes in productivity.

An analysis of marine core TAN1302-97 (57.26°S, 161.33°E, water depth 3544 m), which was extracted near TAN1302-96 just north of the modern-day APF (Figure 21), could provide supporting data to the results from this thesis. The addition of WSIP and SSST estimates from a diatom-based MAT transfer function would provide additional records of past sea-ice expansion and SSST variability north of the modern-day APF and would increase confidence relating to glacial-interglacial sea-ice reconstructions for the region. A rough age model for TAN1302-97 was previously constructed in Liston (2018) and shows the core also captures a full glacial-interglacial cycle, which would allow for an independent comparison to TAN1302-96 and marine core SO136-111 (Crosta et al., 2004). Additionally, opal concentration and burial rates from TAN1302-97 would allow for a more adequate testing of the SALH, as the core site sites north of the APF and may capture the hypothesized dipole in opal productivity on either side of the modern APF.

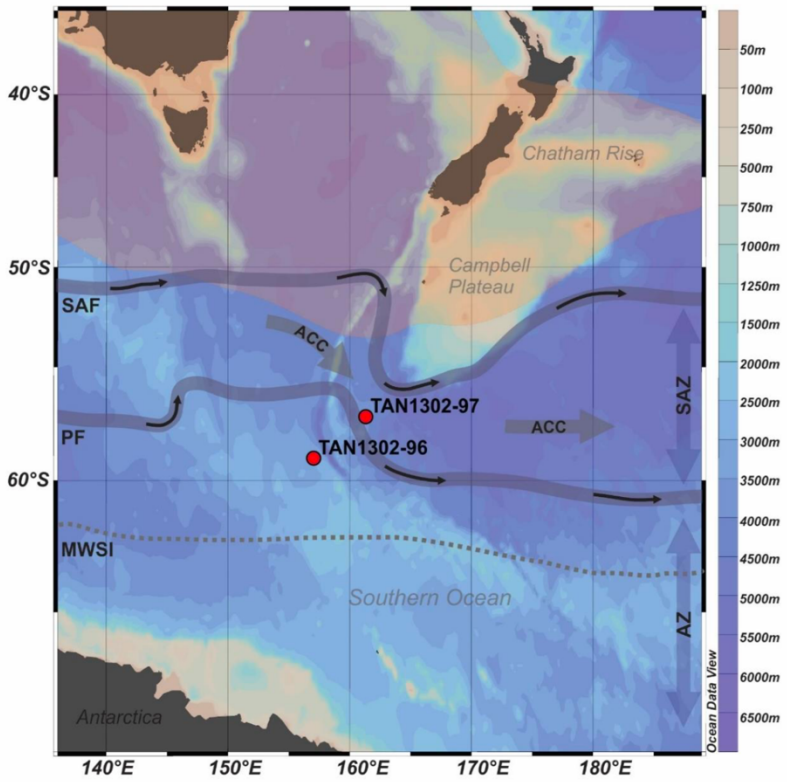

Figure 21: *Map of the southwestern Pacific sector of the Southern Ocean, including the locations of both TAN1302-96 (this study) and TAN1302-97. This figure was taken from Liston (2018).*

Additionally, a synthesis of all available data from across the southwestern Pacific sector of the Southern Ocean could provide important data on the possible southern migration of the APF during MIS 5e, the latitudinal extent of sea-ice expansion in the region, and changes in total primary productivity (both opal and $CaCO_3$). A regional assessment of SST was conducted in Chapter 2, and although most of the cores included are located too far north to capture sea-ice expansion and a southern migration of the APF, they could serve as a starting point to assess large-scale frontal changes across the region. These additional analyses would help support the hypotheses outlined in the previous section and would provide useful information on past surface water and frontal changes in this region over the last 140 ka.

3.6 Summary & Conclusion

This chapter has considered the temporal relationships between opal, carbonate, iron, and winter sea-ice coverage at marine core TAN1302-96 over a full glacial-interglacial cycle to better understand the larger processes that govern opal burial. Within the Southern Ocean, opal burial is considered an important component of understanding how Si production and surface Si utilization may have changed in the past and therefore contributed to changes in atmospheric CO_2 concentrations (Brzezinski et al., 2002; Matsumoto et al., 2002; Chase et al., 2015). The Antarctic Polar Front Zone and Subantarctic Zones are areas of particular interest because of the nearby formation of intermediate waters, which supply the low- and mid-latitudes with nutrients (Anderson et al., 2009). According to the SALH, sufficient silicic acid 'leaked' out of the Southern Ocean during past glacials and allowed diatoms to outcompete carbonate-based organisms, ultimately leading to a net-CO_2 drawdown (Brzezinski et al., 2002; Matsumoto et al., 2002). While previous assessments of the interplay between these factors have been completed (e.g., Chase et al., 2003; Bradtmiller et al., 2009; Chase et al., 2015), most focus primarily on the LGM to Holocene and lack the temporal resolution to interpret their relationship during glacial inception and across a full glacial-interglacial cycle. To better understand these relationships, I have produced new measurements of opal concentrations and MARs from TAN1302-96 and compared them to WSIP estimates produced in Chapter 2 and previously collected iron and $CaCO_3$ concentrations back to 140 ka BP.

The results from this analysis suggest that opal concentrations reached their lowest values during both warm interglacial periods, such as MIS 5e (125 ka BP), as well as during cold glacial periods of the MIS 3/4 boundary (56 ka BP) and the LGM (18 ka BP), while sea ice expanded over the core site only during MIS 2, 4, and 6. $CaCO_3$ concentrations appear to have an inverse relationship to opal concentrations, with relatively low values throughout the core except during MIS 5e (127 ka BP), the 3/4 boundary (56 ka BP), and the Holocene, where concentrations increased. Fe concentrations remained low throughout the core, with peak concentrations occurring during glacial stages of MIS 2, 4, and 6, largely in agreement with past reconstructions of the glacial dust cycle across the Pacific (e.g., Kohfeld and Harrison, 2001; Lambert et al., 2015; Wu et al., 2021). Considering the data together over the last 140 ka, the interplay between opal, carbonate, sea ice, and Fe can be summarized as follows:

- Sea-ice expansion appears to have limited opal burial during cool glacial periods of MIS 2 and 4, but perhaps not during the glacial period of MIS 6.

- The high concentrations of Fe during cold glacial periods of MIS 2 and 4 may also have caused a reduction in the Si:N, uptake ratio of diatoms which caused the raining opal to be more susceptible to dissolution, contributing to low opal concentrations during these periods.

- A polarward shift in the APF during the warm interglacial period of MIS 5e may have caused the TAN1302-96 core site to be located beneath the carbonate-dominant waters of the Subantarctic Zone, driving the $CaCO_3$ concentrations to increase.

- An increase in total primary production during the warm interglacial period of the Holocene may have driven the high opal, $CaCO_3$, and total MARs. Similar behavior (increases in all MARs) is seen in during the brief, peak interglacial period of MIS5e.

- Dilution of opal by $CaCO_3$ may have played a minor role in influencing opal concentrations throughout the core.

- Dissolution may have contributed to fluctuations in opal concentration throughout the core, either directly (opal dissolution) or indirectly ($CaCO_3$ dissolution).

Overall, the results from the opal analysis are generally in agreement with the literature from the region and suggest that diatom productivity south of the APF may have been lower during the last glacial relative to the Holocene (e.g., Chase et al., 2003; Bradtmiller et al., 2009; Chase et al., 2015). Additional data will help to better diagnose the contributions of productivity, Fe fertilization, sea-ice expansion, and dissolution. These data could include: [1] an increased number of proxies examined on TAN1302-96, including a U-Th systematics analysis and an analysis of the benthic $\delta^{13}C$ record, and [2] an increase in the spatial coverage of data through measurements on nearby marine core TAN1302-97 and a data synthesis of all regional measurements across important frontal gradients (Table 3).

MIS	Time Period/Event	Proposed Mechanism	Observed Change in Opal Concentrations?	Additional Data Needed to Support Our Hypothesis	How Would This Additional Data Support Our Hypothesis?
MIS 6	140 ka BP	Reduced $CaCO_3$ preservation	Increase	[1] Authigenic U & $\delta^{13}C$; [2] Increased spatial resolution	[1] The inclusion of an authigenic U and $\delta^{13}C$ analysis could assist with the interpretation of the low $CaCO_3$ concentrations during MIS 6 in both TAN1302-96 and nearby core SO136-111. If authigenic U is present and the $\delta^{13}C$ signature is very light during this time, carbonate dissolution may be occurring because of corrosive overlying waters, thereby increasing opal concentration via reduced dilution. [2] Increased spatial resolution could help determine if the carbonate minima event in SO136-111 and the low carbonate values in TAN1302-96 are observed elsewhere in the region, or if they are a unique event specific to this area. If they are unique to these cores, additional insights may be gained from more cores throughout the region.
MIS 5e	123 ka BP	Southern migration of the APF	Decrease	[1] Increased spatial resolution	[1] Increased spatial resolution could help identify a possible southern migration of the APF in additional cores using the same analyses conducted on TAN1302-96 in this chapter.
MIS 4	55-65 ka BP	Sea-ice expansion	Decrease	[1] Increased spatial resolution	[1] Increased spatial resolution could help constrain sea-ice expansion in the region and provide additional records to understand regional coverage.
		Fe-induced shift in Si:N uptake ratio	Decrease	[1] $^{231}Pa/^{230}Th$ ratio analysis; [2] Increased spatial resolution	[1] The addition of a $^{231}Pa/^{230}Th$ ratio analysis could help determine if dissolution is occurring. Elevated $^{231}Pa/^{230}Th$ ratios could suggested opal dissolution, which could support the hypothesis that Fe input is influencing the Si:N uptake ratio of diatoms, causing them to be more susceptible to dissolution. [2] Increased spatial resolution could help identify if other cores have elevated iron and $^{231}Pa/^{230}Th$ during this time, which may support this hypothesis.
MIS 3	37-55 ka BP	Increased opal productivity	Increase	[1] Increased spatial resolution	[1] Increased spatial resolution could help constrain sea-ice expansion in the region and provide additional records to understand regional coverage. If the brief retreat of sea ice caused the temporary increase in opal burial during this stage, additional cores could help support this hypothesis.
MIS 2	18-30 ka BP	Sea ice-expansion	Decrease	[1] Increased spatial resolution	[1] Increased spatial resolution could help constrain sea-ice expansion in the region and provide additional records to understand regional coverage.
		Fe-induced shift in Si:N uptake ratio	Decrease	[1] $^{231}Pa/^{230}Th$ ratio analysis; [2] Increased spatial resolution	[1] The addition of a $^{231}Pa/^{230}Th$ ratio analysis could help determine if dissolution is occurring. Elevated $^{231}Pa/^{230}Th$ ratios could suggested opal dissolution, which could support the hypothesis that Fe input is influencing the Si:N uptake ratio of diatoms, causing them to be more susceptible to dissolution. [2] Increased spatial resolution could help identify if other cores have elevated iron and $^{231}Pa/^{230}Th$ during this time, which could support this hypothesis.

Holocene	0-12 ka BP	Increased opal productivity	Increase	[1] $^{231}Pa/^{230}Th$ ratio analysis; [2] Increased spatial resolution	[1] The addition of a $^{231}Pa/^{230}Th$ ratio analysis would help support the MAR results by providing an independent proxy for opal rain rates. [2] Increased spatial resolution could help support the hypothesis of enhanced productivity in the region, as outlined by Bradtmiller et al. (2009) and others.

***Table 3**: Synthesis of proposed mechanisms driving observed changes in opal concentration over the last 140 ka BP. Time period refers to the period within the MIS where changes in opal concentration is being explained, 'Proposed Mechanism' refers to the hypothesized driver of concentration changes as identified in the discussion section, 'Observed Change in Opal Concentrations?' refers to whether the proposed mechanism increased or deceased concentrations, 'Additional Data Needed to Confirm' refers to additional proxy data or analyses that are required to support the proposed hypothesis, and 'How Would This Data Support Our Findings' describes how the additional data would be used to help resolve uncertainties associated with this hypothesis.*

Chapter 4: Thesis Conclusion

The specific mechanism(s) driving the ~80 ppm decrease in atmospheric CO_2 during glacial periods has remained unknown since it was first discovered in Antarctic ice cores in the 1980s (Delmas, 1980; Neftel et al., 1982). While numerous studies have provided compelling arguments outlining the possible physical and biological mechanisms that explain the reduction in CO_2, significant debate continues regarding the precise timing and contributions of each proposed mechanism (e.g., Kohfeld and Chase, 2017). The discussion surrounding Antarctic sea ice and its physical and biological effects on atmospheric CO_2 have gained momentum within the paleoscience community, and efforts to reconstruct past sea-ice extent, including the work by the Cycles of Sea-Ice Dynamics in the Earth System (C-SIDE) working group, have helped produce more quantitative reconstructions to constrain latitudinal expansion back in time. Within this thesis, I have provided a comprehensive introduction to climate proxies, their application, and why Antarctic sea ice is believed to be an important contributor to glacial-interglacial CO_2 variability. Secondly, I, along with several members of the C-SIDE working group, have produced the second regional winter sea ice concentration (WSIC) and summer sea surface temperature (SSST) reconstruction estimates over the last 140 ka using marine core TAN1302-96 taken from the southwestern Pacific sector of the Southern Ocean. Finally, I have provided new opal concentration and mass accumulation rates throughout TAN1302-96 and have linked these to fundamental processes operating within the Southern Ocean to better understand the interplay between opal burial, iron deposition, and sea-ice expansion over a full glacial-interglacial cycle.

The WSIC and SSST reconstructions from TAN1302-96 provide an important new dataset for understanding the full glacial-interglacial variability of sea-ice extent in the southwestern Pacific sector of the Southern Ocea. The results from Chapter 2 show that winter sea ice expanded over the core site during MIS 2, 4, and 6, and while sea ice was largely consolidated in the region during these times, its absence during MIS 5d suggests that it may not have played a key role in early glacial atmospheric CO_2 drawdown, as hypothesized in Kohfeld and Chase (2017). The expansion of sea ice does however appear to coincide with periods of Antarctic Intermediate Water (AAIW) shoaling, as determined from carbon isotope signatures in benthic foraminifera records from several

nearby intermediate-depth sediment cores. We interpret this relationship to suggest that the enhanced sea ice melt caused a local buoyancy gain through an increased freshwater flux into the AAIW formation region, which may have resulted in an inhibition of its downward expansion that was coincident with a volumetric expansion of carbon-rich deep waters. An additional comparison of regional SSST gradients with the estimated SSST from TAN1302-96 suggests that early glacial (i.e., MIS 5d) cooling may have played a key role in early glacial atmospheric CO_2 sequestration through air-sea disequilibrium.

The new opal concentration estimates provided in Chapter 3 form the starting point for a future analysis to understand the interplay between opal, carbonate, iron, and sea ice within the region over a full glacial-interglacial cycle. This analysis helps set the stage for future work by introducing the possible drivers of changes in opal concentration and burial at the TAN1302-96 core site. These preliminary comparisons suggest that sea-ice expansion during cool glacial periods of MIS 2 and 4 and a poleward migration of the Antarctic Polar Front (APF) during the warm interglacial period of MIS 5e may have limited opal burial at these times. Iron concentrations have an inverse relationship to opal concentrations, suggesting that periods with enhanced iron deposition may result in a reduction in the Si:N uptake ratio, supporting the Silicic Acid Leakage Hypothesis (SALH). Overall, the results from TAN1302-96 show higher opal burial rates during the Holocene relative to the last glacial period. Additional data, such as a U-Th systematics analysis, the inclusion of nearby marine core TAN1302-97, and a larger regional synthesis of nearby cores will help in creating a comprehensive picture of the role of sea-ice, Fe deposition, marine productivity, and front migration in controlling diatom productivity (and surface ocean Si cycling) during the glacial-interglacial cycle.

This research is part of the larger work by the C-SIDE working group and has contributed to our understanding of the role of sea ice in contributing to glacial-interglacial CO_2 variability. These results represent the 6th quantitative Antarctic sea ice reconstruction covering a full glacial-interglacial cycle, and the first in the region directly linking sea ice growth to fluctuations in intermediate water production and subduction variability. These results also contribute an additional datapoint to help better understand sea-ice dynamics and refine our predictive models, which are currently unable to reconstruct the observed expansion from 1979 to 2014 (Maksym, 2019; Parkinson, 2019). Despite our coordinated efforts, glacial-interglacial sea ice reconstructions still lack the spatial resolution needed to fully understand the extent of expansion over the last glacial-interglacial cycle. The

continued work by the C-SIDE working group to produce new sea-ice reconstructions are particularly useful in refining our understanding of sea-ice dynamics during glacial inception and can help fine-tune our climate models to better predict future changes in sea-ice coverage in a changing climate.

References

Abernathey, R. P., Cerovecki, I., Holland, P. R., Newsom, E., Mazloff, M., and Talley, L. D. (2016). Water-mass transformation by sea ice in the upper branch of the Southern Ocean overturning. Nature Geoscience, 9(8), 596–601. https://doi.org/10.1038/ngeo2749

Ackley, S.F. (1981). A review of sea-ice weather relationships in the Southern Hemisphere. In: Allison, I. (Ed.), Sea Level, Ice, and Climate Change. IAHS Publication, pp. 127e159.

Allen, C., Pike, J., & Pudsey, C. J. (2011). Last glacial–interglacial sea-ice cover in the SW Atlantic and its potential role in global deglaciation. Quaternary Science Reviews, 30(19), 2446–2458. https://doi.org/10.1016/j.quascirev.2011.04.002

Alves, E., Macario, K., Ascough, P., & Bronk Ramsey, C. (2018). The Worldwide Marine Radiocarbon Reservoir Effect: Definitions, Mechanisms, and Prospects. Reviews of Geophysics (1985), 56(1), 278–305. https://doi.org/10.1002/2017RG000588

Anderson, R.F., Bacon, M., & Brewer, P. (1983). Removal of 230Th and 231Pa from the open ocean. Earth and Planetary Science Letters, 62(1), 7–23. https://doi.org/10.1016/0012-821X(83)90067-5

Anderson, R.F., Kumar, N., Mortlock, R., Froelich, P., Kubik, P., Dittrich-Hannen, B., & Suter, M. (1998). Late-Quaternary changes in productivity of the Southern Ocean. Journal of Marine Systems, 17(1), 497–514. https://doi.org/10.1016/S0924-7963(98)00060-8

Anderson, D., Glibert, P. M., & Burkholder, J. M. (2002). Harmful Algal Blooms and Eutrophication: Nutrient Sources, Composition, and Consequences. Estuaries, 25(4), 704–726. https://doi.org/10.1007/BF02804901

Anderson, R. F., Ali, S., Bradtmiller, L. I., Nielsen, S. H. H., Fleisher, M. Q., Anderson, B. E. and Burckle, L. H. (2009). Wind-Driven Upwelling in the Southern Ocean and the Deglacial Rise in Atmospheric CO. Science (American Association for the Advancement of Science), 323(5920), 1443–1448. https://doi.org/10.1126/science.1167441

Archer, D., Lyle, M., Rodgers, K., & Froelich, P. (1993). What Controls Opal Preservation in Tropical Deep-Sea Sediments? Paleoceanography, 8(1), 7–21. https://doi.org/10.1029/92PA02803

Archer, D., and Johnson, K. (2000). A model of the iron cycle in the ocean. Global Biogeochemical Cycles, 14(1), 269–279. https://doi.org/10.1029/1999GB900053

Archer, D.E., Martin, P.A., Milovich, J., Brovkin, V., Plattner, G.K., and Ashendel, C. (2003). Model sensitivity in the effect of Antarctic sea ice and stratification on atmospheric pCO2. Paleoceanography, 18(1): 1012. https://doi.org/10.1029/2002PA000760

Armand, L., Ferry, A., and Leventer, A. (2017). Advances in paleo sea ice estimation. Sea ice (3) 600-629.

Ascough, P.L., Cook, G.T., & Dugmore, A. (2005) Methodological approaches to determining the marine radiocarbon reservoir effect. Progress in Physical Geography, 29 (4). pp. 532-547. ISSN 0309-1333

Assmy, P., Ciewski, B., Henjes, J., Klaas, C., Montresor, M., & Smetacek, V. (2014). Response of the protozooplankton assemblage during the European Iron Fertilization Experiment (EIFEX) in the Antarctic circumpolar current. Journal of Plankton Research, 36(5), 1175–1189. https://doi.org/10.1093/plankt/fbu068

Bacon, M. P. (1984), Glacial to interglacial changes in carbonate and clay sedimentation in the Atlantic Ocean estimated from 230Th measurements, Isotope Geosci., 2, 97–111. https://doi.org/10.1016/0009-2541(84)90183-9

Bard, E., Hamelin, B., Fairbanks, R.G. & Zindler, A. (1990) Calibration of the 14C timescale over the past 30,000 years using mass spectrometric U-Th ages from Barbados corals. Nature, 345, 405-410.

Bard, E., Arnold, M., Fairbanks, R. G. & Hamelin, B. (1993) 230Th/ 234U and 14C ages obtained by mass spectrometry on corals. Radiocarbon, 35 (1), 137-189.

Barnes, C.E., & Cochran, J. (1990). Uranium removal in oceanic sediments and the oceanic U balance. Earth and Planetary Science Letters, 97(1), 94–101. https://doi.org/10.1016/0012-821X(90)90101-3

Bassinot, F., Labeyrie, L. D., Vincent, E., Quidelleur, X., Shackleton, N. J., & Lancelot, Y. (1994). The astronomical theory of climate and the age of the Brunhes-Matuyama magnetic reversal. Earth and Planetary Science Letters, 126(1), 91–108. https://doi.org/10.1016/0012-821X(94)90244-5

Bayliss, A. (2015). Quality in Bayesian chronological models in archaeology. *World Archaeology*, *47*(4), 677–700. https://doi.org/10.1080/00438243.2015.1067640

Benz, V., Esper, O., Gersonde, R., Lamy, F., and Tiedemann, R. (2016). Last Glacial Maximum sea surface temperature and sea-ice extent in the Pacific sector of the Southern Ocean. Quaternary Science Reviews, 146: 216–237. https://doi.org/10.1016/j.quascirev.2016.06.006

Bianchi, C., and Gersonde, R. (2002). The Southern Ocean surface between Marine Isotope Stages 6 and 5d: shape and timing of climate changes. Paleogeography, Paleoclimatology, Paleoecology, 187: 151–177.

Bereiter, B., Eggleston, S., Schmitt, J., Nehrbass-Ahles, C., Stocker, T.F., Fischer, H., Kipfstuhl, S., and Chappellaz, J. (2015). Revision of the EPICA Dome C CO2 record from 800 to 600 kyr before present. Geophysical Research Letters, 42(2): 542–549. https://doi.org/10.1002/2014GL061957

Blaauw, M. & Christen, J. A. (2011). Flexible paleoclimate age-depth models using an autoregressive gamma process. Bayesian Analysis, 6(3): 457-474. https://doi.org/10.1214/11-BA618

Bostock, H., Opdyke, B. N., Gagan, M. K., & Fifield, L. K. (2004). Carbon isotope evidence for changes in Antarctic Intermediate Water circulation and ocean ventilation in the southwest Pacific during the last deglaciation. Paleoceanography, 19(4): PA4013–n/a. https://doi.org/10.1029/2004PA001047

Bostock, H., Barrows, T., Carter, L., Chase, Z., Cortese, G., Dunbar, G., Ellwood, M., Hayward, B., Howard, W., Neil, H., Noble, T., Mackintosh, A., Moss, P., Moy, A., White,

D., Williams, M. J., & Armand, L. (2013). A review of the Australian–New Zealand sector of the Southern Ocean over the last 30 ka (Aus-INTIMATE project). Quaternary Science Reviews, 74, 35–57. https://doi.org/10.1016/j.quascirev.2012.07.018

Bostock, H., Hayward, B., Neil, H., Sabaa, A., & Scott, G. (2015). Changes in the position of the Subtropical Front south of New Zealand since the last glacial period. Paleoceanography, 30(7), 824–844. https://doi.org/10.1002/2014PA002652

Bouttes, N., Paillard, D., and Roche, D. M. (2010). Impact of brine-induced stratification on the glacial carbon cycle. Climate of the Past, 6(5): 575–589. https://doi.org/10.5194/cp-6-575-2010

Boyd, P. (2002). Environmental factors controlling phytoplankton processes in the Southern Ocean. Journal of Phycology, 38(5), 844.

Boyd, P.W. (2012). Ocean Fertilization for Sequestration of Carbon Dioxide from the Atmosphere. In Geoengineering Responses to Climate Change (pp. 53–72). Springer New York. https://doi.org/10.1007/978-1-4614-5770-1_5

Boyle, E.D. (1998). Pumping iron makes thinner diatoms. Nature (London), 393(6687), 733–734. https://doi.org/10.1038/31585

Bradtmiller, L., Anderson, R., Fleisher, M., & Burckle, L. (2006) Diatom productivity in the equatorial Pacific Ocean from the last glacial period to the present: A test of the silicic acid leakage hypothesis, Paleoceanography, 21, https://doi.org/10.1029/2006PA001282

Bradtmiller, L.I., Anderson, R.F., Fleisher, M.Q. and Burckle, L.H. (2009). Comparing glacial and Holocene opal fluxes in the Pacific sector of the Southern Ocean. Paleoceanography, 24(2), PA2214–n/a. https://doi.org/10.1029/2008PA001693

Broecker, W. S., and T.-H. Peng (1982), Tracers in the sea, Lamont-Doherty Geol. Observ. Publ., Palisades, N. Y.

Bronk Ramsey, C. (1995). Radiocarbon Calibration and Analysis of Stratigraphy: The OxCal Program. Radiocarbon, 37(2), 425–430. https://doi.org/10.1017/S0033822200030903

Brzezinski, M.A., Pride, C. J., Franck, V. M., Sigman, D. M., Sarmiento, J. L., Matsumoto, K., Gruber, N., Rau, G. H., & Coale, K. H. (2002). A switch from Si(OH)4 to NO3− depletion in the glacial Southern Ocean. Geophysical Research Letters, 29(12), 5–1–5–4. https://doi.org/10.1029/2001GL014349

Buck, C., and Juarez, M. (2017). Bayesian radiocarbon modelling for beginners. University of Sheffield. Retrived from: https://arxiv.org/pdf/1704.07141.pdf

Burckle, L.H. and Mortlock, R. (1998). Sea-ice extent in the Southern Ocean during the Last Glacial Maximum: another approach to the problem. Annals of Glaciology, 27, 302–304. https://doi.org/10.3189/1998AoG27-1-302-304

Burr, G.S., Beck, J. W., Taylor, F. W., Récy, J., Edwards, R. L., Cabioch, G., Corrège, T., Donahue, D. J., & O'malley, J. M. (1998). A High-Resolution Radiocarbon Calibration Between 11,700 and 12,400 Calendar Years Bp Derived from 230Th Ages of Corals from Espiritu Santo Island, Vanuatu. Radiocarbon, 40(3), 1093–1105. https://doi.org/10.1017/S0033822200019147

Butzin, M., Köhler, P., and Lohmann, G. (2017). Marine radiocarbon reservoir age simulations for the past 50,000 years. Geophysical Research Letters, 44(16), 8473–8480. https://doi.org/10.1002/2017GL074688

Butzin, M., Heaton, T.J., Köhler, P., and Lohmann, G. (2020). A short note on marine reservoir age simulations used in INTCAL20. Radiocarbon, 62(4), 1–7. https://doi.org/10.1017/RDC.2020.9

Cavalieri, D.J., Parkinson, C. L., & Vinnikov, K. Y. (2003). 30-Year satellite record reveals contrasting Arctic and Antarctic decadal sea ice variability. Geophysical Research Letters, 30(18), 1970–n/a. https://doi.org/10.1029/2003GL018031

Cavalieri, D.J. & Parkinson, C. L. (2008). Antarctic sea ice variability and trends, 1979–2006. Journal of Geophysical Research: Oceans, 113(C7): C07004–n/a. https://doi.org/10.1029/2007JC004564

Cefarelli, A.O., Ferrario, M.E., Almandoz, G.O., Atencio, A.G., Akselman, R., and Vernet, M. (2010). Diversity of the diatom genus Fragilariopsis in the Argentine Sea and

Antarctic waters: morphology, distribution and abundance. Polar Biology, 33(11): 1463–1484. https://doi.org/10.1007/s00300-010-0794-z

Chadwick, M., Allen, C. S., Sime, L. C., Crosta, X., & Hillenbrand, C.-D. (2022). Reconstructing Antarctic winter sea-ice extent during Marine Isotope Stage 5e. Climate of the Past, 18(1), 129–146. https://doi.org/10.5194/cp-18-129-2022

Chadwick, M., Allen, C.., Sime, L.., & Hillenbrand, C.-D. (2020). Analysing the timing of peak warming and minimum winter sea-ice extent in the Southern Ocean during MIS 5e. Quaternary Science Reviews, 229, 106134. https://doi.org/10.1016/j.quascirev.2019.106134

Chan, D. (2021). Combining Statistical, Physical, and Historical Evidence to Improve Historical Sea-Surface Temperature Records. Harvard Data Science Review. https://doi.org/10.1162/99608f92.edcee38f

Charles, C. D., P. N. Froelich, M. A. Zibello, R. A. Mortlock, and J. J. Morley (1991), Biogenic opal in Southern Ocean sediments over the last 450,000 years: Implications for surface water chemistry and circulation, Paleoceanography, 6, 697–728. https://doi.org/10.1029/91PA02477

Chase, Z., R. F. Anderson, M. Q. Fleisher, and P. W. Kubik (2002), The influence of particle composition and particle flux on scavenging of Th, Pa and Be in the ocean, Earth Planet. Sci. Lett., 204, 215–229. https://doi.org/10.1016/S0967-0645(02)00595-7

Chase, Z., Anderson, R. F., Fleisher, M. Q., & Kubik, P. W. (2003). Accumulation of biogenic and lithogenic material in the Pacific sector of the Southern Ocean during the past 40,000 years. Deep-Sea Research. Part II, Topical Studies in Oceanography, 50(3), 799–832. https://doi.org/10.1016/S0967-0645(02)00595-7

Chase, Z., Kohfeld, K. E., & Matsumoto, K. (2015). Controls on biogenic silica burial in the Southern Ocean. Global Biogeochemical Cycles, 29(10), 1599–1616. https://doi.org/10.1002/2015GB005186

CLIMAP Project Members (1976). The Surface of the Ice Age Earth: Quantitative geologic evidence is used to reconstruct boundary conditions for the climate 18,000

years ago. Science (American Association for the Advancement of Science), 191(4232), 1131–1137. https://doi.org/10.1126/science.191.4232.1131

CLIMAP Project Members (1981). Seasonal reconstructions of the Earth's surface at the last glacial maximum in Map Series, Technical Report MC-36. Boulder, Colorado: Geological Society of America

Comiso, J., Meier, W. N., & Gersten, R. (2017). Variability and trends in the Arctic Sea ice cover: Results from different techniques. Journal of Geophysical Research. Oceans, 122(8), 6883–6900. https://doi.org/10.1002/2017JC012768

Cooke, D. W., and Hays, J. D. (1982). Estimates of Antarctic Ocean seasonal sea-ice cover during glacial intervals. in Craddock, C., ed. Antarctic geoscience. Madison, WI, University of Wisconsin Press, pp. 1017–1025.

Cortese, G., Gersonde, R., Hillenbrand, C.-D., & Kuhn, G. (2004). Opal sedimentation shifts in the World Ocean over the last 15 Myr. Earth and Planetary Science Letters, 224(3), 509–527. https://doi.org/10.1016/j.epsl.2004.05.035

Costa, K.M., Hayes, C. T., Anderson, R. F., Pavia, F. J., Bausch, A., Deng, F., Dutay, J., Geibert, W., Heinze, C., Henderson, G., Hillaire-Marcel, C., Hoffmann, S., Jaccard, S. L., Jacobel, A. W., Kienast, S. S., Kipp, L., Lerner, P., Lippold, J., Lund, D., … Zhou, Y. (2020). 230 Th Normalization: New Insights on an Essential Tool for Quantifying Sedimentary Fluxes in the Modern and Quaternary Ocean. Paleoceanography and Paleoclimatology, 35(2), e2019PA003820. https://doi.org/10.1029/2019PA003820

Craig, H. (1957). Isotopic standards for carbon and oxygen and correction factors for mass-spectrometric analysis of carbon dioxide. Geochimica et Cosmochimica Acta, 12(1), 133–149. https://doi.org/10.1016/0016-7037(57)90024-8

Craig, H. (1961). Standard for Reporting Concentrations of Deuterium and Oxygen-18 in Natural Waters. Science (American Association for the Advancement of Science), 133(3467), 1833–1834. https://doi.org/10.1126/science.133.3467.1833

Crosta, X., Pichon, J.-J., and Burckle, L.H., (1998). Application of modern analog technique to marine Antarctic diatoms: reconstruction of maximum sea-ice extent at the Last Glacial Maximum. Paleoceanography, 13: 284–297.

Crosta, X., Sturm, A., Armand, L., and Pichon, J.-J., (2004). Late Quaternary sea ice history in the Indian sector of the Southern Ocean as recorded by diatom assemblages. Marine Micropaleontology, 50: 209–223.

Crosta, X., Shukla, S.K., Ther, O., Ikehara, M., Yamane, M., and Yokoyama, Y. (2020). Last Abundant Appearance Datum of Hemidiscus karstenii driven by climate change. Marine Micropaleontology, 157: 101861. https://doi.org/10.1016/j.marmicro.2020.101861

Dansgaard, W. (1964). Stable isotopes in precipitation. Tellus, 16(4), 436–468. https://doi.org/10.3402/tellusa.v16i4.8993

De Boer, A.M., & Hogg, A.M. (2014). Control of the glacial carbon budget by topographically induced mixing, Geophysical Research Letters, 41(12), 4277–4284. https://doi.org/10.1002/2014GL059963

De Baar, H., Buma, A., Nolting, R. F., Cadee, G. C., Jacques, G., and Treguer, P. J. (1990). On iron limitation of the Southern Ocean: experimental observations in the Weddell and Scotia Seas. Marine Ecology. Progress Series (Halstenbek), 65(2), 105–122. https://doi.org/10.3354/meps065105

de Vries H. (1958). Variation in concentration of radiocarbon with time and location on earth. Proceedings of the Koninklijke Nederlandse Akademie Van Wetenschappen Series B-Palaeontology Geology Physics Chemistry Anthropology B61:94–102

Delille, B., Vancoppenolle, M., Geilfus, N.X., Tilbrook, B., Lannuzel, D., Schoemann, V., Becquevort, S., Carnat, G., Delille, D., Lancelot, C., Chou, L., Dieckmann, G.S., and Tison, J.L. (2014). Southern Ocean CO2 sink: The contribution of sea ice. Journal of Geophysical Research, 119(9): 6340-3655. https://doi.org/10.1002/2014JC009941

Delmas, R.J., Ascencio, J.-M., & Legrand, M. (1980). Polar ice evidence that atmospheric CO2 20,000 yr BP was 50% of present. Nature (London), 284(5752), 155–157. https://doi.org/10.1038/284155a0

Denton, G., Anderson, R. F., Toggweiler, R., Edwards, R. L., Schaefer, M., & Putnam, A. E. (2010). The Last Glacial Termination. Science (American Association for the

Advancement of Science), 328(5986), 1652–1656. https://doi.org/10.1126/science.1184119

Dezileau, Bareille, G., Reyss, J., & Lemoine, F. (2000). Evidence for strong sediment redistribution by bottom currents along the southeast Indian ridge. Deep-Sea Research. Part I, Oceanographic Research Papers, 47(10), 1899–1936. https://doi.org/10.1016/S0967-0637(00)00008-X

Dubois, N., Kienast, M., Kienast, S., Calvert, S. E., François, R., & Anderson, R. F. (2010). Sedimentary opal records in the eastern equatorial Pacific: It is not all about leakage. Global Biogeochemical Cycles, 24(4), n/a–n/a. https://doi.org/10.1029/2010GB003821

Duplessy, J.C., Shackleton, N. J., Fairbanks, R. G., Labeyrie, L., Oppo, D., & Kallel, N. (1988). Deepwater source variations during the last climatic cycle and their impact on the global deepwater circulation. Paleoceanography, 3(3), 343–360. https://doi.org/10.1029/PA003i003p00343

Durand, A., Chase, Z., Noble, T. L., Bostock, H., Jaccard, S. L., Kitchener, P., Townsend, A. T., Jansen, N., Kinsley, L., Jacobsen, G., Johnson, S., and Neil, H. (2017). Export production in the New-Zealand region since the Last Glacial Maximum. Earth and Planetary Science Letters, 469, 110–122. https://doi.org/10.1016/j.epsl.2017.03.035

Eggleston, S., and E.D. Galbraith. (2018). The devil's in the disequilibrium: multi-component analysis of dissolved carbon and oxygen changes under a broad range of forcings in a general circulation model. Biogeosciences 15: 3761-3777.

Emerson, S.R., & Archer, D. (1990). Calcium Carbonate Preservation in the Ocean. Philosophical Transactions of the Royal Society of London. Series A: Mathematical and Physical Sciences, 331(1616), 29–40. https://doi.org/10.1098/rsta.1990.0054

Emiliani, C. (1955). Pleistocene Temperatures. The Journal of Geology, 63(6), 538–578. https://doi.org/10.1086/626295

Esper, O., and Gersonde, R. (2014). New tools for the reconstruction of Pleistocene Antarctic Sea ice. Palaeogeography, Paleoclimatology, Paleoecology, 399: 260–283. https://doi.org/10.1016/j.palaeo.2014.01.019

Fenner, J., Schrader, H., and Wienigk, H. (1976). Diatom Phytoplankton Studies in the Southern Pacific Ocean, Composition and Correlation to the Antarctic Convergence and Its Paleoecological Significance.

Ferrari, R., Jansen, M.F., Adkins, J.F., Burke, A., Stewart, A.L., Thompson, A.F. (2014). Antarctic sea ice control on ocean circulation in present and glacial times. Proceedings of the National Academy of Sciences of the United States of America, 111: 8753–8758.

Ferry, A.J., Crosta, X., Quilty, P.G., Fink, D., Howard, W., and Armand, L.K. (2015). First records of winter sea ice concentration in the southwest Pacific sector of the Southern Ocean. Paleoceanography, 30(11): 1525–1539. https://doi.org/10.1002/2014pa002764

Fischer, H., Meissner, K. J., Mix, A. C., Abram, N. J., Austermann, J., Brovkin, V., Capron, E., Colombaroli, D., Daniau, A. L., Dyez, K. A., Felis, T., Finkelstein, S. A., Jaccard, S. L., McClymont, E. L., Rovere, A., Sutter, J., Wolff, E. W., Affolter, S., Bakker, P., … Ziegler, M. (2018). Palaeoclimate constraints on the impact of 2 °C anthropogenic warming and beyond. Nature Geoscience, 11(7), 474–485. https://doi.org/10.1038/s41561-018-0146-0

Francois, R., Frank, M., Rutgers van der Loeff, M. M., & Bacon, M. P. (2004). 230Th normalization: An essential tool for interpreting sedimentary fluxes during the late Quaternary. Paleoceanography, 19(1), PA1018–n/a. https://doi.org/10.1029/2003PA000939

Freeman, N.M, Lovenduski, N. S., Munro, D. R., Krumhardt, K. M., Lindsay, K., Long, M. C., & Maclennan, M. (2018). The Variable and Changing Southern Ocean Silicate Front: Insights From the CESM Large Ensemble. Global Biogeochemical Cycles, 32(5), 752–768. https://doi.org/10.1029/2017GB005816

Froelich, P. N. (1991). Biogenic opal and carbonate accumulation rates in the Subantarctic South Atlantic: The late Neogene of Meteor Rise site 704. Proceedings of the Ocean Drilling Program, Scientific Results, 120, 515–549.

Fryxell, G.A., Hasle, G.R. (1976). The genus Thalassiosira: some species with a modified ring of central strutted processes. Nova Hedwigia Beihefte, 54: 67-98.

Fryxell, G.A., Hasle, G.R., (1980). The marine diatom Thalassiosira oestrupii: structure, taxonomy and distribution. American Journal of Botany, 67: 804-814.

Galbraith, E., and de Lavergne, C. (2019). Response of a comprehensive climate model to a broad range of external forcings: relevance for deep ocean ventilation and the development of late Cenozoic ice ages. Climate Dynamics, 52(1), 653–679. https://doi.org/10.1007/s00382-018-4157-8

Gersonde, R., and Zielinski, U. (2000). The reconstruction of late Quaternary Antarctic sea-ice distribution—the use of diatoms as a proxy for sea-ice. Palaeogeography, Palaeoclimatology, Palaeoecology, 162(3), 263–286. https://doi.org/10.1016/S0031-0182(00)00131-0

Gersonde, R., Crosta, X., Abelmann, A., and Armand, L. (2005). Sea-surface temperature and sea ice distribution of the Southern Ocean at the EPILOG last Glacial Maximum—a circum-Antarctic view based on siliceous microfossil records. Quaternary Science Reviews, 24 (7–9): 869–896.

Ghadi, P., Nair, A., Crosta, X., Mohan, R., Manoj, M.C, and Meloth, T. (2020). Antarctic sea-ice and palaeoproductivity variation over the last 156,000 years in the Indian sector of Southern Ocean. Marine Micropaleontology, 160: 101894. https://doi.org/10.1016/j.marmicro.2020.101894

Gordon, J.E., & Harkness, D.D. (1992). Magnitude and geographic variation of the radiocarbon content in Antarctic marine life: Implications for reservoir corrections in radiocarbon dating. Quaternary Science Reviews, 11(7-8), 697–708. https://doi.org/10.1016/0277-3791(92)90078-M

Gottschalk, J., Skinner, L. C., Lippold, J., Vogel, H., Frank, N., Jaccard, S. L., & Waelbroeck, C. (2016). Biological and physical controls in the Southern Ocean on past millennial-scale atmospheric CO2 changes. Nature Communications, 7(1), 11539–11539. https://doi.org/10.1038/ncomms11539

Govin, A., Michel, E., Labeyrie, L., Waelbroeck, C., Dewilde, F., and Jansen, E. (2009), Evidence for northward expansion of Antarctic Bottom Water mass in the Southern Ocean during the last glacial inception, Paleoceanography, 24, PA1202, doi:10.1029/2008PA001603.

Graham, R.M. & De Boer, A. M. (2013). The Dynamical Subtropical Front. Journal of Geophysical Research. Oceans, 118(10), 5676–5685. https://doi.org/10.1002/jgrc.20408

Gregoire, L., Valdes, P. J., & Payne, A. J. (2015). The relative contribution of orbital forcing and greenhouse gases to the North American deglaciation. Geophysical Research Letters, 42(22), 9970–9979. https://doi.org/10.1002/2015GL066005

Guiot, J., de Beaulieu, J.L., Chceddadi, R., David, F., Ponel, P., Reille, M. (1993). The climate of western Europe during the last Glacial/Interglacial cycle derived from pollen and insect remains. Palaeogeography, Palaeoclimatology, Palaeoecology, 103: 73–93.

Guiot, J., and de Vernal, A. (2011). Is spatial autocorrelation introducing biases in the apparent accuracy of paleoclimatic reconstructions? Quaternary Science Reviews, 30(15-16): 1965–1972. https://doi.org/10.1016/j.quascirev.2011.04.022

Hasle G.R., and Syvertsen, E.E. (1997) Marine diatoms. In: Tomas CR (ed) Identifying marine phytoplankton. Academic Press, pp 5–385.

Hays, J.D., Lozano, J.A., Shackleton, N., and Irving, G. (1976). Reconstruction of the Atlantic and western Indian Ocean sectors of the 18,000 B.P. Antartic Ocean. (1977). Deep-Sea Research (1977), 24(4), 273. https://doi.org/10.1016/0146-6291(77)90297-1

Hayward, B., Sabaa, A., & Grenfell, H. R. (2004). Benthic foraminifera and the late Quaternary (last 150 ka) paleoceanographic and sedimentary history of the Bounty Trough, east of New Zealand. Palaeogeography, Palaeoclimatology, Palaeoecology, 211(1), 59–93. https://doi.org/10.1016/j.palaeo.2004.04.007

Hayward, B.W., Scott, G. H., Crundwell, M. P., Kennett, J. P., Carter, L., Neil, H. L., Sabaa, A. T., Wilson, K., Rodger, J. S., Schaefer, G., Grenfell, H. R., & Li, Q. (2008). The effect of submerged plateaux on Pleistocene gyral circulation and sea-surface

temperatures in the Southwest Pacific. Global and Planetary Change, 63(4), 309–316. https://doi.org/10.1016/j.gloplacha.2008.07.003

Heaton, T., Köhler, P., Butzin, M., Bard, E., Reimer, R., Austin, W., Bronk Ramsey, C., Grootes, P., Hughen, K., Kromer, B., Reimer, P., Adkins, J., Burke, A., Cook, M., Olsen, J., and Skinner, L. (2020). Marine20—The Marine Radiocarbon Age Calibration Curve (0–55,000 cal BP). Radiocarbon, 62(4), 779–820. https://doi.org/10.1017/RDC.2020.68

Hildebrand, M., Lerch, S. J. L., & Shrestha, R. P. (2018). Understanding Diatom Cell Wall Silicification—Moving Forward. Frontiers in Marine Science, 5. https://doi.org/10.3389/fmars.2018.00125

Hobbs, W.R., Massom, R., Stammerjohn, S., Reid, P., Williams, G., & Meier, W. (2016). A review of recent changes in Southern Ocean sea ice, their drivers and forcings. Global and Planetary Change, 143(C), 228–250. https://doi.org/10.1016/j.gloplacha.2016.06.008

Hodell, D.A., Charles, C., & Sierro, F. (2001). Late Pleistocene evolution of the ocean's carbonate system. Earth and Planetary Science Letters, 192(2), 109–124. https://doi.org/10.1016/S0012-821X(01)00430-7

Holloway, M., Sime, L. C., Allen, C. S., Hillenbrand, C., Bunch, P., Wolff, E., & Valdes, P. J. (2017). The Spatial Structure of the 128 ka Antarctic Sea Ice Minimum. Geophysical Research Letters, 44(21), 11,129–11,139. https://doi.org/10.1002/2017GL074594

Honjo, S. (2004) 'Particle export and the biological pump in the Southern Ocean', Antarctic Science. Cambridge University Press, 16(4), pp. 501–516. doi: 10.1017/S0954102004002287.

Howard, W.R., and Prell, W. L. (1992). Late Quaternary Surface Circulation of the Southern Indian Ocean and its Relationship to Orbital Variations. Paleoceanography, 7(1), 79–117. https://doi.org/10.1029/91PA02994

Howard, W.R., and Prell, W.L. (1994). Late Quaternary CaCO3 production and preservation in the Southern Ocean: implications for oceanic and atmospheric carbon cycling. Paleoceanography 9, 453e482.

Hurd, D.C. (1973). Interactions of biogenic opal, sediment and seawater in the Central Equatorial Pacific. Geochimica et Cosmochimica Acta, 37(10), 2257, IN1,2267–2266, IN1,2282. https://doi.org/10.1016/0016-7037(73)90103-8

Hutson, W.H. (1980). The Agulhas Current during the Late Pleistocene: Analysis of Modern Faunal Analogs. Science (American Association for the Advancement of Science), 207(4426), 64–66. https://doi.org/10.1126/science.207.4426.64

Intergovernmental Panel on Climate Change (IPCC) (2013). The Physical Science Basis. Contribution of Working Group I to the Fifth Assessment Report of the Intergovernmental Panel on Climate Change, Cambridge University Press, Cambridge, United Kingdom and New York, NY, USA, pp. 1535

Imbrie, J., and Kipp, N.G. (1971). A new micropaleontological method for quantitative paleoclimatology: application to a Late Pleistocene Caribbean core.
K.K. Turekian (Ed.), The Late Cenozoic Glacial Ages, Yale University Press, New Haven, pp. 71-181.

Imbrie, J., Hays, J. D. , Martinson, D. G. , McIntyre, A. , Mix, A. C. , Morley, J. J. , Pisias, N. G. , Prell, W. L. and Shackleton, N. J. (1984): The orbital theory of Pleistocene climate: support from a revised chronology of the marine d18O record , Dordrecht, D. Reidel Publishing Company

Jaccard, S., Hayes, C.T., Martínez-García, A., Hodell, D. A., Anderson, R. F., Sigman, D. M., & Haug, G. H. (2013). Two Modes of Change in Southern Ocean Productivity Over the Past Million Years. Science (American Association for the Advancement of Science), 339, (6126), 1419–1423. https://doi.org/10.1126/science.1227545

Johansen, J.R., and Fryxell, G.A. (1985). The genus Thalassiosira (Bacillariophyceae): studies on species occurring south of the Antarctic Convergence Zone. Deep-Sea Research. Part B. Oceanographic Literature Review, 32(12): 1050. https://doi.org/10.1016/0198-0254(85)94033-6

Jones, J., Kohfeld, K. E., Bostock, H., Crosta, X., Liston, M., Dunbar, G., Chase, Z., Leventer, A., Anderson, H., and Jacobsen, G. (2022). Sea ice changes in the southwest Pacific sector of the Southern Ocean during the last 140 000 years. Climate of the Past, 18(3), 465–483. https://doi.org/10.5194/cp-18-465-2022

Jouzel, J., Masson-Delmotte, V., Fischer, H., Gallet, J. C., Johnsen, S., Leuenberger, M., Loulergue, L., Luethi, D., Oefter, H., Parrenin, F., Raisbeck, G., Raynaud, D., Cattani, O., Schilt, A., Schwander, J., Selmo, E., Souchez, R., Spahni, R., Stauffer, B., & Chappellaz, J. (2007). Orbital and Millennial Antarctic Climate Variability over the Past 800,000 Years. Science (American Association for the Advancement of Science), 317(5839), 793–796. https://doi.org/10.1126/science.1141038

Kashiwase, H., Ohshima, K. I., Nihashi, S., & Eicken, H. (2017). Evidence for ice-ocean albedo feedback in the Arctic Ocean shifting to a seasonal ice zone. Scientific Reports, 7(1), 8170–10. https://doi.org/10.1038/s41598-017-08467-z

Khatiwala, S, Schmittner, A, and Muglia, J. (2019). Air-sea disequilibrium enhances ocean carbon storage during glacial periods. Science Advances, 5(6), eaaw4981–eaaw4981. https://doi.org/10.1126/sciadv.aaw4981

Kohfeld, K.E., and Harrison, S. P. (2001). DIRTMAP: the geological record of dust. Earth-Science Reviews, 54(1), 81–114. https://doi.org/10.1016/S0012-8252(01)00042-3

Kohfeld, K.E., and Ridgwll, A. (2009). Glacial-Interglacial Variability in Atmospheric CO2 – Surface Ocean-Lower Atmospheric Processes (eds C. L. Quéré and E. S. Saltzman), American Geophysical Union, Washington D.C.

Kohfeld, K.E., Le Quere, C., Harrison, S. P., and Anderson, R. F. (2005). Role of marine biology in glacial-interglacial CO2 cycles. Science (American Association for the Advancement of Science), 308(5718), 74–78.

Kohfeld, K.E., Graham, R., de Boer, A., Sime, L., Wolff, E., Le Quéré, C., & Bopp, L. (2013). Southern Hemisphere westerly wind changes during the Last Glacial Maximum: paleo-data synthesis. Quaternary Science Reviews, 68, 76–95. https://doi.org/10.1016/j.quascirev.2013.01.017

Kohfeld, K.E., and Chase, Z. (2017). Temporal evolution of mechanisms controlling ocean carbon uptake during the last glacial cycle. Earth and Planetary Science Letters, 472: 206–215. https://doi.org/10.1016/j.epsl.2017.05.015

Kroopnick, P.M. (1985). The distribution of 13C of ΣCO2 in the world oceans. Deep-Sea Research. Part A. Oceanographic Research Papers, 32(1), 57–84. https://doi.org/10.1016/0198-0149(85)90017-2

Kumar, N., Gwiazda, R., Anderson, R. F., & Froelich, P. N. (1993). 231Pa/230Th ratios in sediments as a proxy for past changes in Southern Ocean productivity. Nature (London), 362(6415), 45–48. https://doi.org/10.1038/362045a0

Kumar, N., Anderson, R. F., Mortlock, R. A., Froelich, P. N., Kubik, P., Dittrich-Hannen, B., & Suter, M. (1995). Increased biological productivity and export production in the glacial Southern Ocean. Nature (London), 378(6558), 675–680. https://doi.org/10.1038/378675a0

Lambert, F., Tagliabue, A., Shaffer, G., Lamy, F., Winckler, G., Farias, L., Gallardo, L., & De Pol-Holz, R. (2015). Dust fluxes and iron fertilization in Holocene and Last Glacial Maximum climates. Geophysical Research Letters, 42(14), 6014–6023. https://doi.org/10.1002/2015GL064250

Lamy, F., Arz, H. W., Kilian, R., Lange, C. B., Lembke-Jene, L., Wengler, M., Kaiser, J., Baeza-Urrea, O., Hall, I. R., Harada, N., & Tiedemann, R. (2015). Glacial reduction and millennial-scale variations in Drake Passage throughflow. Proceedings of the National Academy of Sciences - PNAS, 112(44), 13496–13501. https://doi.org/10.1073/pnas.1509203112

Li, F., Ginoux, P., & Ramaswamy, V. (2008). Distribution, transport, and deposition of mineral dust in the Southern Ocean and Antarctica: Contribution of major sources. Journal of Geophysical Research: Atmospheres, 113(D10), D10207–n/a. https://doi.org/10.1029/2007JD009190

Lisiecki, L.E., and Raymo, M.E., (2005). A Pliocene–Pleistocene stack of 57 globally distributed benthic δ 18 O records. Paleoceanography, 20(1): 1-17. https://doi.org/10.1029/2004PA001071

Lisiecki, L. & Stern, J. V. (2016). Regional and global benthic δ18O stacks for the last glacial cycle. Paleoceanography, 31(10), 1368–1394. https://doi.org/10.1002/2016PA003002

Liston, M. (2018). Master's thesis: Glacial-interglacial productivity in the Polar Frontal Zone, southwest Pacific Ocean. Victoria University of Wellington, Wellington New Zealand.

Locarnini, R.A., Mishonov, A.V., Antonov, J.I., Boyer, T.P., Garcia, H.E., Baranova, O.K., Zweng, M.M., Paver, C.R., Reagan, J.R., Johnson, D.R., Hamilton, M., Seidov, D. (2013). World Ocean atlas 2013, volume 1: Temperature. In: Levitus, S. (Ed.), A. Mishonov Technical. Vol. 73. pp. 40. (NOAA Atlas NESDIS).

Lougheed, B., & Obrochta, S. P. (2016). MatCal: Open Source Bayesian 14C Age Calibration in Matlab. Journal of Open Research Software, 4(1), e42–e42. https://doi.org/10.5334/jors.130

Lougheed, B. C., and Obrochta, S. P. (2019). A Rapid, Deterministic Age-Depth Modeling Routine for Geological Sequences With Inherent Depth Uncertainty. Paleoceanography and Paleoclimatology, 34(1), 122–133. https://doi.org/10.1029/2018PA003457

Lynch-Stieglitz, J., Adkins, J., Curry, W., Dokken, T., Hall, I., Herguera, J., Hirschi, J. J.-M., Ivanova, E., Kissel, C., Marchal, O., Marchitto, T., McCave, I., McManus, J., Mulitza, S., Ninnemann, U., Peeters, F.J., Yu, E.F., & Zahn, R. (2007). Atlantic Meridional Overturning Circulation during the Last Glacial Maximum. Science (American Association for the Advancement of Science), 316,(5821), 66–69. https://doi.org/10.1126/science.1137127

Maksym, T. (2019). Arctic and Antarctic Sea Ice Change: Contrasts, Commonalities, and Causes. Annual Review of Marine Science, 11(1), 187–213. https://doi.org/10.1146/annurev-marine-010816-060610

Mann, D.G., and Droop, S. J. M. (1996). Biodiversity, biogeography and conservation of diatoms. Hydrobiologia (The Hague), 336(1-3), 19–32

Morales Maqueda, M. and Rahmstorf, S. (2002). Did Antarctic sea-ice expansion cause glacial CO2 decline? Geophysical Research Letters, 29(1), 11.1–11.3.

Marchetti, A., & Cassar, N. (2009). Diatom elemental and morphological changes in response to iron limitation: a brief review with potential paleoceanographic

applications. Geobiology, 7(4), 419–431. https://doi.org/10.1111/j.1472-4669.2009.00207.x

MARGO Project Members (2009). Const 2 raints on the magnitude and patterns of ocean cooling at the Last Glacial Maximum. Nature Geoscience, 2, 127-132. https://doi.org/10.1038/ngeo411

Martin, J.H., Gordon, R. M., and Fitzwater, S. E. (1990). Iron in Antarctic waters. Nature (London), 345(6271), 156–158. https://doi.org/10.1038/345156a0

Martínez-García, A., Sigman, D. M., Ren, H., Anderson, R. F., Straub, M., Hodell, D. A., Jaccard, S. L., Eglinton, T. I., & Haug, G. H. (2014). Iron Fertilization of the Subantarctic Ocean During the Last Ice Age. Science (American Association for the Advancement of Science), 343(6177), 1347–1350. https://doi.org/10.1126/science.1246848

Martinson, D., Pisias, N. G., Hays, J. D., Imbrie, J., Moore, T. C., & Shackleton, N. J. (1987). Age dating and the orbital theory of the ice ages: Development of a high-resolution 0 to 300,000-year chronostratigraphy. Quaternary Research, 27(1), 1–29. https://doi.org/10.1016/0033-5894(87)90046-9

Marzocchi, A., & Jansen, M.F. (2019). Global cooling linked to increased glacial carbon storage via changes in Antarctic sea ice. Nature Geoscience, 12(12): 1001–1005. https://doi.org/10.1038/s41561-019-0466-8

Matsumoto, K., Sarmiento, J. L., & Brzezinski, M. A. (2002). Silicic acid leakage from the Southern Ocean: A possible explanation for glacial atmospheric pCO2. Global Biogeochemical Cycles, 16(3), 5–1–5–23. https://doi.org/10.1029/2001GB001442

Matsumoto, K., Chase, Z., & Kohfeld, K. (2014). Different mechanisms of silicic acid leakage and their biogeochemical consequences. Paleoceanography, 29(3), 238–254. https://doi.org/10.1002/2013PA002588

McManus, J., Berelson, W. M., Klinkhammer, G. P., Hammond, D. E., & Holm, C. (2005). Authigenic uranium: Relationship to oxygen penetration depth and organic carbon rain. Geochimica et Cosmochimica Acta, 69(1), 95–108. https://doi.org/10.1016/j.gca.2004.06.023

Milankovitch, M. (1920). Théorie mathématique des phénomenes thermiques produits par la radiation solaire. Paris, Gauthier-Villars.

Mitchell, G.B., Brody, E. A., Holm-Hansen, O., McClain, C., & Bishop, J. (1991). Light Limitation of Phytoplankton Biomass and Macronutrient Utilization in the Southern Ocean. Limnology and Oceanography, 36(8), 1662–1677. https://doi.org/10.4319/lo.1991.36.8.1662

Mix, A.C., Bard, E., & Schneider, R. (2001). Environmental processes of the ice age: land, oceans, glaciers (EPILOG). Quaternary Science Reviews, 20(4), 627–657. https://doi.org/10.1016/S0277-3791(00)00145-1

Morales Maqueda, M.A., and Rahmstorf, S. (2002). Did Antarctic sea-ice expansion cause glacial CO2 decline? Geophysical Research Letters, 29(1), 1011–11–3. https://doi.org/10.1029/2001GL013240

Morée, A.L., Schwinger, J., & Heinze, C. (2018). Southern Ocean controls of the vertical marine δ13C gradient – a modelling study. Biogeosciences, 15(23), 7205–7223. https://doi.org/10.5194/bg-15-7205-2018

Mortlock, R.A., and Froelich, P. N. (1989). A simple method for the rapid determination of biogenic opal in pelagic marine sediments. Deep-Sea Research. Part A. Oceanographic Research Papers, 36(9), 1415–1426. https://doi.org/10.1016/0198-0149(89)90092-7

Mortlock, R.A., Charles, C. D., Froelich, P. N., Zibello, M. A., Saltzman, J., Hays, J. D., & Burckle, L. H. (1991). Evidence for lower productivity in the Antarctic Ocean during the last glaciation. Nature (London), 351(6323), 220–223. https://doi.org/10.1038/351220a0

Nair, A., Mohan, R., Crosta, X., Manoj, M., Thamban, M., & Marieu, V. (2019). Southern Ocean sea ice and frontal changes during the Late Quaternary and their linkages to Asian summer monsoon. Quaternary Science Reviews, 213, 93–104. https://doi.org/10.1016/j.quascirev.2019.04.007

Neff, P., and Bertler, N. A. N. (2015). Trajectory modeling of modern dust transport to the Southern Ocean and Antarctica. Journal of Geophysical Research. Atmospheres, 120(18), 9303–9322. https://doi.org/10.1002/2015JD023304

Neftel, A., Oeschger, H., Schwander, J., Stauffer, B., & Zumbrunn, R. (1982). Ice core sample measurements give atmospheric CO2 content during the past 40,000 yr. Nature (London), 295(5846), 220–223. https://doi.org/10.1038/295220a0

Nelson, S.T. (2000). A simple, practical methodology for routine VSMOW/SLAP normalization of water samples analyzed by continuous flow methods. Rapid Communications in Mass Spectrometry, 14(12), 1044–1046. https://doi.org/10.1002/1097-0231(20000630)14:12<1044::AID-RCM987>3.0.CO;2-3

Ohno, M., Hayashi, T., Sato, M., Kuwahara, Y., Mizuta, A., Kita, I., Sato, T., & Kano, A. (2016). Millennial-Scale Interaction between Ice Sheets and Ocean Circulation during Marine Isotope Stage 100. Frontiers in Earth Science (Lausanne), 4. https://doi.org/10.3389/feart.2016.00055

Oliver, K. I. C., Hoogakker, B. A. A., Crowhurst, S., Henderson, G. M., Rickaby, R. E. M., Edwards, N. R., and Elderfield, H. (2009). A synthesis of marine sediment core δ 13 C data over the last 150 000 years. Climate of the Past Discussions, 5(6): 2497–2554. https://doi.org/10.5194/cpd-5-2497-2009

O'Neill, C.M., Hogg, A.M., Ellwood, M.J., Opdyke, B.N., & Eggins, S.M. (2021). Sequential changes in ocean circulation and biological export productivity during the last glacial–interglacial cycle: a model–data study. Climate of the Past, 17(1), 171–201. https://doi.org/10.5194/cp-17-171-2021

Pahnke, K., Zahn, R., Elderfield, H., and Schulz, M. (2003), 340,000-year centennial-scale marine record of Southern Hemisphere climatic oscillation, Science, 301: 948–952.

Pahnke, K., and Zahn, R. (2005). Southern Hemisphere Water Mass Conversion Linked with North Atlantic Climate Variability. Science (American Association for the Advancement of Science), 307(5716): 1741–1746. https://doi.org/10.1126/science.1102163

Panassa, E., Santana-Casiano, J. M., González-Dávila, M., Hoppema, M., van Heuven, S. M. A. ., Völker, C., Wolf-Gladrow, D., & Hauck, J. (2018). Variability of nutrients and carbon dioxide in the Antarctic Intermediate Water between 1990 and 2014. Ocean Dynamics, 68(3), 295–308. https://doi.org/10.1007/s10236-018-1131-2

Parkinson, C. and Cavalieri, D. J. (2012). Antarctic sea ice variability and trends, 1979–2010. The Cryosphere, 6(4), 871–880. https://doi.org/10.5194/tc-6-871-2012

Parkinson, C. (2019). A 40-y record reveals gradual Antarctic sea ice increases followed by decreases at rates far exceeding the rates seen in the Arctic. Proceedings of the National Academy of Sciences - PNAS, 116(29), 14414–14423. https://doi.org/10.1073/pnas.1906556116

Paterne, M., Michel, E., and Héros, V. (2019). Variability of marine 14C reservoir ages in the Southern Ocean highlighting circulation changes between 1910 and 1950. Earth and Planetary Science Letters, 511, 99–104. https://doi.org/10.1016/j.epsl.2019.01.029f

Pellichero, V., Sallée, J., Schmidtko, S., Roquet, F., & Charrassin, J. (2017). The ocean mixed layer under Southern Ocean sea-ice: Seasonal cycle and forcing. Journal of Geophysical Research. Oceans, 122(2), 1608–1633. https://doi.org/10.1002/2016JC011970

Pellichero, V., Sallée, J., Schmidtko, S., Roquet, F., & Charrassin, J. (2017). The ocean mixed layer under Southern Ocean sea-ice: Seasonal cycle and forcing. Journal of Geophysical Research. Oceans, 122(2), 1608–1633. https://doi.org/10.1002/2016JC011970

Pellichero, V., Sallée, J.B., Chapman, C., and Downes, S. (2018). The Southern Ocean meridional overturning in the sea-ice sector is driven by freshwater fluxes. Nature Communications, 9(1), 1789–9. https://doi.org/10.1038/s41467-018-04101-2

Person, R., Vancoppenolle, M., & Aumont, O. (2020). Iron Incorporation From Seawater Into Antarctic Sea Ice: A Model Study. Global Biogeochemical Cycles, 34(11), e2020GB006665–n/a. https://doi.org/10.1029/2020GB006665

Petit, J., Jouzel, J., Raynaud, D., Barkov, N. I., Barnola, J.-M., Basile, I., Bender, M., Chappellaz, J., Davis, M., Delaygue, G., Delmotte, M., Kotlyakov, V. M., Legrand, M., Lipenkov, V. Y., Lorius, C., PÉpin, L., Ritz, C., Saltzman, E., & Stievenard, M. (1999). Climate and atmospheric history of the past 420,000 years from the Vostok ice core, Antarctica. Nature (London), 399(6735), 429–436. https://doi.org/10.1038/20859

Petrich, C., and Eicken, H. (2017). Overview of sea ice growth and properties. In: Sea Ice, Third Edition, Thomas, D.N. (Ed.), Wiley-Blackwell, Oxford, UK.

Pichon, J.J., Bareille, G., Labracherie, M., Labeyrie, L.D., Baudrimont, A. & Turon, J.L. (1992). Quantification of the Biogenic Silica Dissolution in Southern Ocean Sediments. Quaternary Research, 37(3), 361–378. https://doi.org/10.1016/0033-5894(92)90073-R

Pollard, T.R., Lucas, M., & Read, J. (2002). Physical controls on biogeochemical zonation in the Southern Ocean. Deep-Sea Research. Part II, Topical Studies in Oceanography, 49(16), 3289–3305. https://doi.org/10.1016/S0967-0645(02)00084-X

Prebble, J. G., Bostock, H. C., Cortese, G., Lorrey, A. M., Hayward, B. W., Calvo, E., Northcote, L. C., Scott, G. H., and Neil, H. L. (2017). Evidence for a Holocene Climatic Optimum in the southwest Pacific: A multiproxy study. Paleoceanography, 32(8), 763–779. https://doi.org/10.1002/2016PA003065

Prell, W. (1985). The stability of low-latitude sea-surface temperatures: an evaluation of CLIMAP reconstruction with emphasis on the positive SST anomalies. Rep. TR 025, 1-60, U.S. Dep. Of Energy, Washington, D.C.

Ragueneau, O., Tréguer, P., Leynaert, A., Anderson, R.F., Brzezinski, M.A., DeMaster, D.J., Dugdale, R.C., Dymond, J., Fischer, G., François, R., Heinze, C., Maier-Reimer, E., Martin-Jézéquel, V., Nelson, D.M., & Quéguiner, B. (2000). A review of the Si cycle in the modern ocean: recent progress and missing gaps in the application of biogenic opal as a paleoproductivity proxy. Global and Planetary Change, 26(4), 317–365. https://doi.org/10.1016/S0921-8181(00)00052-7

Reimer, R. (2021). Evolution of Radiocarbon Calibartion. Radiocarbon, 1–17. https://doi.org/10.1017/RDC.2021.62

Renberg, I. (1990). A procedure for preparing large sets of diatom slides from sediment cores. Journal of Paleolimnology, 4(1): 87-90. https://doi.org/10.1007/bf00208301

Resende, P. Azeiteiro, U., & Pereira, M. J. (2005). Diatom ecological preferences in a shallow temperate estuary (Ria de Aveiro, Western Portugal). Hydrobiologia, 544(1), 77–88. https://doi.org/10.1007/s10750-004-8335-9

Reynolds, R., Rayner, N., Smith, T., Stokes, D., and Wang, W. (2002). An Improved In Situ and Satellite SST Analysis for Climate. Journal of Climate, 15(13), 1609–1625. https://doi.org/10.1175/1520-0442(2002)015<1609:AIISAS>2.0.CO;2

Reynolds, R., Smith, T., Chunying, L., Chelton, D., Casey, K., & Schlax, M. (2007). Daily High-Resolution-Blended Analyses for Sea Surface Temperature. Journal of Climate, 20(22), 5473–5496. https://doi.org/10.1175/2007JCLI1824.1

Rintoul, S.R., & Bullister, J. L. (1999). A late winter hydrographic section from Tasmania to Antarctica. Deep-Sea Research. Part I, Oceanographic Research Papers, 46(8), 1417–1454. https://doi.org/10.1016/S0967-0637(99)00013-8

Roach, L.A., Dörr, J., Holmes, C. R., Massonnet, F., Blockley, E. W., Notz, D., Rackow, T., Raphael, M. N., O'Farrell, S. P., Bailey, D. A., & Bitz, C. M. (2020). Antarctic Sea Ice Area in CMIP6. Geophysical Research Letters, 47(9), e2019GL086729. https://doi.org/10.1029/2019GL086729

Ronge, T.A., Steph, S., Tiedemann, R., Prange, M., Merkel, U., Nürnberg, D., and Kuhn, G. (2015). Pushing the boundaries: Glacial/interglacial variability of intermediate and deep waters in the southwest Pacific over the last 350,000 years. Paleoceanography, 30(2): 23–38. https://doi.org/10.1002/2014pa002727

Röthlisberger, Bigler, M., Wolff, E. W., Joos, F., Monnin, E., & Hutterli, M. A. (2004). Ice core evidence for the extent of past atmospheric CO2 change due to iron fertilisation. Geophysical Research Letters, 31(16), L16207–n/a. https://doi.org/10.1029/2004GL020338

Rutgers van der Loeff, M.M., Cassar, N., Nicolaus, M., Rabe, B., and Stimac, I. (2014). The influence of sea ice cover on air-sea gas exchange estimated with radon-222 profiles. Journal of Geophysical Research, Oceans, 119(5): 2735–2751. https://doi.org/10.1002/2013jc009321

Rysgaard, S., Bendtsen, J., Delille, B., Dieckmann, G. S., Glud, R. N., Kennedy, H., Mortensen, J., Papadimitriou, S., Thomas, D. N., & Tison, J.-L. (2011). Sea ice contribution to the air-sea CO2 exchange in the Arctic and Southern Oceans. Tellus. Series B, Chemical and Physical Meteorology, 63(5), 823–830. https://doi.org/10.1111/j.1600-0889.2011.00571.x

Sachs, H.M. (1973) Quantitative radiolarian-based Paleo-Oceanography in the Late Pliestocene Subarctic Pacific Sediments. Ph.D. Thesis, Brown University [full ref in 1977 paper]

Sachs, H.M., Webb, T., & Clark, D. R. (1977). Paleoecological Transfer Functions. Annual Review of Earth and Planetary Sciences, 5(1), 159–178. https://doi.org/10.1146/annurev.ea.05.050177.001111

Sayles, F.L., Martin, W. ., Chase, Z., & Anderson, R. (2001). Benthic remineralization and burial of biogenic SiO2, CaCO3, organic carbon, and detrital material in the Southern Ocean along a transect at 170° West. Deep-Sea Research. Part II, Topical Studies in Oceanography, 48(19-20), 4323–4383. https://doi.org/10.1016/S0967-0645(01)00091-1

Schlitzer, R. (2005). Interactive analysis and vizualization of geoscience data with Ocean Data View. Computers and Geoscience, 28: 1211–1218. https://doi.org/10.1016/S0098-3004(02)00040-7

Schmiedl, G., & Mackensen, A. (2006). Multispecies stable isotopes of benthic foraminifers reveal past changes of organic matter decomposition and deepwater oxygenation in the Arabian Sea. Paleoceanography, 21(4). https://doi.org/10.1029/2006PA001284

Schneider Mor, A., Yam, R., Bianchi, C., Kunz-Pirrung, M., Gersonde, R., & Shemesh, A. (2012). Variable sequence of events during the past seven terminations in two deep-sea cores from the Southern Ocean. Quaternary Research, 77(2), 317–325. https://doi.org/10.1016/j.yqres.2011.11.006

Schultz, C., Doney, S. C., Zhang, W. G., Regan, H., Holland, P., Meredith, M. P., & Stammerjohn, S. (2020). Modeling of the Influence of Sea Ice Cycle and Langmuir Circulation on the Upper Ocean Mixed Layer Depth and Freshwater Distribution at the West Antarctic Peninsula. Journal of Geophysical Research. Oceans, 125(8), n/a–n/a. https://doi.org/10.1029/2020JC016109

Sedwick, P.E., & DiTullio, G. R. (1997). Regulation of algal blooms in Antarctic Shelf Waters by the release of iron from melting sea ice. Geophysical Research Letters, 24(20), 2515–2518. https://doi.org/10.1029/97GL02596

Serôdio, J., & Lavaud, J. Diatoms and Their Ecological Importance. Life Below Water, Encyclopedia of the UN Sustainable Development Goals, pp.1-9, 2020, ff10.1007/978-3-319-71064-8_12-1ff. ffhal-03113866f

Shackleton, N. (1967). Oxygen Isotope Analyses and Pleistocene Temperatures Reassessed. Nature (London), 215(5096), 15–17. https://doi.org/10.1038/215015a0

Shackleton, N., & Opdyke, N. (1973). Oxygen Isotope and Palaeomagnetic Stratigraphy of Equatorial Pacific Core V28-238: Oxygen Isotope Temperatures and Ice Volumes on a 105 Year and 106 Year Scale. Quaternary Research, 3(1), 39-55. doi:10.1016/0033-5894(73)90052-5

Shin, S.I., Liu, Z., Otto-Bliesner, B., Kutzbach, J., & Vavrus, Stephen J. (2003). Southern Ocean sea-ice control of the glacial North Atlantic thermohaline circulation. Geophysical Research Letters, 30(2), 1096–n/a. https://doi.org/10.1029/2002GL015513

Shoenfelt, E., Winckler, G., Lamy, F., Anderson, R. F., & Bostick, B. C. (2018). Highly bioavailable dust-borne iron delivered to the Southern Ocean during glacial periods. *Proceedings of the National Academy of Sciences - PNAS*, *115*(44), 11180–11185. https://doi.org/10.1073/pnas.1809755115

Sigman, D., and Boyle, E. (2000) Glacial/Interglacial variations in atmospheric carbon dioxide. Nature (London), 407(6806): 859-869. https://doi.org/10.1038/35038000

Sigman, D.E., Nelson, D. M., & Brzezinski, M. A. (2002). The Si cycle in the Pacific sector of the Southern Ocean: seasonal diatom production in the surface layer and export to the deep sea. Deep-Sea Research. Part II, Topical Studies in Oceanography, 49(9), 1747–1763. https://doi.org/10.1016/S0967-0645(02)00010-3

Sigman, Hain, M. P., & Haug, G. H. (2010). The polar ocean and glacial cycles in atmospheric CO(2) concentration. Nature (London), 466(7302), 47. https://doi.org/10.1038/nature09149

Sigman, D.E., Fripiat, F., Studer, A. S., Kemeny, P. C., Martínez-García, A., Hain, M. P., Ai, X., Wang, X., Ren, H., & Haug, G. H. (2021). The Southern Ocean during the ice ages: A review of the Antarctic surface isolation hypothesis, with comparison to the

North Pacific. Quaternary Science Reviews, 254, 106732. https://doi.org/10.1016/j.quascirev.2020.106732

Skinner, L., & Shackleton, N. (2005). An Atlantic lead over Pacific deep-water change across Termination I: implications for the application of the marine isotope stage stratigraphy. Quaternary Science Reviews, 24(5), 571–580. https://doi.org/10.1016/j.quascirev.2004.11.008

Smith, N.O., & Nelson, D. M. (1985). Phytoplankton Bloom Produced by a Receding Ice Edge in the Ross Sea: Spatial Coherence with the Density Field. Science (American Association for the Advancement of Science), 227(4683), 163–166. https://doi.org/10.1126/science.227.4683.163

Smith, R. O., Vennell, R., Bostock, H. C., & Williams, M. J. (2013). Interaction of the subtropical front with topography around southern New Zealand. Deep-Sea Research. Part I, Oceanographic Research Papers, 76, 13–26. https://doi.org/10.1016/j.dsr.2013.02.007

Smol J.P., & Stoermer EF. (2010) The Diatoms: Applications for the Environmental and Earth Sciences. New York: Cambridge University Press. https://doi.org/10.1017/CBO9780511763175

Snoeijs, P., Busse, S., & Potapova, M. (2002). The Importanc of Diatom Cell Size in Community Analysis, Journal of Phycology, 38(2), 265–281. https://doi.org/10.1046/j.1529-8817.2002.01105.x

Sokolov, & Rintoul, S. R. (2002). Structure of Southern Ocean fronts at 140°E. Journal of Marine Systems, 37(1), 151–184. https://doi.org/10.1016/S0924-7963(02)00200-2

Sokolov, S., & Rintoul, S. (2009). Circumpolar structure and distribution of the Antarctic Circumpolar Current fronts: 2. Variability and relationship to sea surface height. Journal of Geophysical Research: Oceans, 114(C11), n/a–n/a. https://doi.org/10.1029/2008JC005248

Stein, K., Timmermann, A., Kwon, E.Y., and Friedrich, T. (2020). Timing and magnitude of Southern Ocean sea ice/carbon cycle feedbacks. Proceedings of the National Academy of Sciences, 117(9): 4498–4504. https://doi.org/10.1073/pnas.1908670117

Stenni, B., Masson-Delmotte, V., Selmo, E., Oerter, H., Meyer, H., Röthlisberger, R., Jouzel, J., Cattani, O., Falourd, S., Fischer, H., Hoffmann, G., Iacumin, P., Johnsen, S. ., Minster, B., & Udisti, R. (2010). The deuterium excess records of EPICA Dome C and Dronning Maud Land ice cores (East Antarctica). Quaternary Science Reviews, 29(1), 146–159. https://doi.org/10.1016/j.quascirev.2009.10.009

Stephens, B.B., and Keeling, R.F. (2000). The influence of Antarctic sea ice on glacial–interglacial CO2 variations. Nature (London), 404(6774): 171–174. https://doi.org/10.1038/35004556

Stern, J. & Lisiecki, L. E. (2013). North Atlantic circulation and reservoir age changes over the past 41,000 years. Geophysical Research Letters, 40(14), 3693–3697. https://doi.org/10.1002/grl.50679

Studer, A. S., Sigman, D.M., Martínez-García, A., Benz, V., Winckler, G., Kuhn, G., Esper, O., Lamy, F., Jaccard, S.L., Wacker, L., Oleynik, S., Gersonde, R., and Haug, G.H. (2015). Antarctic Zone nutrient conditions during the last two glacial cycles. Paleoceanography, 30(7): 845–862. https://doi.org/10.1002/2014PA002745

Stuiver, M., & Braziunas, T. F. (1993). Modeling Atmospheric 14C Influences and 14C Ages of Marine Samples to 10,000 BC. Radiocarbon, 35(1), 137–189. https://doi.org/10.1017/S0033822200013874

Stukel, M.R., & Ducklow, H. W. (2017). Stirring Up the Biological Pump: Vertical Mixing and Carbon Export in the Southern Ocean. Global Biogeochemical Cycles, 31(9), 1420–1434. https://doi.org/10.1002/2017GB005652

Sturm, A. (2003) Dissertation: Changes in ocean circulation and carbonate chemistry in the Australian sector of the Southern Ocean during the last 500,000 years. Available at: http://oceanrep.geomar.de/1614/1/641_Sturm_2004_ChangesInOceanCirculationAnd_92 Hschri_pubid5837.pdf (Accessed: 2 March 2018).

Sun, X., and Matsumoto, K. (2010). Effects of sea ice on atmospheric pCO2: A revised view and implications for glacial and future climates. Journal of Geophysical Research: Biogeosciences, 115(G2), n/a–n/a. https://doi.org/10.1029/2009JG001023

Takeda, A.(1998). Influence of iron availability on nutrient consumption ratio of diatoms in oceanic waters. Nature (London), 393(6687), 774–777. https://doi.org/10.1038/31674

Taylor, R.E. (2000). Fifty Years of Radiocarbon Dating: This widely applied technique has made major strides since its introduction a half-century ago at the University of Chicago. American Scientist, 88(1), 60–67.

Thiagarajan, N., & McManus, J. F. (2019). Productivity and sediment focusing in the Eastern Equatorial Pacific during the last 30,000 years. Deep-Sea Research. Part I, Oceanographic Research Papers, 147, 100–110. https://doi.org/10.1016/j.dsr.2019.03.007

Tschumi, T., Joos, F., Gehlen, M., & Heinze, C. (2011). Deep ocean ventilation, carbon isotopes, marine sedimentation and the deglacial CO2 rise. Climate of the Past, 7(3), 771–800. https://doi.org/10.5194/cp-7-771-2011

Toggweiler, J. R. (1999). Variation of atmospheric CO2 by ventilation of the ocean's deepest water. Paleoceanography, 14(5): 571–588. https://doi.org/10.1029/1999PA900033

Toggweiler, J.R., Russell, J. L., & Carson, S. R. (2006). Midlatitude westerlies, atmospheric CO2, and climate change during the ice ages. Paleoceanography, 21(2), PA2005–n/a. https://doi.org/10.1029/2005PA001154

Urey, H.C. (1947). The thermodynamic properties of isotopic substances. Journal of the Chemical Society, 562–581. https://doi.org/10.1039/jr9470000562

Van Cappellen, P. & Qiu, L. (1997). Biogenic silica dissolution in sediments of the Southern Ocean. I. Solubility. Deep-Sea Research. Part II, Topical Studies in Oceanography, 44(5), 1109–1128. https://doi.org/10.1016/S0967-0645(96)00113-0

Varkouhi, S., & Wells, J. (2020). The relation between temperature and silica benthic exchange rates and implications for near-seabed formation of diagenetic opal. Results in Geophysical Sciences, 1-4, 100002. https://doi.org/10.1016/j.ringps.2020.100002

Wang, S., Bailey, D., Lindsay, K., Moore, J. K., & Holland, M. (2014). Impact of sea ice on the marine iron cycle and phytoplankton productivity. Biogeosciences, 11(17), 4713–4731. https://doi.org/10.5194/bg-11-4713-2014

Warnock, J., Scherer, R., & Loubere, P. (2007). A quantitative assessment of diatom dissolution and late quaternary primary productivity in the Eastern Equatorial Pacific. Deep-Sea Research. Part II, Topical Studies in Oceanography, 54(5), 772–783. https://doi.org/10.1016/j.dsr2.2007.01.011

Warnock, J.P., and Scherer, R.P. (2015a). A revised method for determining the absolute abundance of diatoms. Journal of Paleolimnology, 53(1): 157–163. https://doi.org/10.1007/s10933-014-9808-0

Warnock, & Scherer, R. P. (2015b). Diatom species abundance and morphologically-based dissolution proxies in coastal Southern Ocean assemblages. Continental Shelf Research, 102, 1–8. https://doi.org/10.1016/j.csr.2015.04.012

Weaver, A. J., Eby, M., Fanning, A. F., and Wiebe, E. C., 1998, Simulated influence of carbon dioxide, orbital forcing and ice sheets on the climate of the Last Glacial Maximum: Nature, v. 394, p. 847-853.

Westacott, S., Planavsky, N. J., Zhao, M.-Y., & Hull, P. M. (2021). Revisiting the sedimentary record of the rise of diatoms. Proceedings of the National Academy of Sciences - PNAS, 118(27), 1. https://doi.org/10.1073/pnas.2103517118

Wilks, J. V., and Armand, L. K. (2017). Diversity and taxonomic identification of Shionodiscus spp. in the Australian sector of the Subantarctic Zone. Diatom Research, 32(3): 295–307. https://doi.org/10.1080/0269249X.2017.1365015

Williams, M. J. (2013). Voyage Report TAN1302, Mertz Polynya (Tech. Rep.). Wellington: National Institute of Water and Atmospheric Research (NIWA).

Williams, T.J., Martin, E.E., Sikes, E., Starr, A., Umling, N.E., and Glaubke, R. (2021). Neodymium isotope evidence for coupled Southern Ocean circulation and Antarctic climate throughout the last 118,000 years. Quaternary Science Reviews, 260, 106915. https://doi.org/10.1016/j.quascirev.2021.106915

Willis, E.H., Tauber, H., & Munnich, K.O. (1960). Variations in the atmospheric radiocarbon concentration over the past 1300 years. American Journal of Science Radiocarbon Supplement 2:1–4

Wilson, D.J., Piotrowski, A.M., Galy, A., and Banakar, V.K. (2015). Interhemispheric controls on deep ocean circulation and carbon chemistry during the last two glacial cycles. Paleoceanography, 30: 621–641.

Wittmann, A. (2010). Life in cold oceans: activity dependent on extracellular ion regulation?. http://elib.suub.uni-bremen.de/edocs/00101851-1.pdf.

Wolff, E.W., Barbante, C., Becagli, S., Bigler, M., Boutron, C.F., Castellano, E., de Angelis, M., Federer, U., Fischer, H., Fundel, F., Hansson, M., Hutterli, M., Jonsell, U., Karlin, T., Kaufmann, P., Lambert, F., Littot, G.C., Mulvaney, R., Röthlisberger, R., and Wegner, A. (2010). Changes in environment over the last 800,000 years from chemical analysis of the EPICA Dome C ice core. Quaternary Science Reviews, 29(1), 285–295. https://doi.org/10.1016/j.quascirev.2009.06.013

Wu, Y., Roberts, A. P., Grant, K. M., Heslop, D., Pillans, B. J., Zhao, X., Rohling, E. J., Ronge, T. A., Ma, M., Hesse, P. P., & Palmer, A. S. (2021). Climatically Modulated Dust Inputs from New Zealand to the Southwest Pacific Sector of the Southern Ocean Over the Last 410 kyr. Paleoceanography and Paleoclimatology, 36(5), n/a–n/a. https://doi.org/10.1029/2020PA003949

Zielinski, U., Bianchi, C., Gersonde, R., & Kunz-Pirrung, M. (2002). Last occurrence datums of the diatoms Rouxia leventerae and Rouxia constricta: indicators for marine isotope stages 6 and 8 in Southern Ocean sediments. Marine Micropaleontology, 46(1), 127–137. https://doi.org/10.1016/S0377-8398(02)00042-7

Appendix A.

Age Model & Sampling Depths

Table 4: Radiocarbon dates taken from TAN1302-96. NDFB = Not Distinguishable from Background (>57,5000 years).

Lab Code	Sample Material	Core Name	Depth (cm)	δ13 C (per mil)	δ13 C (+/-)	% Modern Carbon	1σ error	Fraction Modern	(+/-)	Radiocarbon Year	1σ error	Reference
NZA 57105	*N. pachyderma* and *G. bulloides*	TAN13 02-96	21	1	0.2	/	/	0.5982	0.0018	4127	24	Prebble et al., 2017
NZA 57109	*N. pachyderma* and *G. bulloides*	TAN13 02-96	50	0.7	0.2	/	/	0.3723	0.0015	7936	32	Prebble et al., 2017
OZX 517	*N. pachyderma* and *G. bulloides*	TAN13 02-96	63	1	0.1	30.62	0.15	/	/	9505	40	*This study*
NZA 61429	*N. pachyderma* and *G. bulloides*	TAN13 02-96	75	0.7	0.2	/	/	0.2373	0.0011	11554	37	Prebble et al., 2017
OZX 518	*N. pachyderma* and *G. bulloides*	TAN13 02-96	87	-0.1	0.1	19.62	0.11	/	/	13085	45	*This study*
OZX 519	*N. pachyderma* and *G. bulloides*	TAN13 02-96	130	1.7	0.1	0.02	0.04	/	/	NDFB	/	*This study*
OZX 520	*N. pachyderma* and *G. bulloides*	TAN13 02-96	170	-1.1	0.3	0.03	0.04	/	/	NDFB	/	*This study*

Table 5: *Tie points used in construction of the TAN1302-96 age model*

TAN1302-96 Depth (cm)	TAN1302-96 $\delta^{18}O$ (‰)	LR04 Age (ka)	LR04 $\delta^{18}O$ (‰)
110	4.71	18000	5.02
170	3.93	56000	4.35
200	3.782	70000	4.32
220	3.07	82000	3.8
230	3.23	87000	4.18
250	3.22	109000	4.12
270	2.9	123000	3.1
300	3.66	129000	3.9
320	4.35	140000	4.98

Table 6: *Sample depth and corresponding age. Diatom slides using Method 1 used sediment samples that are even (e.g., 10, 20, 30, etc.), while diatom slides using Method 2 used sediment samples that are odd (e.g., 53, 87, etc.). * Indicates the sample was calculated based on linear sedimentation rates.*

Sample Depth (cm)	Age (yr)	Sample Depth (cm)	Age (yr)	Sample Depth (cm)	Age (yr)	Sample Depth (cm)	Age (yr)
10	1001	100	16011	197	68608	260	116007
20	2531	103	16609	200	69999	263	118110

30	4061	107	17406	203	71790	267	120912
40	5591	110	18000	207	74196	270	123000
50	7152	113	19893	210	76000	273	123597
53	7584	117	22434	213	77802	277	124398
57	8108	120	24340	217	80207	280	124998
60	8486	123	26244	220	82000	283	125598
63	8890	127	28780	223	83491	287	126398
67	9735	130	30686	227	85503	290	126999
70	10404	140	37035	230	87000	293	127600
73	11056	150	43357	233	90289	297	128403
77	11844	160	49677	237	94703	300	129000
80	12306	170	56000	240	98011	303	130644
83	12747	180	60672	243	101314	307	132850
87	13361	183	62074	247	105715	310	134503
90	13963	187	63942	250	108999	313	136155
93	14581	190	65340	253	111094	317	138360
97	15404	193	66740	257	113903	320	140000

Appendix B.

Supporting Information

Table 7: *Information for all cores used in calculating southwestern Pacific sector SST gradients (Figure 14).*

Core Name	Latitude	Longitude	Depth (m)	Age Model Reference	Data Used	Data Source
TAN1302-96	59.09°S	157.05°E	3099	*This study*	n/a	*This study*
SO136-111	56.66°S	160.23°E	3912	Crosta et al., 2004	WSIC; SST	Crosta et al., 2004; *This study*
SO136-GC3	42.3°S	169.88°E	958	Pelejero et al., 2006; Barrows et al., 2007	δ13C; SST	Pelejero et al., 2006; Ronge et al., 2015
FR1/94-GC3	44.25°S	149.98°E	2667	Pelejero et al., 2006	SST	Pelejero et al., 2006
ODP 1119-181	44.75°S	172.39°E	396	Wilson et al., 2005	SST	Wilson et al., 2005; Hayward et al., 2008
DSDP 594	45.54°S	174.94°E	1204	Nelson et al., 1985; Kowalski & Meyers 1997	SST	Schaefer et al., 2005
Q200	45.99°S	172.02°E	1370	Waver et al., 1998	SST	Weaver et al., 1998

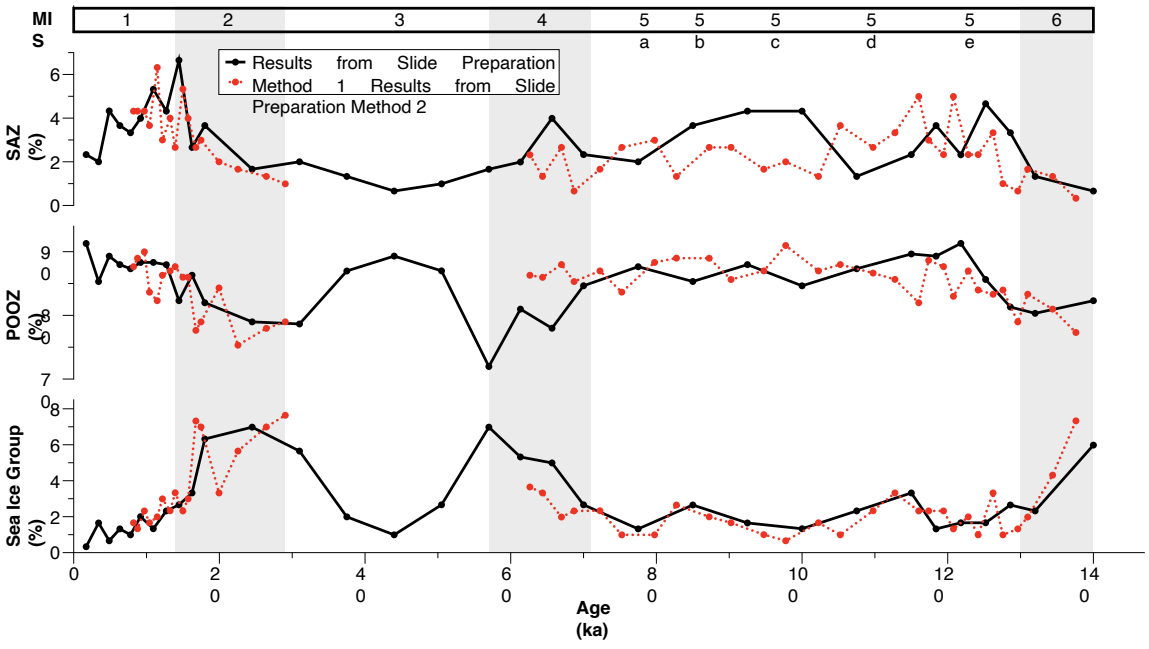

Figure 22: *Results from diatom slide preparation methods 1 & 2. No notable differences or biases were observed between the two different methods.*

Appendix C.

TAN1302-96 and E27-23 Comparison

Potential Causes for WSIC Estimate Differences

The first potential cause for the observed differences between TAN1302-96 and E27-23 WSIC estimates is through the cumulative effects of different laboratory protocols. While it is difficult to determine precisely how much different laboratory protocols could influence the results, we cannot exclude this explanation as a possible contributor to differences in WSIC.

The second potential cause for differences in WSIC estimates between E27-23 and TAN1302-96 are differences in counting and identification methods. We believe this is an unlikely cause for the differences observed between E27-23 and TAN1302-96 primarily because of the magnitude of counting discrepancies required to cause a difference of 50% wSIC estimates between the two cores. The close coupling of wSIC estimates between TAN1302-96 and SO136-111 over the entire glacial-interglacial cycle supports that a fundamental issue relating to taxonomic identification and/or methodology is an unlikely explanation for the observed wSIC differences.

Finally, the fourth potential cause of differing wSIC estimates is selective diatom preservation (e.g., Pichon et al., 1999; Ragueneau et al., 2000). The similarities between TAN1302-96 and SO136-111 wSIC estimates, along with independent indicators in cores E27-23 and TAN1302-96, suggest that this is unlikely. For E27-23, Bradtmiller et al. (2009) used the consistent relationship between $^{231}Pa/^{230}Th$ ratios and opal fluxes to suggest that dissolution remained relatively constant between the LGM and Holocene periods. In TAN1302-96, we assigned a semi-quantitative diatom preservation value between 1 (extreme dissolution) and 4 (virtually perfect preservation) for each counted specimen. The average preservation of diatoms for the entire core was 3.38 ± 0.13, with no observed bias based on sedimentation rate or MIS. This assessment, although semi-qualitative, suggests that preservation remained relatively constant (and good) throughout TAN1302-96, and is therefore unlikely to cause large differences in wSIC between the two cores.

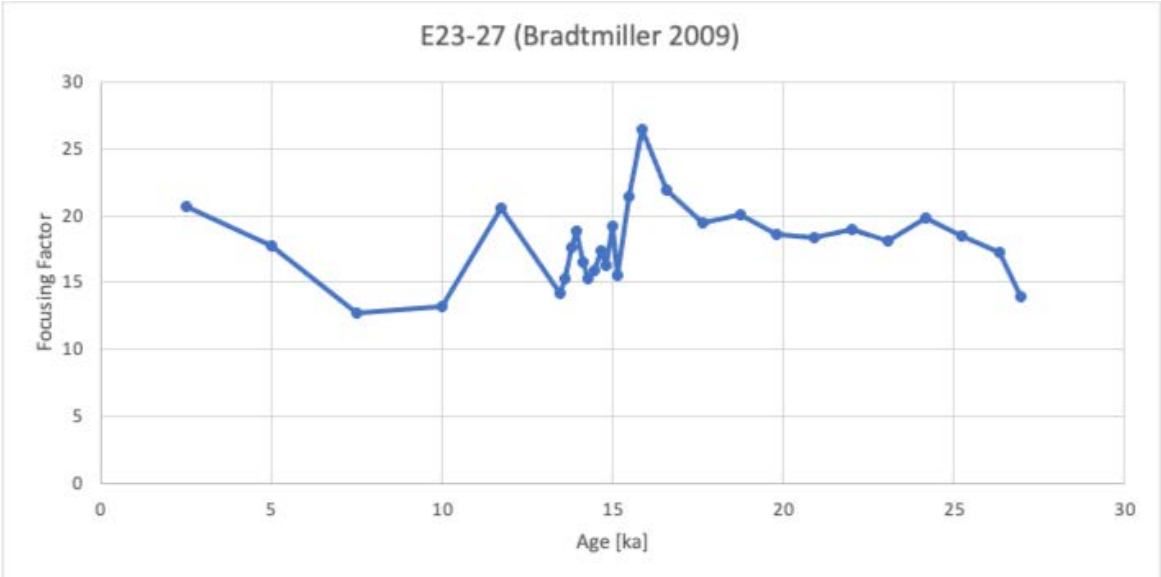

***Figure 23**: Preliminary focusing factor (FF) values for E27-23. These results suggest notable lateral sediment redistribution over the last 26 ka, requiring further analysis (Bradtmiller et al., 2009). FF refers to the degree of sediment focusing (or winnowing), where FF = 1 suggests no postdepositional redistribution of sediments, FF = >1 suggests lateral input of sediments, and FF = <1 suggests lateral removal of sediments (Francois et al., 2004).*

Appendix D.

%AAIW Calculation

The calculation of %AAIW in this study is the same as was used in Ronge et al. (2015):

$$\%AAIW = (\delta^{13}C_{MD97\text{-}2120} - \delta^{13}C_{MD06\text{-}2986}) / (\delta^{13}C_{MD06\text{-}2990} - \delta^{13}C_{MD06\text{-}2986}) * 100$$

All core information for MD97-2120, MD06-2986, and MD06-2990, along with supporting supplemental information can be found through the original publication.

***Table 8**: Calculated %AAIW by age using marine cores MD06-2990, MD06-2986, and MD97-2120.*

Age (ka)	%AAIW	Age (ka)	%AAIW	Age (ka)	%AAIW	Age (ka)	%AAIW
2.87	63.1	30.81	46.2	63.85	47.6	103.08	39.3
3.83	53.4	31.33	44.2	64.36	55.1	103.49	62.6
4.44	61.3	31.85	44.2	64.84	60.1	103.9	74.9
5.7	53.3	32.9	59.5	65.34	66.3	104.31	82.6
6.96	19.1	33.42	75.4	66.32	44.4	104.71	98.3
8.22	8.1	33.94	73.3	67.09	41.1	105.12	87.9
9.48	30.7	34.46	79.1	67.94	15.5	105.53	64.5
11.24	50.8	34.98	73.9	68.38	13.8	105.94	46.1
12.99	30.6	35.5	52.5	69.26	12.9	106.35	37
14.66	60	36.02	35.4	69.7	-4.6	106.75	32.2
15.18	65.9	36.54	62.3	70.14	-17.6	107.16	33.4
15.7	72.2	37.06	74.8	70.58	-17	107.57	31.4
16.1	51.9	37.58	101.5	71.02	-15	108.14	32.9
16.75	31	38.1	101	71.65	2.2	109.5	40.7
17.27	18	38.63	90.3	72.56	9.9	110.85	51.8
17.79	5.7	39.15	85.5	73.48	16.4	112.2	54
18.31	11.7	39.67	57.2	74.4	44.4	114.91	65.8
18.83	11	40.19	41.7	75.32	58.2	116.26	76.4
19.35	6.2	40.71	18.3	76.23	66.7	117.61	68.8
19.87	12.7	41.23	17.9	77.15	77.2	118.97	68.8
20.39	17.5	41.75	13.5	78.07	77	120.32	84.5
20.91	12.7	42.27	23.3	78.98	65.1	121.67	74.5
21.43	18	42.53	41.2	79.9	60	124.38	66.3

21.96	21.4	43.31	60.8	80.82	61.1	125.73	64.6
22.48	18.4	43.84	57.9	81.74	70.3	127.08	59.3
23	17.3	44.36	78.6	82.65	65.5	128.39	68.1
23.52	28.7	44.88	76.4	83.57	68	129.41	58.2
24.04	21.9	45.4	38.8	84.49	66.8	130.43	53.6
24.56	24.3	45.92	28.5	85.4	68.1	131.45	54
25.08	30.1	46.44	79.3	86.32	47.7	133.16	21.2
25.6	33.2	47.93	99.8	87.24	35.7	133.54	8
26.12	29.5	49.43	100.5	88.16	34.4	134.29	-10.4
26.64	38.2	50.94	77.7	89.65	64.7	135.42	-26
27.16	42	52.45	58	92.65	67.1	136.55	-21.5
27.69	53.1	60.27	80.1	94.15	45.4	137.31	-12.3
28.73	43.2	61.2	73.1	97.15	44.7	138.44	-8.3
29.25	26.6	62.13	49.5	98.65	24.3	138.82	-1.2
29.77	19.2	62.87	40.1	100.15	33.5	140.3	1.1
30.29	39.5	63.36	45	101.65	25.3		

Appendix E.

Average Diatom Assemblage Preservation

***Table 9**: Information on average preservation of diatom assemblage by sample. Each diatom identified per slide (min. of 300 diatoms per slide) was given a relative preservation value of 0-4, representing 1 (extreme dissolution) and 4 (virtually perfect preservation), discussed in Appendix C.*

Sample Depth (cm)	Age (ka)	Avg. Preservation	Sample Depth (cm)	Age (ka)	Avg. Preservation
10	1001	3.47	197	68608	3.51
20	2531	3.42	200	69999	3.63
30	4061	3.45	203	71790	3.32
40	5591	3.47	207	74196	3.22
50	7152	3.75	210	76000	3.45
53	7584	3.3	213	77802	3.43
57	8108	3.24	217	80207	3.42
60	8486	3.32	220	82000	3.59
63	8890	3.41	223	83491	3.36
67	9735	3.45	227	85503	3.51
70	10404	3.38	230	87000	3.39
73	11056	3.27	233	90289	3.42
77	11844	3.31	237	94703	3.34
80	12306	3.46	240	98011	3.51
83	12747	3.30	243	101314	3.41
87	13361	3.32	247	105715	3.27
90	13963	3.61	250	108999	3.43
93	14581	3.42	253	111094	3.26
97	15404	3.47	257	113903	3.25
100	16011	3.44	260	116007	3.06
103	16609	3.2	263	118110	3.34
107	17406	3.12	267	120912	3.32
110	18000	3.62	270	123000	3.39
113	19893	3.33	273	123597	3.38
117	22434	3.40	277	124398	3.36
120	24340	3.36	280	124998	3.46
123	26244	3.07	283	125598	3.64
127	28780	3.32	287	126398	3.39
130	30686	3.59	290	126999	3.39
140	37035	3.42	293	127600	3.22
150	43357	3.38	297	128403	3.44
160	49677	3.43	300	129000	3.41

170	56000	3.41	303	130644	3.42
180	60672	3.51	307	132850	3.29
183	62074	3.24	310	134503	3.12
187	63942	3.30	313	136155	3.19
190	65340	3.56	317	138360	3.21
193	66740	3.35	320	140000	3.51

Appendix F.

Opal, $CaCO_3$, Fe, and Total Concentrations and MAR Results

***Table 10**: Opal MAR Results*

Depth (cm)	Age (yr)	Opal (%)	Sed Rate (cm/ka)	DBD (g/cm^3)	opal MAR ($g\ cm^{-2}\ ka^{-1}$)
0	0	55.08		0.33	
10	1001	59.31	9.99	0.33	1.96
20	2531	63.63	6.54	0.31	1.29
30	4061	64.28	6.54	0.29	1.22
40	5591	62.46	6.54	0.33	1.35
50	7152	63.03	6.41	0.34	1.37
60	8486	58.71	7.50	0.33	1.45
70	10404	60.58	5.21	0.33	1.04
80	12306	70.08	5.26	0.27	0.99
90	13963	65.17	6.04	0.29	1.14
100	16011	71.48	4.88	0.24	0.84
110	18000	56.35	5.03	0.37	1.05
120	24340	61.12	1.58	0.32	0.31
130	30686	66.24	1.58	0.34	0.35
140	37035	73.48	1.58	0.3	0.35
150	43357	76.5	1.58	0.29	0.35
160	49677	73.89	1.58	0.27	0.32
170	56000	52.7	1.58	0.34	0.28
180	60672	63.23	2.14	0.39	0.53
190	65340	70.32	2.14	0.26	0.39
200	69999	70.05	2.15	0.26	0.39
210	76000	69.13	1.67	0.26	0.30
220	82000	67.7	1.67	0.24	0.27
230	87000	61.49	2.00	0.26	0.32
240	98011	63.03	0.91	0.31	0.18
250	108999	59.42	0.91	0.35	0.19
260	116007	59.16	1.43	0.35	0.30
270	123000	61.36	1.43	0.29	0.25
280	124998	52	5.01	0.31	0.81
290	126999	33.91	5.00	0.36	0.61
300	129000	58.73	5.00	0.23	0.68
310	134503	49.42	1.82	0.21	0.19

320	140000	66.17	1.82	0.38	0.46

***Table 11**: $CaCO_3$ MAR Results*

Depth (cm)	Age (yr)	CaCO3 (%)	Sed Rate (cm/ka)	DBD (g/cm^3)	CaCO3 MAR ($g\ cm^{-2}\ ka^{-1}$)
0	0	21.20		0.33	
10	1001	19.42	9.99	0.33	0.64
20	2531	13.01	6.54	0.31	0.26
30	4061	10.95	6.54	0.29	0.21
40	5591	10.88	6.54	0.33	0.23
50	7152	14.19	6.41	0.34	0.31
60	8486	14.57	7.50	0.33	0.36
70	10404	19.98	5.21	0.33	0.34
80	12306	7.93	5.26	0.27	0.11
90	13963	5.82	6.04	0.29	0.10
100	16011	1.52	4.88	0.24	0.02
110	18000	6.84	5.03	0.37	0.13
120	24340	7.85	1.58	0.32	0.04
130	30686	6.46	1.58	0.34	0.03
140	37035	7.14	1.58	0.3	0.03
150	43357	5.30	1.58	0.29	0.02
160	49677	7.28	1.58	0.27	0.03
170	56000	20.75	1.58	0.34	0.11
180	60672	17.42	2.14	0.39	0.15
190	65340	3.58	2.14	0.26	0.02
200	69999	7.57	2.15	0.26	0.04
210	76000	7.97	1.67	0.26	0.03
220	82000	11.14	1.67	0.24	0.04
230	87000	13.67	2.00	0.26	0.07
240	98011	13.42	0.91	0.31	0.04
250	108999	23.71	0.91	0.35	0.08
260	116007	24.77	1.43	0.35	0.12
270	123000	17.20	1.43	0.29	0.07
280	124998	30.61	5.01	0.31	0.47
290	126999	47.82	5.00	0.36	0.86
300	129000	12.16	5.00	0.23	0.14
310	134503	2.23	1.82	0.21	0.01
320	140000	9.36	1.82	0.38	0.06

***Table 12**: Fe MAR Results*

Depth (cm)	Age (yr)	Fe (‰)	Sed Rate (cm/ka)	DBD (g/cm^3)	Fe Mar ($g\ cm^{-2}\ ka^{-1}$)
0	0			0.33	
10	1001	0.4003	9.99	0.33	0.0077
20	2531	0.3991	6.54	0.31	0.0072
30	4061	0.3426	6.54	0.29	0.0068
40	5591	0.3177	6.54	0.33	0.0072
50	7152	0.3934	6.41	0.34	0.0092
60	8486	0.4322	7.50	0.33	0.0104
70	10404	0.5945	5.21	0.33	0.0102
80	12306	0.6264	5.26	0.27	0.0095
90	13963	0.6347	6.04	0.29	0.0115
100	16011	0.6927	4.88	0.24	0.0093
110	18000	2.2845	5.03	0.37	0.0482
120	24340	0.9526	1.58	0.32	0.0047
130	30686	0.7126	1.58	0.34	0.0037
140	37035	0.3956	1.58	0.3	0.0018
150	43357	0.3439	1.58	0.29	0.0015
160	49677	0.4544	1.58	0.27	0.0019
170	56000	0.7055	1.58	0.34	0.0037
180	60672	0.8117	2.14	0.39	0.0073
190	65340	0.4148	2.14	0.26	0.0025
200	69999	0.2643	2.15	0.26	0.0016
210	76000	0.3218	1.67	0.26	0.0011
220	82000	0.2149	1.67	0.24	0.0007
230	87000	0.3015	2.00	0.26	0.0010
240	98011	0.2718	0.91	0.31	0.0011
250	108999	0.3918	0.91	0.35	0.0018
260	116007	0.4932	1.43	0.35	0.0023
270	123000	0.5856	1.43	0.29	0.0050
280	124998	0.5164	5.01	0.31	0.0047
290	126999	0.6322	5.00	0.36	0.0067
300	129000	0.5649	5.00	0.23	0.0038
310	134503	0.5268	1.82	0.21	0.0033
320	140000	2.8271	1.82	0.38	0.0134

***Table 13**: Total MAR Results*

Depth (cm)	Age (yr)	Sed Rate (cm/ka)	DBD (g/cm^3)	Total MAR ($g\ cm^{-2}\ ka^{-1}$)

0			0.33	
10	1001	9.99	0.33	3.297
20	2531	6.54	0.31	2.026
30	4061	6.54	0.29	1.895
40	5591	6.54	0.33	2.157
50	7152	6.41	0.34	2.178
60	8486	7.50	0.33	2.474
70	10404	5.21	0.33	1.721
80	12306	5.26	0.27	1.420
90	13963	6.04	0.29	1.750
100	16011	4.88	0.24	1.172
110	18000	5.03	0.37	1.860
120	24340	1.58	0.32	0.505
130	30686	1.58	0.34	0.536
140	37035	1.58	0.3	0.473
150	43357	1.58	0.29	0.459
160	49677	1.58	0.27	0.427
170	56000	1.58	0.34	0.538
180	60672	2.14	0.39	0.835
190	65340	2.14	0.26	0.557
200	69999	2.15	0.26	0.558
210	76000	1.67	0.26	0.433
220	82000	1.67	0.24	0.400
230	87000	2.00	0.26	0.520
240	98011	0.91	0.31	0.282
250	108999	0.91	0.35	0.319
260	116007	1.43	0.35	0.499
270	123000	1.43	0.29	0.415
280	124998	5.01	0.31	1.552
290	126999	5.00	0.36	1.799
300	129000	5.00	0.23	1.149
310	134503	1.82	0.21	0.382
320	140000	1.82	0.38	0.691

Appendix G.

MAT Transfer Function Output Files

All MAT transfer function data can be accessed at: https://doi.pangaea.de/10.1594/PANGAEA.938457.

Appendix H.

Discussion Regarding TAN1302-96's Age Model

1.0 Introduction

The age model constructed for TAN1302-96 (henceforth, the 'original age model') was questioned by an anonymous reviewer during the review process and then again following publication. The issues raised focus on the amplitude of the $\delta^{18}O$ record relative to nearby core SO136-111 and the decision not to include two ^{14}C samples that returned dates of 'non-distinguishable from background' (NDFB), corresponding to >57.5 ka BP. The reviewer provided an alternative age model (henceforth, the 'proposed age model'), which is the subject of this addendum. The full comment made by the reviewer, including the author's response, can be found at: https://cp.copernicus.org/preprints/cp-2021-107/#discussion under RC3. The original comments led to a refinement of the age model in the published work; however, the subsequent comments are addressed here.

2.0 Overview of Reviewer's Comments and Author's Response

The main concerns the reviewer raised were around interpretation of the $\delta^{18}O$ record and the decision to exclude two NDFB ^{14}C samples from the age model. The reviewer's comments suggested that our interpretation of the $\delta^{18}O$ was incorrect based on the magnitude of changes relative to nearby core SO136-111. Specifically, the reviewer suggested that although the top 110 cm, corresponding to the Holocene and LGM, (~3 to 18 ka BP), was correct and well-constrained by ^{14}C samples and $\delta^{18}O$ minima, the $\delta^{18}O$ values from 110 to 220 cm were too negative to be attributed to MIS 2, 3, and 4, as was done in our original age model. Instead, the reviewer suggested that the 10 cm of sediment accumulation between 110 to 120 cm corresponded to MIS 2, 3, and 4 (18 to 69 ka BP), representing 51 ka of accumulation. Additionally, the reviewer suggested that 130 to 300 cm correspond to MIS 5 (71 to 130 ka BP), representing 59 ka of accumulation. Both the original age model and the reviewer's proposed age model (Figure 24) agreed on the identification of MIS 5e and Termination II (~124 to 130 ka BP). The reviewer suggested that their interpretation was supported by the two ^{14}C

samples taken at 130 and 170 cm, which returned dates of NDFB (i.e., >57.5 ka BP), that were excluded from the manuscript age model.

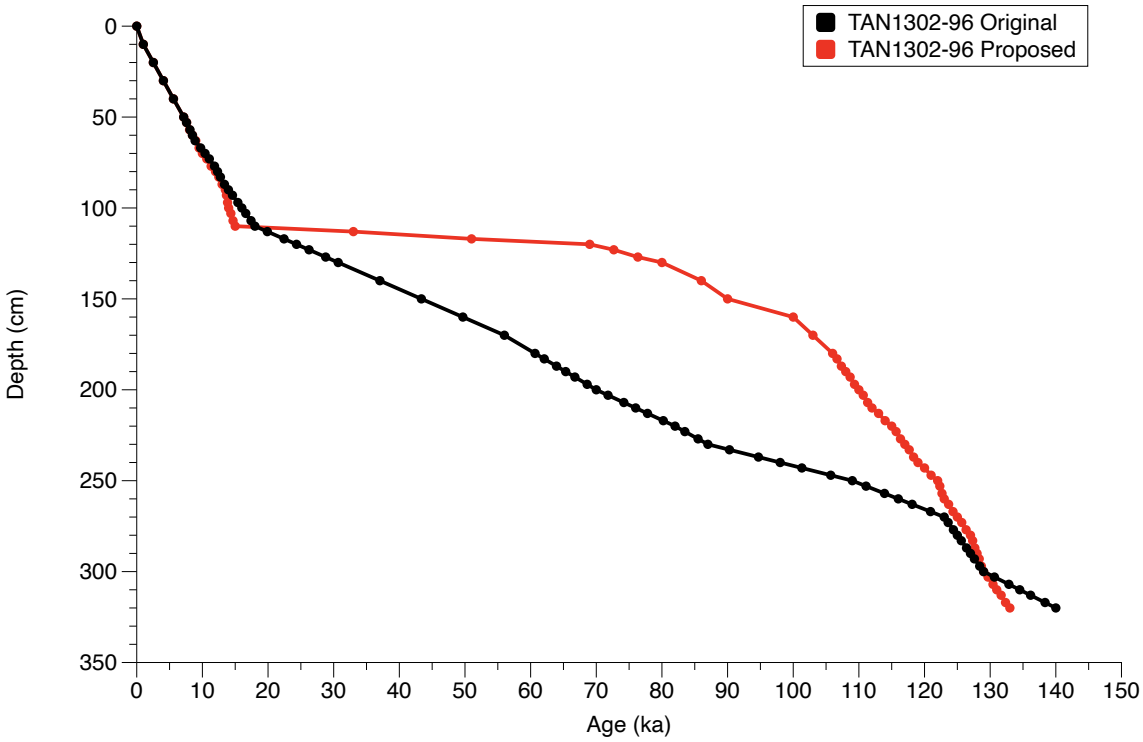

***Figure 24**: Depth vs. age of the original age model (black) from Jones et al. (2022) and the proposed age model (red) as suggested by the reviewer.*

In response to these comments, the co-authors outlined a series of additional age model constructions and criteria to evaluate against to determine which age model was the most robust. The co-authors constructed 4 additional age models (5 total), 3 of which were tied to the EPICA Dome C deuterium temperature record (EDT) and used a combination of both, one, or neither of the NDFB radiocarbon dates, which were set at the 57.5 ka BP (i.e., the maximum detection limit). Using these constructed age models, including the original age model and the proposed age model, criteria were outlined to compare the TAN1302-96 age models against the independent age model of nearby marine core SO136-111 (Crosta et al., 2004). The determination of the most robust age model was based on:

[1] match of the $\delta^{13}C$ records between TAN1302-96 and SO136-111;

[2] sensible behaviour and magnitude of sediment accumulation rates relative to SO136-111; and

[3] overall fit to $\delta^{18}O$ and EDC SST.

This process ultimately led to a refining of the age model and the determination that the proposed age model was likely incorrect. The refined age model was accepted by the publisher and has subsequently been published in the scientific journal *Climate of the Past*. After the manuscript was accepted for publication, the issue was re-raised by the reviewer to further discuss the issues.

Following additional review, the co-authors concluded that although the age model proposed by the reviewer is possible, the published age model remains the more likely option. The following sections highlight [1] arguments that support the proposed age model; [2] arguments against the proposed age model; and [3] additional data needed to help resolve these issues.

3.0 Arguments Supporting the Proposed Age Model

3.1 δ18O Record

The central critique of the original age model is the $\delta^{18}O$ record of TAN1302-96. In the original age model, the $\delta^{18}O$ is tied to the LR04 benthic stack at 9 tie points (see Appendix A, Table 5). Compared to the LR04 benthic stack, the amplitude of TAN1302-96's $\delta^{18}O$ is lighter by ~0.5 to 1‰ (Figure 25), which the reviewer suggests is the primary evidence of the age model's inaccuracy. The proposed age model is nearly identical to the original age model until the $\delta^{18}O$ maxima at 110 cm; however, from 120 to 320 cm the proposed age model's $\delta^{18}O$ is tied directly to the SO136-111 $\delta^{18}O$ record. Although tying the records together such that they fit in terms of timing and amplitude appears to reconcile the $\delta^{18}O$ records, this does affect the sedimentation rates, $\delta^{13}C$, and overall results of the core (discussed later).

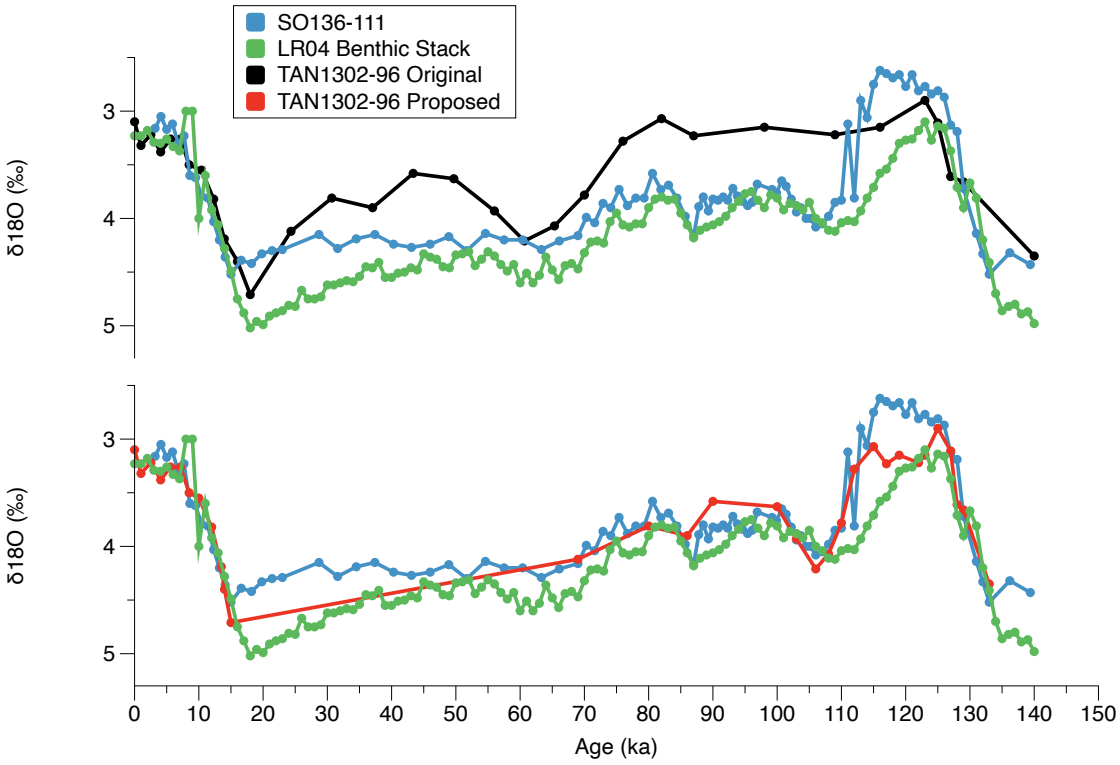

***Figure 25**: $\delta^{18}O$ record for the original age model (top, black) compared to the LR04 benthic stack (green) and SO136-111 record. The proposed age model (bottom, red) is compared to the LR04 and SO136-111 records.*

3.2 NDFB ^{14}C Dates

The reviewer also suggested that their interpretation of the $\delta^{18}O$ record is supported by the two ^{14}C samples that produced non-distinguishable from background (NDFB) dates. The detection limit for both samples taken at 130 and 170 cm is 57.5 ka BP, which the reviewer suggested should be included as a minimum age. In our original (published) Bayesian age modelling approach, both NDFB samples were treated as outliers and subsequently excluded from the age model because they conflicted with the assumed positive sediment accumulation (i.e., produced an age reversal) and chosen tie points. However, including the two NDFB ages (>57.5 ka BP) at depths 130 and 170 cm would support the validity of the proposed age model and therefore cannot be ruled out.

4.0 Arguments Against the Reviewer's Proposed Age Model

4.1 $\delta^{13}C$

Although the $\delta^{18}O$ record and the ^{14}C dates lend some support for the proposed age model, the $\delta^{13}C$ record does not (Figure 26). Compared to SO136-111, the $\delta^{13}C$ record from the original TAN1302-96 age model shows a coherent regional pattern of planktonic $\delta^{13}C$ over the last glacial-interglacial cycle. Using the proposed age model changes the pattern such that TAN1302-96 and SO136-111 have quite different $\delta^{13}C$ records, with notably different patterns around ~80 to ~90 ka BP and 100 to ~110 ka BP. The agreement in $\delta^{13}C$, which captures the localized surface water conditions, provides the strongest evidence in support of the original age model.

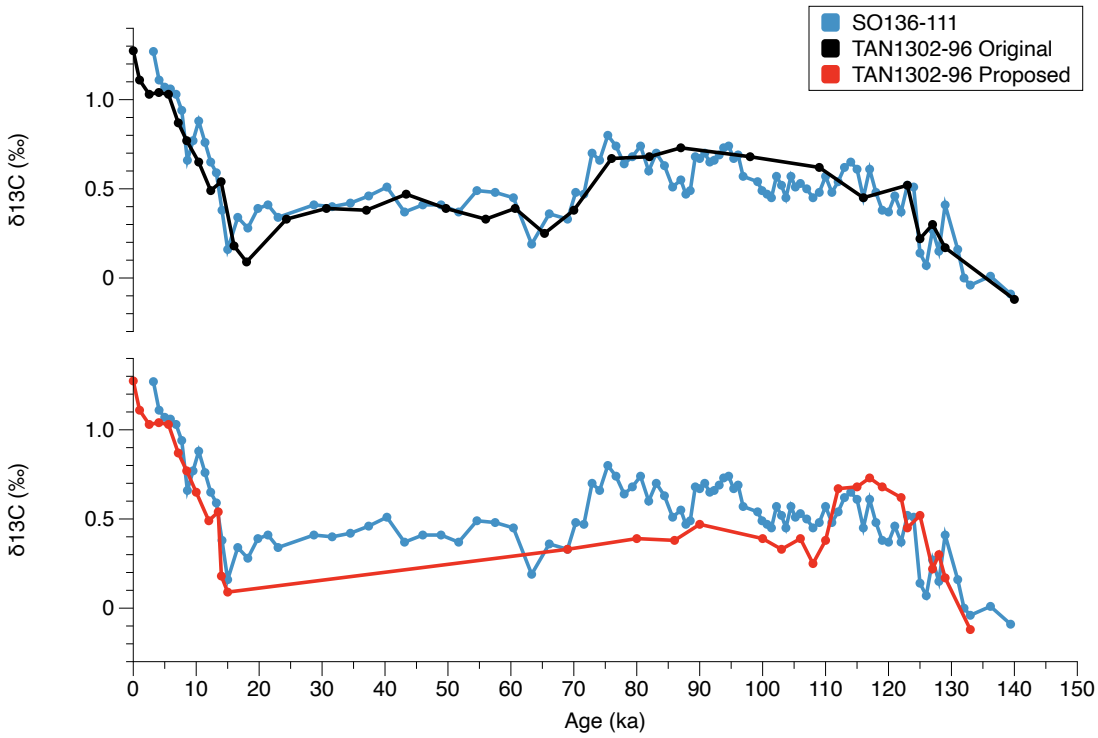

***Figure 26**: $\delta^{13}C$ record from TAN1302-96 using the original age model (top, black) compared to the proposed age model (bottom, red). Both records are compared to the $\delta^{13}C$ record of SO136-111.*

4.2 Sedimentation Rates

Based on the sedimentation rates of TAN1302-96, comparing the proposed age model with the original age model would result in drastically different sedimentation rates. The sedimentation rates calculated using the original age model average between ~5 cm ka^{-1} during warm periods (Holocene and MIS 5e) and ~1.5 to 2 cm ka^{-1} during cool periods (MIS 2, 3, 4, and 6). SO136-111 has sedimentation rates between 6 cm ka^{-1} during warm periods and ~2 to 3 cm ka^{-1} during cold periods (Crosta et al., 2004). E27-23, on the other hand, has sedimentation rates that are highly variable, ranging from between 23 to 132 cm ka^{-1} during the Holocene to between <1 to 5 cm ka^{-1} during MIS 2 (Table 1 in Ferry et al., 2015). It is worth noting that preliminary focusing factor (FF) calculations (see Figure 23 in Appendix C) suggest that E27-23 may have been susceptible to significant lateral sediment redistribution, which may explain the highly variable sedimentation rates.

The sedimentation rates calculated using the proposed age model show significant variability, with sedimentation rates between ~6 and 24 cm ka^{-1} during warm periods (Holocene and MIS 5e), declining to virtually 0 during the cooler periods of MIS 2, 3, and 4 (Figure 27). To explain the significant difference between sedimentation rates, we would expect to see major changes in environmental parameters that limit sedimentation (e.g., consolidated sea ice coverage of ~80% over the core site), or changes in bottom currents that could be driving sediment winnowing. Although analysis of ^{230}Th-normalization (which would confirm the degree of sediment winnowing) is still pending, our estimates suggest that sea-ice coverage at TAN1302-96 never exceeds ~50%. Based on the data available, the original age model has almost identical sedimentation as SO136-111 during MIS 2, 3, and 4 (~2 cm ka^{-1}), which is the period most contested by the reviewer.

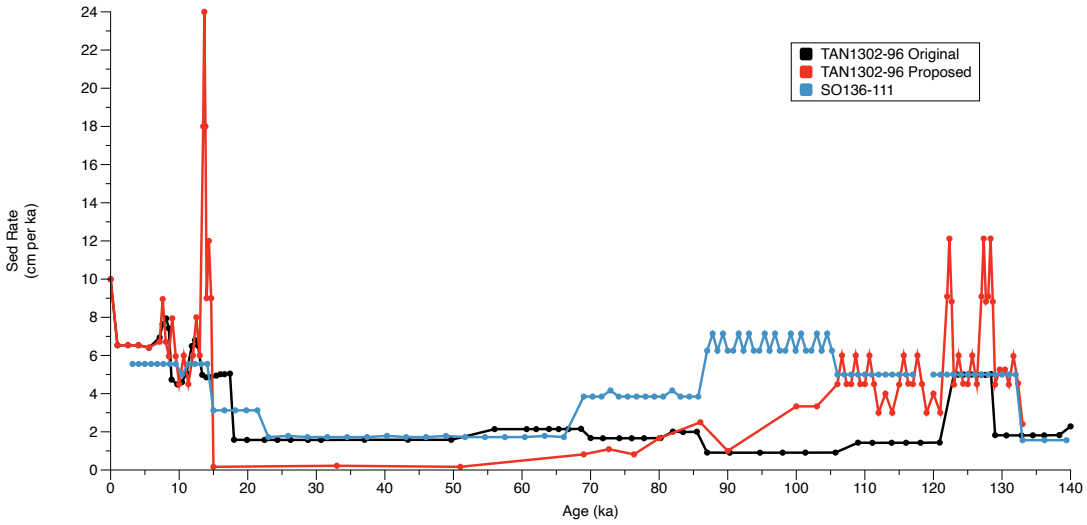

***Figure 27**: Comparison of sedimentation rates (cm ka^{-1}) by age (ka), including TAN1302-96 original (black) and proposed (red), and SO136-111 (blue). Note that despite it's close proximity, E27-23 was left out of this comparison because of the preliminary focusing factor results suggesting lateral sediment redistribution.*

5.0 Additional Data Needed to Resolve Uncertainty

In order to resolve this uncertainty, three additional analyses have been proposed by members of the C-SIDE working group, including: [1] the addition of ^{230}Th-normalized flux data, which will identify any lateral sediment redistribution throughout the core; [2] an assessment of the extinct diatom species *Rouix leventerae*, which can help 'measure' the length of certain stages; and [3] an assessment of bottom topography and the possible influence of localized sediment redistribution.

5.1 Thorium normalization

The addition of U-Th systematics for TAN1302-96 will help address the uncertainties surrounding any lateral sediment redistribution that may be driving chronological uncertainties. The sedimentation rates from E27-23, which show very high rates (up to 132 cm ka^{-1}) during the Holocene, are similar in pattern to the sedimentation rates using the proposed age model. However, preliminary FF values for E27-23 suggest that the core may have experienced lateral sediment redistribution, which could be driving the high sedimentation rates. This emphasizes the need to conduct the same

analysis on TAN1302-96 to identify if any lateral redistribution has occurred. For example, in the proposed age model, sediment winnowing could be driving the very low accumulation rates during MIS 2, 3, and 4 (110 to 120 cm). Conversely, sediment focusing could potentially account for the “extended” MIS 5 (130 to 300 cm). Although other factors would need to be invoked (e.g., substantial changes in bottom currents), ^{230}Th-normalized sedimentation could provide some insights into this possibility and would allow for a more accurate comparison of sedimentation rates from E27-23. U-Th systematics are currently being analyzed by Zanna Chase and colleagues at the University of Tasmania and results are expected later during 2022.

5.2 Last occurrence datum (LOD) Diatom Species

Another proposed way to reconcile the different age models was to consider the presence of the extinct diatom species *Rouix leventerae*. Zielinski et al. (2002) suggests that the species *R. leventerae*, whose last occurrence datum (LOD) is tightly constrained to the end of MIS 6 (140 to 130 ka BP), can be used as a biostratigraphic tie point when sediments lack continuous calcareous microfossils. This species has been suggested to have had higher relative abundances during the MIS 6 cold period compared to the warmer MIS 7 (Crosta, per. comm., 2022), which could allow us to effectively measure the length of MIS 6 (in cm) and use this to calculate sedimentation rates during MIS 6 to compare against the sedimentation rates outlined in the proposed age model. While this use of LOD species to refine our age model in theory works, there are 3 key issues with this proposal: [1] TAN1302-96 does not capture the entirety of MIS 6 so we would be unable to reliably measure sedimentation rates without a fixed time interval, [2] Zielinski et al. (2002) noted that *R. leventerae* represent <1% of the species assemblage between 140 to 130 ka BP, which could result in an incorrect identification of the precise transition from MIS 6 to 5e, and [3] both the original and proposed age model agree on the location of the MIS 6/5e transition, which is well-constrained by the $\delta^{18}O$ record, so conducting this analysis would likely not have any impact on resolving the issues raised. Therefore, the use of *R. leventerae* as a biostratigraphic tie point on TAN1302-96 would not help resolve this particular age model issue.

5.3 Regional Bathymetry

Finally, the last analysis that could provide insights into what may be causing the variable sedimentation in the proposed age model is considering the regional bathymetry. To explain the high sedimentation rates during interstadial periods (e.g., MIS 5) and very little sedimentation during cool stadial periods (MIS 2, 3, and 4), as suggested in the proposed age model, we would expect to see changes in environmental parameters that influence sedimentation, such as sea ice coverage, or changes in circulation that may be redistributing sediment. Therefore, additional analyses on the location and local topography of TAN1302-96, E27-23, and SO136-111 may provide additional insights.

Based on the sea ice reconstructions from TAN1302-96, we do not see any section of the core (irrespective of age model) that produces sea-ice concentrations >50%. These estimates are approximately the same (albeit slightly higher) as those seen in SO136-111 during stadials (~40%), during which time sedimentation rates are around 2 cm ka^{-1} (Figure 27). These WSIC and sedimentation rates are approximately the same in TAN1302-96 during MIS 2, 3, and 4 (using the original age model), suggesting that sea ice coverage at the TAN1302-96 would not be limiting sedimentation to the degree suggested by the proposed age model. This suggests that if we accept the proposed age model, major changes in bottom circulation and sediment redistribution would be the most likely explanation for the lack of sediment accumulation during MIS 2, 3, and 4. If major circulation changes were occurring between the warm interstadial and cool stadial periods, we would expect to see similar redistribution and a lack of sedimentation at E27-23, which is located only 120 km to the southwest. Although SO136-111 has a high-resolution and well-constrained age model from the region, its location north of the Antarctic Polar Front (APF) suggests that it may subject to different bottom circulation and therefore not well-suited for a comparison with TAN1302-96 and E27-23, which are both located south of the APF.

The sedimentation rates for E27-23, as discussed previously, are highly variable between stadial and interstadial periods, ranging from ~1 to ~132 cm ka^{-1}, which are more extreme than those suggested by the proposed age model. It stands to reason that if sediment redistribution is affecting E27-23, as is suggested by the preliminary FF results, it may also be affecting TAN1302-96. Once the U-Th systematics analysis is

completed for TAN1302-96 and preliminary FFs for E27-23 are confirmed, an accurate comparison of lateral sediment redistribution could resolve some of these uncertainties. An additional analysis to address these uncertainties could involve a high-resolution bathymetric analysis of the TAN1302-96 and E27-23 core sites. These analyses could identify if each core site is located in a different physiographic setting, such as on different sides of sills or within a contourite deposit, which could inhibit (or enhance) redistribution at one of the core sites.

6.0 Conclusion

Overall, there is compelling evidence that the original (and published) age model for TAN1302-96 is robust. The main evidence in support of the original age model is the fit of the $\delta^{13}C$ signature to nearby marine core SO136-111 and the sensible sedimentation rates. Although the $\delta^{18}O$ record does appear to fit better with SO136-111 using the proposed age model, this could simply be an artifact of tying the two records together. The issues raised by the reviewer point to important questions that need to be answered, specifically why E27-23 shows similar sedimentation variability to the proposed age model, and if sediment redistribution is occurring at E27-23, is it also occurring at TAN1302-96. The addition of U-Th systematics on TAN1302-96 (pending at the time of writing) and a high-resolution analysis of the regional bathymetry for both E27-23 and TAN1302-96 could help resolve these uncertainties.